

New aerodynamics rotor concepts specifically for very large offshore wind turbines

Deliverable 2.11

Edited by: Helge Aagaard Madsen, Leonardo Bergami, Flemming Rasmussen

September 2013

Agreement no.:	308974
Duration	60 months from 1st November 2012
Co-ordinator:	Mr Peter Hjuler Jensen
Supported by:	EU 7th Framework Programme

Support by:



Document information

Document Name:	New aerodynamics rotor concepts specifically for very large offshore wind turbines
Confidentiality Class	PU
Document Number:	D2.11
Edited by:	Helge Aagaard Madsen, Leonardo Bergami, Flemming Rasmussen
Contributing Authors:	T. Chaviaropoulos, G. Sieros, A. Irisarri, A. Martinez, X. Munduate, F. Grasso, O. Ceyhan, H. A. Madsen, L. Bergami, F. Rasmussen, F. Zahle
Review:	Takis Chaviaropolous (CRES), Flemming Rasmussen (DTU)
Date:	September 2013
WP:	WP2 LIGHTWEIGHT ROTOR
Task:	Task 2.1.1 New aerodynamic blade designs

TABLE OF CONTENTS

SUMMARY OF FINDINGS	5
INTRODUCTION	7
CRES: LOW INDUCTION ROTOR	8
Scope and Objectives.....	8
Strategy for the aerodynamic design of the LIR version of RWT.....	9
Basic Theory.....	9
Design problem.....	10
Reference wind turbine (RWT).....	12
LIR Blade Planform and airfoil Characteristics	12
LIR rotor performance	15
Performance at the Design Point.....	15
Rotor Operating Conditions.....	16
Conclusion	18
CENER: OTHER CONCEPTS, DOWNWIND ROTOR AND THE TOWER SHADOW EFFECT	20
Introduction.....	20
Wind turbine configurations.....	20
Computed cases	20
Tower shadow model used:	20
Dynamic Stall:.....	20
Tip and Hub loss models:.....	21
Inflow model:.....	21
Results	21
Simulations performed at $V_m=10$ m/s	21
Simulations performed at $V_r=11.4$ m/s.....	25
TSR – azimuth	29
Conclusions.....	33
CENER: COMPRESSIBLE FLOW BLADE DESIGN VERIFICATION AND HIGH TIP SPEED.....	34
Introduction.....	34
Airfoil data used.....	34
Computed cases	42
Results	43
Power Production:	45
C_p , C_t , C_p/C_t and C_q :	47
$AoA-r$, $a-r$, $a'-r$, C_p-r , $Cl-r$, $Cd-r$:.....	49

Conclusions:.....	51
ECN: NEW AIRFOILS FOR HIGH EFFICENCY AND LOAD REDUCTION	52
Introduction.....	52
Requirements for new airfoils.....	52
Effects of new airfoils for the development of very large offshore wind turbines	53
Conclusions.....	56
ECN: PARAMETRICAL CONCEPT STUDY FOR LOWER POWER DENSITY ROTORS	57
Introduction and motivation.....	57
Parameters	57
Results	57
Conclusions.....	61
DTU WIND: TWO-BLADED ROTOR CONFIGURATION	62
Introduction.....	62
Two-bladed rotor configuration.....	62
Derivation.....	62
Structural properties	63
Steady state analysis	64
Rotational frequency and turbulence spectrum	68
Aeroelastic interaction with the tower modes.....	71
Teetering hub configuration.....	74
Conclusion	76
REFERENCES	77

SUMMARY OF FINDINGS

The deliverable presents a comparison of innovative rotor concepts and summarizes their performances in terms of key figures as expected annual production and load levels, which, combined with cost models from WP1 will allow to identify rotor concepts with promising cost effectiveness.

The deliverable first reports the results of aerodynamic studies on basic concepts for innovative rotor configurations. CENER, quantifies the effects of including flow compressibility in the profile coefficients computation using XFOIL: steeper lift coefficient slope and increased drag cause a reduction of the power coefficient in the outer span of the blade. The rotor power coefficient is decreased by 0.5 % when accounting for compressibility effects at the reference tip speed of 90 m/s. Even higher variations are reported for operation at higher rotational speeds, with a tip speed of 110 m/s the reduction in power coefficient is in the order of 1 %. The losses could be limited by modifying the operation conditions to account for the shifting of the optimal tip speed ratio to approximately 4 % lower values when considering compressibility effects; it is thus worth to consider the compressibility at the blade design stage. CENER also quantifies the effects from tower-shadow on a downwind rotor configuration in terms of increase in angle of attack variations and local tip-speed ratio variations, both for a three bladed and a two bladed configuration; stronger variations are reported in the two bladed case. Limiting the tower shadow effects could be an objective in the airfoil design process by limiting C_l variations either through fixed or variable airfoil geometry.

The contributions from CRES and ECN highlight the potentialities of lower power density rotors, so far based on steady aerodynamic considerations, and thus not taking fatigue during operation and stand still condition into account. The investigation from CRES proposes a low induction rotor with a larger radius (13 %) and higher tip-speed values. The rotor achieves 3.5 % higher annual energy production (AEP) than the reference wind turbine, while the mean flapwise bending moment is maintained. Furthermore, it would give a lower rotor thrust in steady conditions (10 % less than the reference one), and although tower bottom loads are expected to be similar to the reference ones due to the increased tower height, lower thrust might be beneficial to reduce wake losses effects in wind farm installations. The low induction solution would require airfoils with lower design lift coefficients (down to 0.8).

ECN investigates rotor solutions with 20 % longer radius than the reference one, and therefore lower rated wind speed, and higher annual energy yields. Among the investigated configurations, particularly promising results are obtained in combination with a lower solidity option, which returns a 4.5 % increase in AEP, 13 % lower thrust and almost unchanged blade root bending moments compared to the reference rotor. ECN also performed an investigation on the potential of employing high-performance airfoils. Maintaining the same energy output as in the reference rotor, high-performance airfoils would allow for a lower solidity configuration, thus reducing the loads in parked conditions (2.6 %), the thrust, and the blade root bending moment, by, respectively, 5.4 % and 5.6 % in steady conditions.

Further investigations in the INN WIND.EU project on low solidity rotor design will consider the impact from turbulence and extreme operating conditions on the rotor design.

DTU Wind presents a two-bladed downwind version of the reference wind turbine; by maintaining the same solidity as the reference rotor, the two-bladed configuration would have 18 % lighter rotor, but also 3 % lower AEP due to tip losses and larger tower shadow effects. The increased tip losses effects below rated wind speed in the two bladed configuration account for a reduction of the power output by approximately 4 % according to BEM simulations; similar figures are obtained with 3D CFD simulations, which return

3.5 % lower power in the two bladed case. The thrust load variation on the two bladed rotor would be higher than the reference one, as an effect of both tower shadow and turbulence sampling. For a rigid turbine, nearly a 25 % increase in the tower bottom fatigue damage equivalent load is reported. The contribution also stresses the need of re-designing the turbine tower, most likely toward more compliant tower configurations, lowering the tower stand-still frequency to less than 1.5 times the rotational frequency. By adopting a teetering hub solution, the shaft damage equivalent loads would be significantly lowered, down to one fifth of the reference ones; the damage equivalent loads on the blade root bending moment would be also reduced by 30 %, thus reaching nearly the same level as the reference blade in spite of the 50 % longer chord. The two bladed downwind teetering rotor concept shows thus a potential for load reduction and possibly cost reduction, but also some design challenges, as for instance in defining a new tower structure.

INTRODUCTION

The deliverable presents a series of innovative rotor concepts such as low induction rotors, low solidity rotors, lower power density rotors, as well as two-bladed down-wind rotor configuration. The proposed solutions are compared against the 10 MW reference rotor, and their performances are summarized in key figures such as expected annual production and load levels. Combined with the cost models elaborated within WP1, the key figures will thus allow to determine the rotor concepts with promising cost effectiveness characteristics.

The deliverable is organized in chapters corresponding to each partner contribution. First CRES presents a low induction rotor concept, thereafter CENER analysis on downwind rotor configurations with respect to tower shadow effects is reported. In the following chapter, CENER investigates the effects of accounting for flow compressibility in the steady aerodynamic analysis of the reference rotor. ECN then investigates new rotor concepts, based on high performance airfoils, and on larger radius configurations for lower power density. In the last chapter DTU Wind proposes a two-bladed downwind configuration of the reference rotor, and analyses the aeroelastic implication of such configuration; 3D CFD computations of the two bladed rotor are also performed to verify the tip losses prediction obtained with the BEM model.

CRES: LOW INDUCTION ROTOR

Takis Chaviaropoulos, Giorgos Sieros

The main design characteristics of large wind turbines have remained similar over the last generations, with performance improvements being a result of gradual changes in component design. Recently however, a new generation of multi-MW offshore rotors that are under development are deviating from the established design trends, displaying high tip-speed, low solidity but also larger than expected rotor diameters. The purpose of the study performed is to quantify the relative merits of this approach, associated to low induction – high swept area rotors. We are using BEM analysis of such solutions and comparing the results to those of the reference wind turbine (RWT) of the project in order to identify the possibilities for a significant reduction of the cost of energy, especially in large offshore wind farms.

Scope and Objectives

The purpose of the development of the Low Induction Rotor, is to examine the validity of the proposed shift in design patterns, and determine targets for the design of airfoil and planform shapes, compatible with the new LIR.

Examining designs that are currently under development and upscaling them to 10 MW for having a common comparison basis (see Table 1) we observe a shift of the design paradigm, compared to the reference wind turbine that was used for the UPWIND project [1], which was typical of the prevailing trends at the time.

Rotor	UPWIND [1] scaled to 10 MW	SWAY [2]	SeaTitan 10MW [3]	Siemens 6MW [4] scaled to 10MW	Vestas 8MW [5] scaled to 10MW	Alstom 6MW [6] scaled to 10MW
Diameter (m)	178	164	190	199	183	194
Blade Length (m)	87			97	89	95
Design RPM	8.56	12	10	8.52	9.39	8.91
Rated Wind Speed (m/s)	11.3	13		13	13	
Tip Speed (m/s)	80	103	99.5	88.7	90.2	90.3

Table 1: Characteristics of current offshore W/T designs

Larger diameters are used in most cases, combined with higher tip speeds. Large diameters in this case are not to be confused with the large diameters used in Class II and especially Class III turbines designed to better explore low wind speed sites. Here the focus is on high wind speed offshore sites where Class I (or even harder) wind conditions are normally expected. In a more traditional way of thinking, high-wind-speed designs should rather lead to smaller diameters (like in the Sway case) and certainly not larger. In order to provide an answer to the question we start with a theoretical analysis of the benefits of a lower induction rotor and proceed to the preliminary design of such a rotor, based on the INN WIND.EU reference wind turbine (RWT), and a comparison of its performance to the baseline level.

Strategy for the aerodynamic design of the LIR version of RWT

Basic Theory

In order to quantify our analysis we shall use the following set of equations and notation, as described in [7], elaborating on Blade Element Momentum (BEM) theory.

We use the standard definitions for Tip-Speed-Ratio (TSR or λ), blade section lift to drag ratio k and the radius fraction x according to Eq. (1). Note that V is the ambient wind speed, ω the rotational speed, R the rotor radius, and B the number of rotor blades.

$$\lambda = \omega R / V \quad k = C_L / C_D \quad x = r / R \quad (1)$$

Assuming a (uniform on the rotor disc) induction factor a , the span-wise distribution of the circumferential induction a' can be expressed as a function of a , k , λ and x :

$$a' = \frac{\sqrt{(k\lambda x)^2 + 2k\lambda x - 4ak[\lambda x - k(1-a) + 1]} - (k\lambda x + 1)}{2k\lambda x} \quad (2)$$

Using Prandtl's tip loss correction factor

$$F = \frac{2}{\pi} \cos^{-1} \left[\exp \left\{ - \frac{(1-x)B\lambda}{2(1-a)} \right\} \right] \quad (3)$$

And introducing the non-dimensional lift distribution $\Lambda(\lambda, x)$ where $c(\lambda, x)$ is the chord distribution,

$$\Lambda(\lambda, x) = \frac{c(\lambda, x)c_L}{R} \quad (4)$$

it can be shown that $\Lambda(\lambda, x)$, which for selected values of λ and B corresponds to the axial induction value a , is given by Eq. (5).

$$\Lambda(\lambda, x) = \frac{8\pi a(1-a)}{B\lambda(1+a')\sqrt{(1-a)^2 + \lambda^2 x^2(1+a')^2}} \frac{F}{\left[1 + \frac{(1-a)}{k\lambda x(1+a')} \right]} \quad (5)$$

For given design C_L value(s) Eq. (5) can be used for defining the blade chord distribution which yields a given axial induction factor, while the blade twist distribution will derive from the flow angle φ distribution, as given from the classical BEM velocity triangle,

$$\tan \varphi = \frac{(1-a)}{\lambda x(1+a')} \quad (6)$$

by subtracting the design angle of attack (corresponding to the design C_L value(s)).

The power coefficient C_P , rotor thrust coefficient C_T and aerodynamic bending moment coefficient $C_{M(r)}$ at arbitrary radial distance r are given by equations (7) to (9),

$$C_P(\lambda) = \int_0^1 \frac{8a(1-a)F[k(1-a) - \lambda x(1+a')]\lambda x^2}{[(1-a) + k\lambda x(1+a')]} dx \quad (7)$$

$$C_T = \int_0^1 8a(1-a)Fx dx \quad (8)$$

$$C_M(x) = \frac{8a(1-a)}{B} \int_x^1 \frac{F(y)}{[(1-a)/k + \lambda y(1+a')] \{ \lambda y + (1-a)/k \} (y-x)} dy \quad (9)$$

where the above coefficients are defined as non-dimensional representations of the Power (P), Thrust (T) and Bending Moment $M(x)$ through Eqs. (10) to (12).

$$P = \frac{1}{2} \rho \pi R^2 V^3 C_P \quad (10)$$

$$T = \frac{1}{2} \rho \pi R^2 V^2 C_T \quad (11)$$

$$M(x) = \frac{1}{2} \rho \pi R^3 V^2 C_{M(x)} \quad (12)$$

Design problem

For a pitching-variable speed HAWT design and for a given rotor radius the classical rotor aerodynamic design problem would seek to maximize the energy capture by maximizing the power coefficient C_P . According to the BEM theory this would happen for an axial induction value $a=1/3$ and would correspond to a TSR design value λ which gets larger (along with $C_{P,MAX}$) as the aerodynamic performance of the blades k gets better (higher). As design λ increases the non-dimensional lift distribution $\Lambda(\lambda,x)$ gets thinner and, for the same family of blade profiles, the rotor solidity gets lower.

For a variable speed rotor, the design λ value (and therefore $C_{P,MAX}$) can be maintained over a range starting from a minimum wind speed, defined by the low-end capability of the variable-speed power conversion system, up to a maximum wind speed which is limited by the rotor maximum tip-speed, either for restraining noise or centrifugal loading. We shall call this maximum wind speed, where $C_P = C_{P,MAX}$, “design wind speed”. Usually, the pitch variable speed turbines have their design wind speed just below their rated speed.

The top plot of Figure 1 presents a plot of C_P versus a for a three-bladed rotor with profiles of $k=100$. The $C_{P,MAX}$ value is 0.4966 corresponding to an a value of $1/3$.

Suppose that we have an initial wind turbine and rotor design and we want to add some freedom in our design by redesigning the rotor, letting its radius free, but respecting all turbine related constrains (the rated rotational speed, the rated wind speed and power, the hub loading etc). We will assume for simplicity that the new rotor will use the same family of airfoils (same k , considering Reynolds number effects as secondary at the scale of our interest).

Let R_0 be the initial rotor radius and let subscript “0” denote the initial (or reference) design, the one with $a=1/3$ corresponding to maximum C_P .

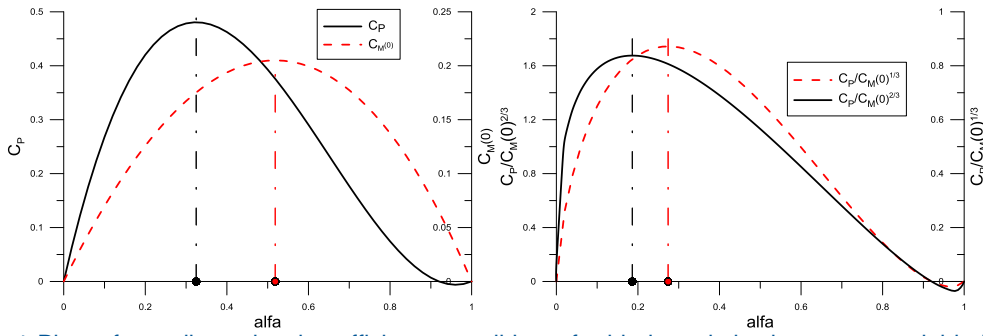


Figure 1 Plots of non-dimensional coefficients, candidates for blade optimization, versus axial induction coefficient a . Application of Eqs. (7) and (9) for $B=3$, $k=100$ and $\lambda=8.85$ (providing the maximum C_P value =0.4966 for the selected B and k combination). The a value corresponding to the maximum coefficient value is shown on the x-axis.

The new design problem is formulated as:

$$\frac{C_P(\lambda, \alpha) \cdot R^2}{C_{P0}(\lambda_0, \alpha_0) \cdot R_0^2} \rightarrow \max, \quad \text{subject to} \quad \frac{C_{M(0)}(\lambda, \alpha) \cdot R^3}{C_{M0(0)}(\lambda_0, \alpha_0) \cdot R_0^3} \cong 1 \quad (13)$$

That is: “maximize the power output up to the design wind speed without exceeding the initial aerodynamic root blade moment” (see Eqs. (10) and (12)). By eliminating the radius dependence the optimization problem (13) can be recast as:

$$\frac{C_P(\lambda, \alpha)}{C_{M(0)}(\lambda, \alpha)^{2/3}} \rightarrow \max \quad (14)$$

The solution of the optimization problem (14) for a , given $\lambda = \lambda_0$, is shown in the right side of Figure 1. The resulting value is $\alpha=0.187$ and although it has been calculated for a “wrong” $\lambda (= \lambda_0)$ it can be shown that the optimum α solution for (14) is λ insensitive.

As a result, the optimal rotor will have a larger radius: $R/R_0 = 1.136$; will capture more energy: $[C_P(\lambda, a) \cdot R^2] / [C_{P0}(\lambda_0, a_0) \cdot R_0^2] = 1.087$; and will be less loaded than the initial one (design C_T and $C_{M(r)}$ will be smaller), operating at a lower axial induction value $a=0.187$ instead of $a_0=0.33$. In other words, we sacrificed C_P in order to increase energy capture with a larger rotor diameter, while maintaining the aerodynamic bending moments at their initial level. This is feasible thanks to the special shape of the C_P and $C_{M(0)}$ curves, where moving a little left from the optimum a at the C_P curve the power coefficient loss is milder than the corresponding reduction of bending moments in the C_M plot.

The obvious question is whether this is cost effective, given that we have a 13% longer blade now. In a very primitive approach and taking only the aerodynamic moments into account, we can assume that the new blade can maintain the cross-sections of the initial blade as long as they have the structural strength to undertake the reference bending loads which are not altered. Thus, the new blade will result as a “prolongation” of the reference one to the new radius its cross sections being invariant in terms of the radius fraction x . This means that the weight and “cost” of the new blade will increase by a factor of R/R_0 . This would result in an increase of the levelized cost of the blade component of 4.6% (13% additional cost, 8.7% more power). Nevertheless, and since the levelized cost of the rotor blades is a small fraction of the overall levelized cost of electricity, particularly offshore, the selection of a larger, less loaded rotor for offshore turbines seems cost effective.

Evidently, the new rotor will have a proportionally increased tip-speed and consequently noisier. This is no problem for far offshore development. In addition, the new rotor will

operate better in a multiple row offshore wind farm or cluster since lower axial induction factors imply lower thrust coefficients and, thus, less wake effects in benefit of the production and loading of downstream turbines.

Reference wind turbine (RWT)

The previous theoretical approach gives an indication that the LIR concept is worth exploring. In order to get a better understanding of the operation of such a wind turbine we design a complete BEM solution. The starting point for the design is the reference wind turbine (RWT) provided by DTU [16] for the INN WIND.EU project. The design is evaluated in detail in [8] where CRES' in-house BEM formulation is also discussed. RWT has a rotor radius of 89.166 m, with chord twist and relative thickness data provided at 41 radial stations for BEM calculations. Nearly the outer 50 meters of the blade are having the same relative thickness equal to 24.1%. The rotor is rated for a tip speed of 90 m/s.

This reference design is *already* deviating from the previously mentioned scale-up of the UPWIND rotor, being more in-line with current trends for a higher tip speed.

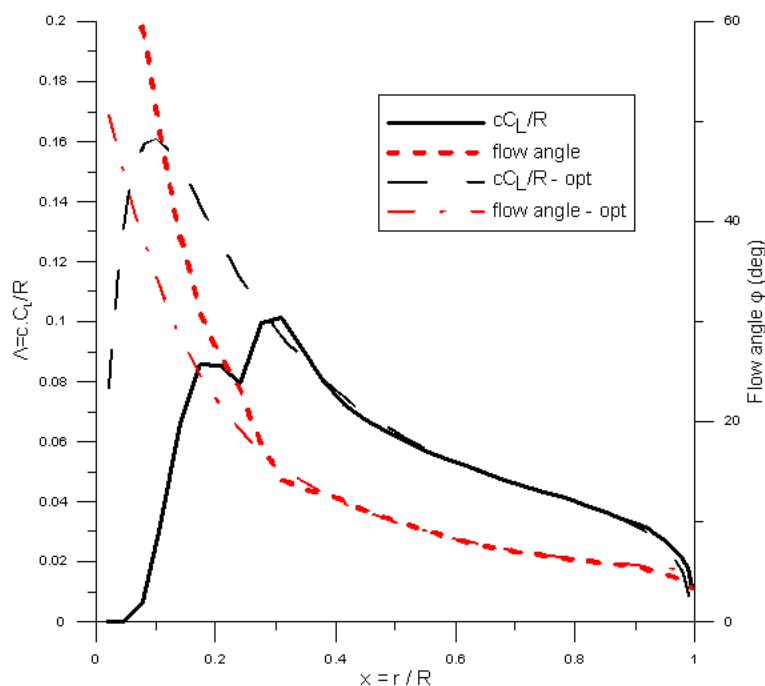


Figure 2 Theoretical optimum and actual non-dimensional lift distribution for the RWT

For the RWT, detailed description of the planform and airfoil geometry and performance are given in [16]. There are five primary profiles of different thickness (24.1%, 30.1%, 36%, 48% and 60%) comprising the adopted FFA-W3 family.

Using the previous analysis for the theoretical Λ distribution, the results from eq. (6) for induction factor equal to $1/3$ are shown in Figure 2, compared to the actual distribution for the RWT. It is apparent that the solution is very close to the optimum for the aerodynamic part of the blade, deviating only in the inner sections, where structural constraints pose limitations on twist and blade shape.

LIR Blade Planform and airfoil Characteristics

The design of a representative LIR is based on the choice of a different Λ distribution, corresponding to an axial induction factor of ~ 0.2 , as opposed to the theoretical optimum

used for the RWT. The LIR will be placed on the same turbine as the reference rotor and thus the rotational speed schedule should remain unchanged.

The resulting distribution, along with the required flow angle, are given in Figure 3, compared to the original wind turbine (assuming a three-bladed rotor with $k=100$).

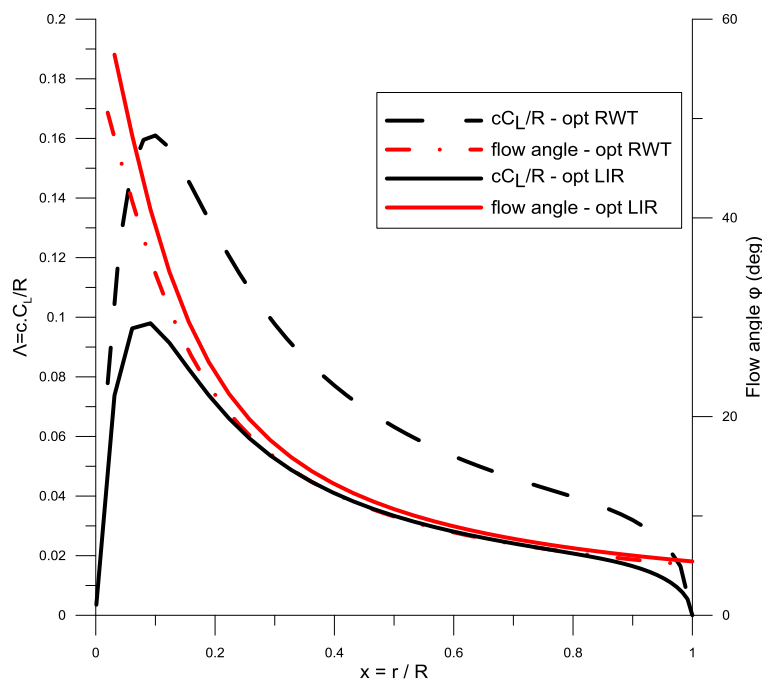


Figure 3. Normalized radial distributions of the optimum non-dimensional lift and the flow angle at design conditions ($\lambda = 7.5$)

In order to produce such a design, without reducing the normalized radial distributions of the chord length and blade thickness (as this would affect the structural integrity), blade sections with reduced lift at design conditions should be used. The resulting planform for the LIR solution is shown in Figure 4, with an elongated blade, but similar chord and thickness values to the RWT. The chord distribution is affected, but *not* up-scaled in an equivalent manner (as this would lead to a large weight increase). The two variations shown correspond to the use of a quasi-linear tapering of the blade, which allows variations in the axial induction factor and a strictly fixed induction factor, resulting in a more elaborate chord distribution. The observed change in pitch distribution is a direct result of the requirement for reduced loading, leading to different AOA at the sections.

The differing aerodynamic requirements for the sections indicate that the original high-lift airfoils would not be a good fit for the proposed design, as they would operate far from their optimum L/D . At this level of analysis, it is not possible to have a set of airfoils that is optimal for the design, but it is possible to derive the *desired* (still realistic) characteristics of such blades. As maximum C_L will be lower we are looking for an airfoil family that will have optimum $k=C_L/C_d$ at lower C_L values. As a starting point we utilised symmetrical NACA63 based profiles, deriving the polar characteristics through XFOIL calculations. Using these results would introduce a bias in favour of the LIR design, as the calculated k was significantly higher (most likely an erroneous over-prediction of a thick profile at high Reynolds numbers) than that provided for the RWT. It was therefore decided to scale the results to the same k , indicating a similar level of performance.

The resulting operating points for the sections are shown in Figure 5, where it is obvious that the design C_L for the LIR is ~ 0.8 , as opposed to 1.25 for the RWT. It is seen that the red-dots, indicating the actual performance of every blade section, are not coinciding

exactly with the sections' maximum performance point. This is true for the entire aerodynamic part of the blade. It should be noted however, that the sections used in the RWT are relatively insensitive to small changes in inflow angle [8]. The sections used for the LIR on the other hand are not optimised for wind turbine usage and could be more sensitive to such variations.

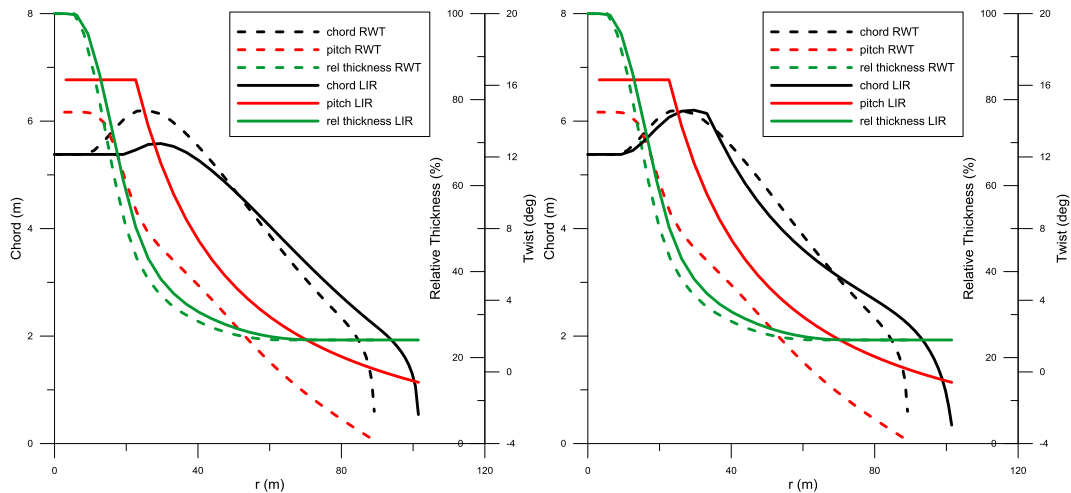


Figure 4. Blade planform characteristics – chord, twist and relative thickness radial distribution. RWT versus two different LIR designs with linear (left) and free (right) chord distribution.

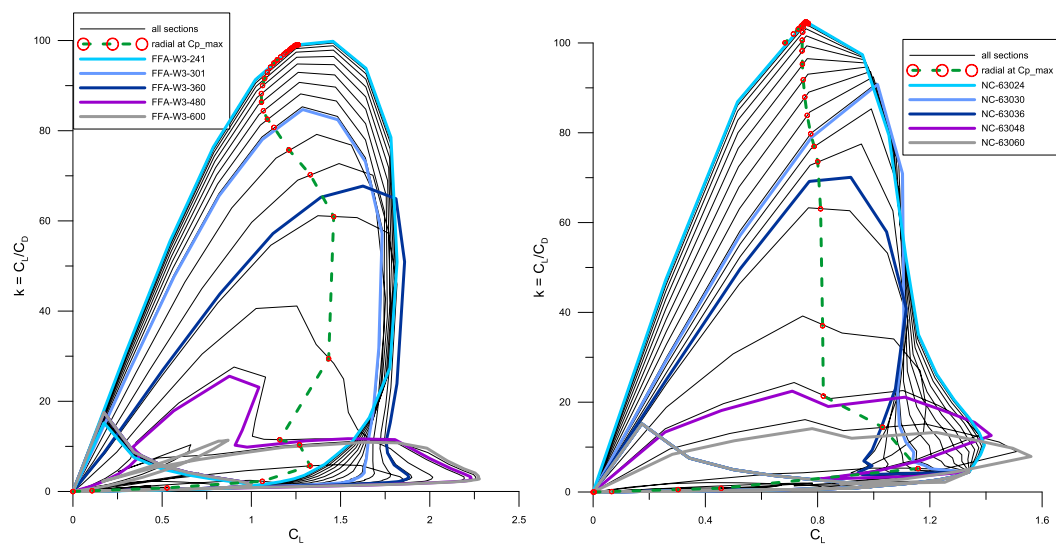


Figure 5. Performance plot of the blade sections derived through interpolation based on the relative thickness. RWT (left) vs LIR-fixed axial induction (right)

It should be stressed that the performance envelope for the airfoils is a design requirement and it remains to be seen if it is attainable through a detailed design.

LIR rotor performance

Performance at the Design Point

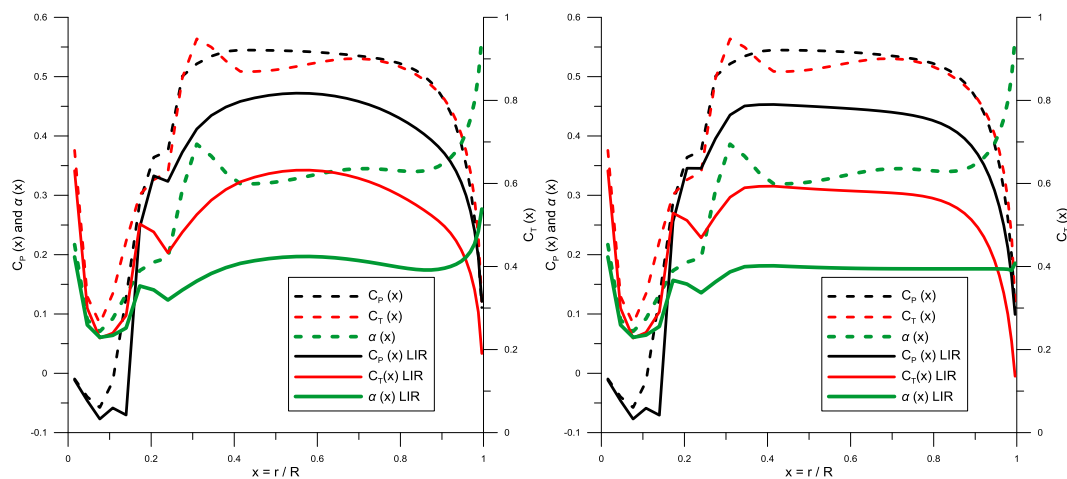


Figure 6. Pressure, thrust coefficients and axial induction factor (α) distributions along the blade at design conditions. RWT vs LIR, for fixed (right) and varying (left) axial induction.

In Figure 6 the radial distribution of the local pressure, thrust coefficient and axial induction factor at rotor design conditions is presented. It can be seen that at the aerodynamic part of the blade ($30\% < x < 85\%$) all three distributions are almost flat. However, while in the RWT α approaches its theoretical optimum value of 0.33, in the revised design a much lower value of ~ 0.2 is used. At the same time the local power coefficient which exceeds 0.5 for the original design is now significantly reduced. The same model for tip effects has been used in both cases, resulting in similar behaviour as expected for the outer part of the blade. The BEM solution in the area $0\% < x < 30\%$ is associated with significant uncertainties that are model- and data- dependent, as the modeling of operation in the non-aerodynamic part of the blade is not that accurate. This however does not affect the comparison between the two designs. The thrust coefficient level for the LIR has dropped from ~ 0.9 to ~ 0.6 for the larger part of the blade, as expected, a drop of almost 50%.

Elaborating on airfoil performance we present in Figure 7 the radial distribution of C_L/C_D along with the corresponding angle of attack calculated by the BEM code, against the distributions of $k = \max(C_L/C_D)$ and its angle of attack of the airfoil placed at that x . To achieve maximum rotor performance at the design point these distributions, at least in the aerodynamic part of the blade, should exactly match each other. The LIR design is closer to this in the outer part of the blade, though there are still differences. The angle of attack (AOA) at the blade is lower in the LIR design, as the required lift is also lower.

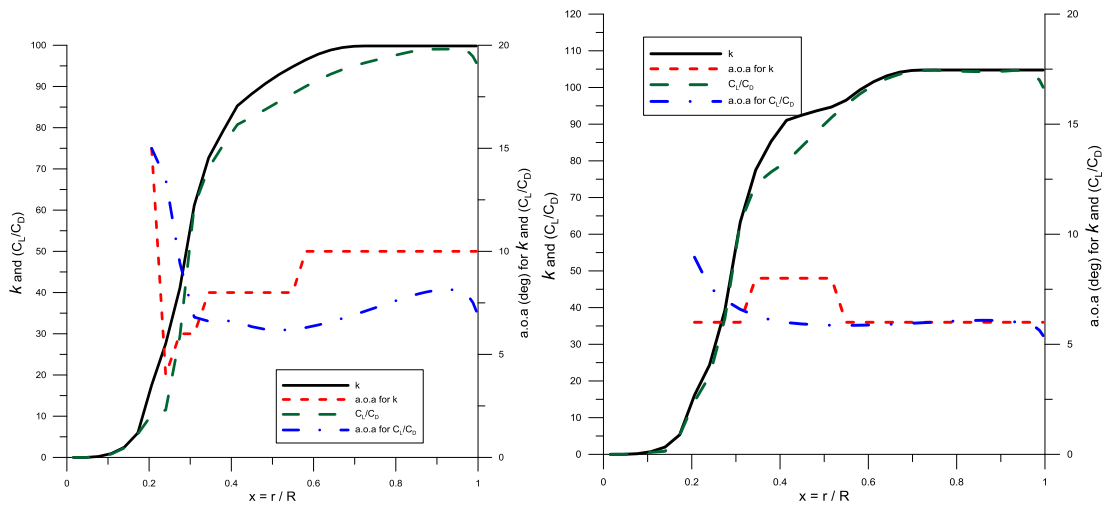


Figure 7. Normalized radial distributions of the lift over drag and the corresponding angle of attack at design conditions. RWT (left) vs LIR with varying axial induction (right)

Rotor Operating Conditions

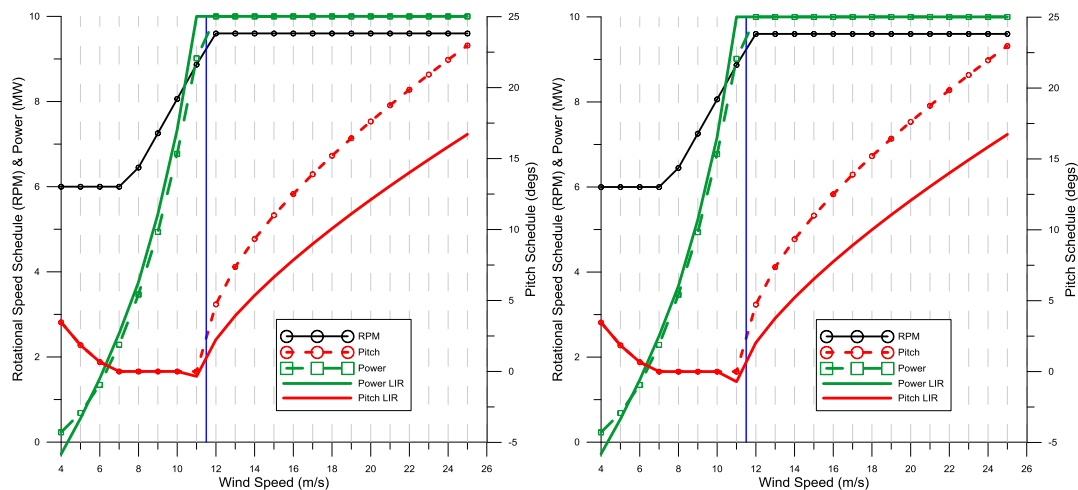


Figure 8. Rotational speed and pitch schedule as a function of the wind speed (two designs for LIR). RWT vs LIR (3.6% more AEP)

Details about the operating range of the RWT are given in [8]. The LIR follows the same rotational speed schedule, with a range of 6 – 9.6 RPM. The pitching schedule for low speeds remains the same, with limited pitch action to facilitate start-up. At speeds above rated the pitching schedule is modified, in order to retain the same rated power as the RWT (10 MW). The LIR reached the rated power at a reduced wind speed and in general produces greater power at speeds below rated. The differences between the two alternative chord distributions for LIR are practically negligible. The rotational speed / pitching schedule of the RWT used here were provided by DTU [16] with a wind-speed resolution of 1 m/s. The initial schedule was slightly modified in order to ensure a flat power at speeds over 11.5 m/s in all cases.

In order to get a better insight on the performance of the proposed rotor we present some details based on rotor power (P), thrust (T), torque (Q) and thrust bending moment $M(r)$ (at a given radial position) and the relevant non-dimensional coefficients C_{xx} defined through the following relations:

$$P = \frac{1}{2} \rho \pi R^2 V^3 C_P \quad (15)$$

$$T = \frac{1}{2} \rho \pi R^2 V^2 C_T \quad (16)$$

$$Q = \frac{1}{2} \rho \pi R^3 V^2 C_Q \quad (17)$$

$$M(x) = \frac{1}{2} \rho \pi R^3 V^2 C_{BM(x)} \quad (18)$$

The variation of these quantities is given for the full range of expected wind speeds, for the design with the linear variation of chord (the results for the alternative design are very similar).

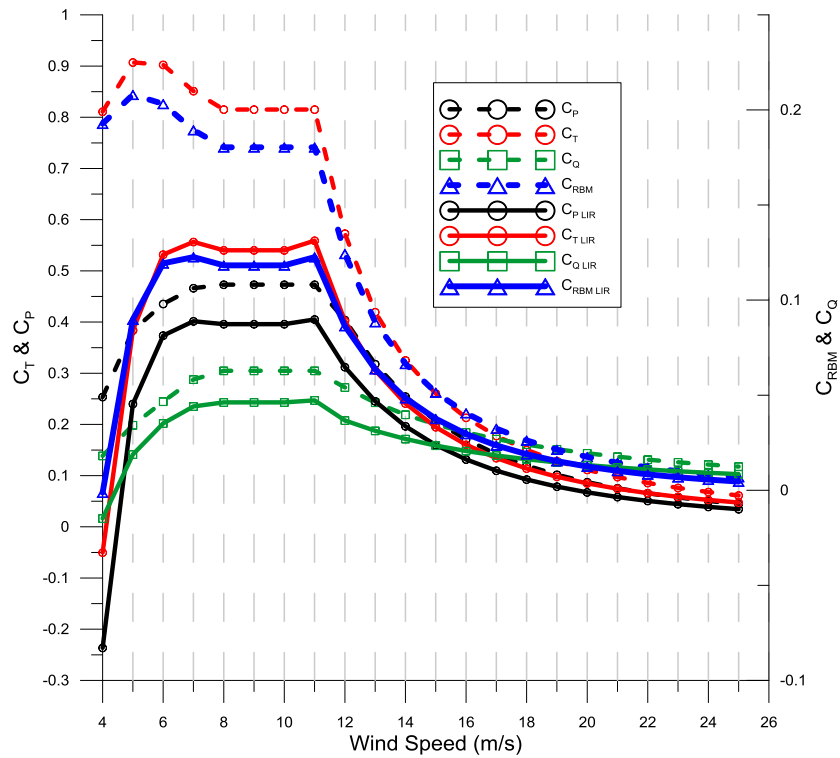


Figure 9. Pressure, thrust, torque (C_Q) and root bending moment coefficients (C_{RBM}) versus the wind speed. RWT vs LIR (varying axial induction)

In Figure 9 we present the variation of the above four coefficients with the wind speed, ranging from its cut-in to its cut-out value. The respective values for the RWT are also shown. As can be seen from the figure the coefficients are practically constant in the variable speed region and are adjusted to the desired power level after rated wind speed. The power coefficient maximum value is reduced from 0.473 to ~0.4 for the LIR design. A more drastic change is observed in the thrust and bending moment (which is directly affected by thrust) coefficients, where maximum values are almost halved in the new design. As these values are however only observed at low speeds, a more meaningful comparison would be of the actual dimensional thrust and bending moment.

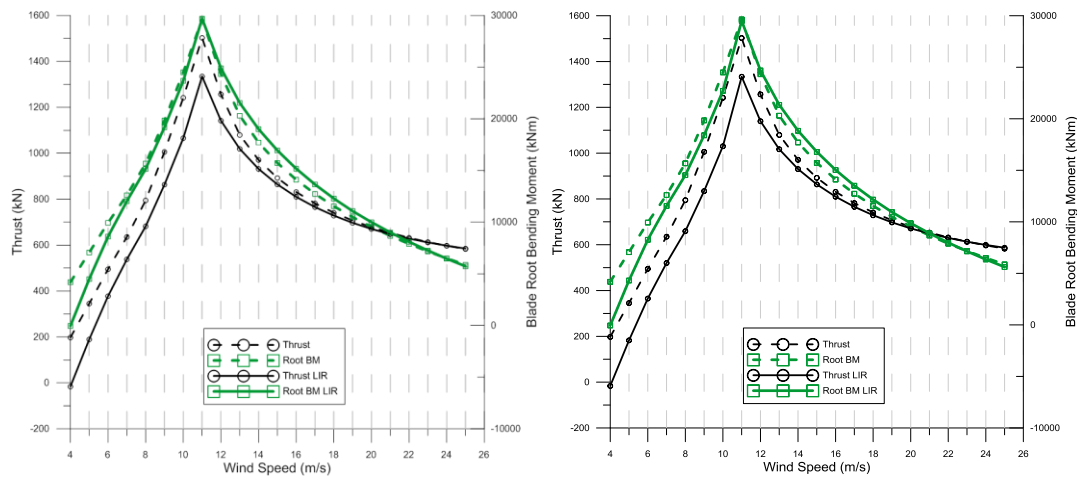


Figure 10. Dimensional thrust and root bending moment versus the wind speed. for fixed (right) and varying (left) axial induction LIR vs RWT.

The variation of rotor thrust and thrust bending moment at blade root over the wind speed operating regime is presented in Figure 10. As expected for pitch-variable speed designs, the maximum values of all three loads are obtained at rated wind speed. A non-negligible decrease of the thrust from ~ 1500 kN to ~ 1350 kN is observed for the LIR design, while the corresponding root bending moment (at $r=0$) is practically unaffected, as expected.

The reduction in thrust could result in reduced loads at the tower base, if the tower height were to remain the same. In order to keep the blade clearance from the water level constant however, it is necessary to increase the tower height, following the blade length increase. Therefore the moment at the tower base will remain close to the RWT value (a $\sim 10\%$ increase in height, compensated by a $\sim 10\%$ decrease in thrust). The advantage is that as there is no increase in the moment, the tower height increase can be accomplished with a favourable weight increase of the structure.

Conclusion

The concept of a Low Induction Rotor was evaluated in this report. The evaluation included

- Initial theoretical investigation of the concept, demonstrating that a low induction high swept area rotor can capture more energy than a conventional design that aims at $C_{P,MAX}$, without a penalty on the aerodynamic loading of the blades.
- Evaluation using a BEM model, resulting in a modified version of the reference wind turbine. Two variations on the design were used without noticeable differences in the results. The main characteristics of the resulting design are
 - The axial induction factor is chosen to have a value of ~ 0.2 (as opposed to 0.33, typical for C_{p_max} designs)
 - CC_L/R drops 50-60% but the original chord is more or less maintained for structural reasons
 - Rotor radius is increased by 13%
 - C_L design (where L/D is max) has to come down to 0.80, meaning that a new family of airfoils is needed. Realistic specifications have been given, it remains to be seen how these can be realized.
- Comparison of key performance parameters to the RWT, including

- Energy capture, where a 3.5% improvement of AEP compared to the RWT is observed
- Loads, a 10% reduction in thrust is obtained, while retaining the same blade root bending moment

The analysis has shown that an increase in energy capture and a decrease in levelised cost of energy are possible for such a design. The required performance of airfoils has also been shown, through the lift-drag curves used. In following tasks of the projects detailed design of such blade sections will be undertaken, to check if the prescribed levels of performance are attainable.

CENER: OTHER CONCEPTS, DOWNWIND ROTOR AND THE TOWER SHADOW EFFECT

Ainara Irisarri, Alfredo Martinez, and Xabier Munduate

Introduction

The aim of CENER in this task is to evaluate the influence of the tower shadow in blade design for different turbine configurations: 3 bladed upwind, 3 bladed downwind and 2 bladed downwind.

To evaluate that, comparisons of AoA-azimuth, Cl-azimuth, RotorPower-azimuth, RotorCq-azimuth and TSR-azimuth have been performed both with the tower shadow effect disabled and with the tower shadow effect enabled.

The software used for this purpose is the NREL code FAST (v7.02.00d-bjj, 20-Feb-2013) with AeroDyn (v13.00.02a-bjj, 20-Feb-2013) [9].

Wind turbine configurations

Name	3BI Upwind	3BI Downwind	2BI Downwind
Number of blades	3	3	2
Upwind/downwind	Upwind	Downwind	Downwind
Blade design	10MW model of the project	10MW model of the project	10MW model of the project
$\omega_{at V_m}$ (rpm)	8.03	8.03	9.8
ω_{max} (rpm)	9.6	9.6	11.7171
$\lambda_{at V_m}$	7.5	7.5	9.157
Pitch at V_m (deg)	0	0	0
Pitch at V_r (deg)	2.2	2.2	2.2
Yaw (deg)	0	0	0
aerofoils	originals 2D DTU	originals 2D DTU	originals 2D DTU

Table 2: wind turbine configurations

The increase in ω in the two-bladed case has been carried on to maintain the same torque as of the three-bladed case.

Computed cases

For each of the previously described three wind turbine configurations, cases with and without tower shadow effect have been computed. The aim has been to compare and evaluate the obtained results in order to get conclusions about how considering the tower shadow affects to the blade design.

Tower shadow model used:

A model that distorts the flow around the tower for both upwind (based on the work of Bak) and downwind (based on the work of Powles) rotors, as described in the “Tower Influence” section of the AeroDyn Theory Manual [1]. For the upwind configuration, the downwind tower shadow wake effect has been disabled, while for downwind configurations it has been enabled.

Dynamic Stall:

All computed cases have the dynamic stall model based on the works of Beddoes and Leishman enabled.

Tip and Hub loss models:

All computed cases have the tip and hub loss models of Prandtl enabled.

Inflow model:

An equilibrium wake model used. Considers that, at each time step, the stall is completely developed.

All simulated cases are with constant wind speed with no shear and constant rotor speed. The rotor speed values are described in Table 2.

Different conditions have been represented for different results:

- AoA-azimuth, Cl-azimuth, RotorPower-azimuth and RotorCq-azimuth have been obtained for the average and rated wind speed conditions.
- AoA-azimuth and Cl-azimuth have been analysed at 50%L and 70%L sections.
- TSR-azimuth has been calculated for Vm conditions.

Results

Simulations performed at Vm=10 m/s

Variations of angle of attack and Cl in one revolution of a blade have been analyzed in the sections 50%L and 70%L at mean wind speed, and are shown in the next figures.

Figures from 11 to 26 follow the next legend. As a guide, a summarized legend will be put in every figure.

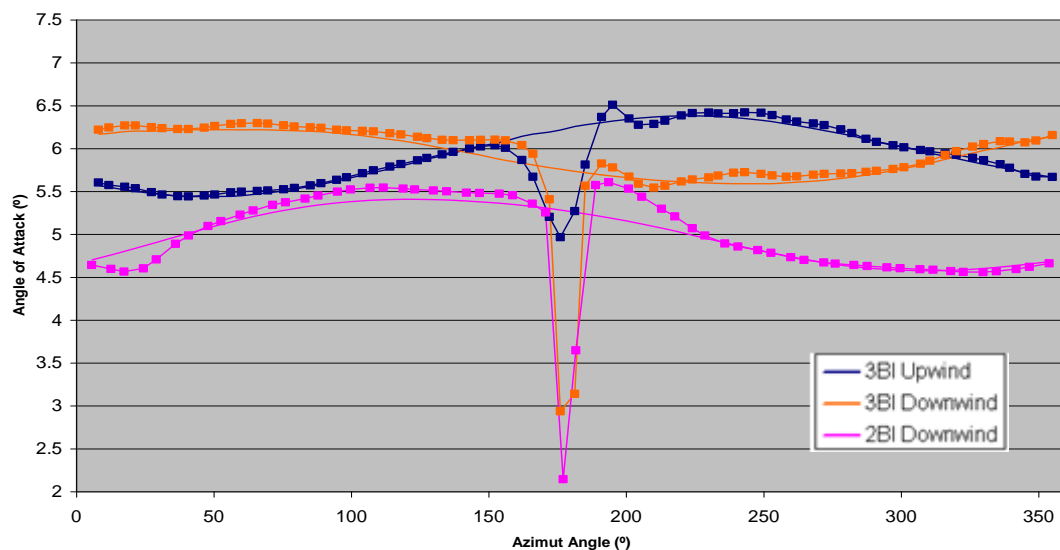
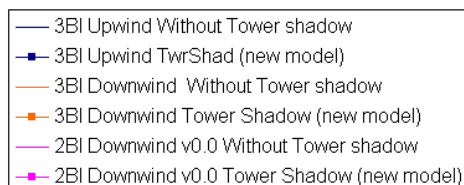


Figure 11: AoA-azimuth at Vm=10m/s at 50% blade length section (r=47.53m)

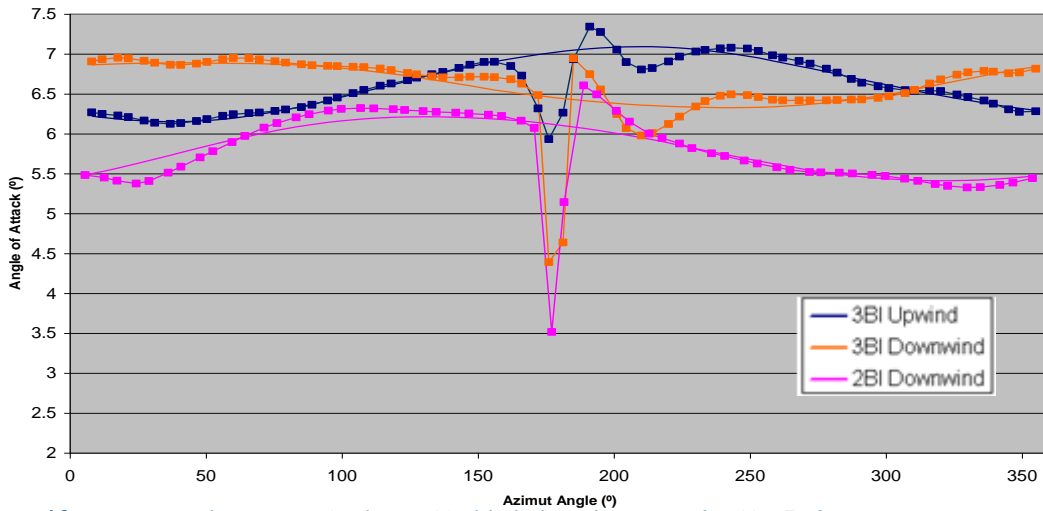


Figure 12: AoA-azimuth at $V_m=10\text{m/s}$ at 70% blade length section ($r=63.45\text{m}$)

To evaluate the speed of the changes seen above, AoA-t has also been plotted:

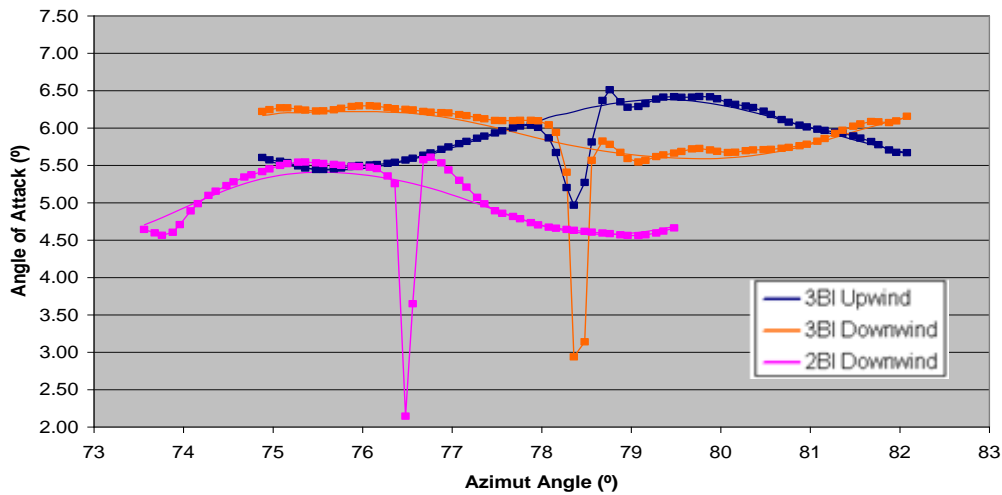


Figure 13: AoA-t at $V_m=10\text{m/s}$ at 50% blade length section ($r=47.53\text{m}$)

	Section	Δt (s)	AoA range (deg)	ΔAoA (deg)	$\Delta \text{AoA} / \Delta t$
3Bladed Upwind	50%L	1.4	6.51 - 4.97	1.54	1.1
3Bladed Downwind	50%L	1.12	6.10 - 2.94	3.16	2.821
2Bladed Downwind	50%L	1	5.61 - 2.15	3.46	3.46

Table 3: AoA and time increments at 50%section for V_m

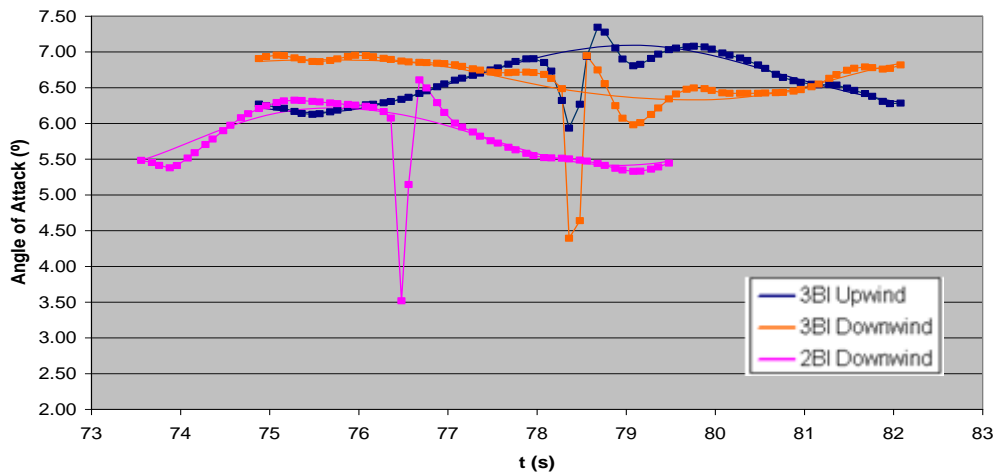


Figure 14: AoA-t at $V_m=10\text{m/s}$ at 70% blade length section ($r=63.45\text{m}$)

	Section	Δt (s)	AoA range (deg)	ΔAoA (deg)	$\Delta \text{AoA} / \Delta t$
3Bladed Upwind	70%L	1.6	7.34 - 5.93	1.41	0.881
3Bladed Downwind	70%L	1.2	6.95 - 4.39	2.56	2.133
2Bladed Downwind	70%L	0.88	6.61 - 3.52	3.09	3.511

Table 4: AoA and time increments at 70%section for V_m

Changes at 3 bladed downwind case occur around 2.5 times faster than at 3 bladed upwind case. Changes at 2 bladed downwind case occur around 3 times faster than at 3 bladed upwind case.

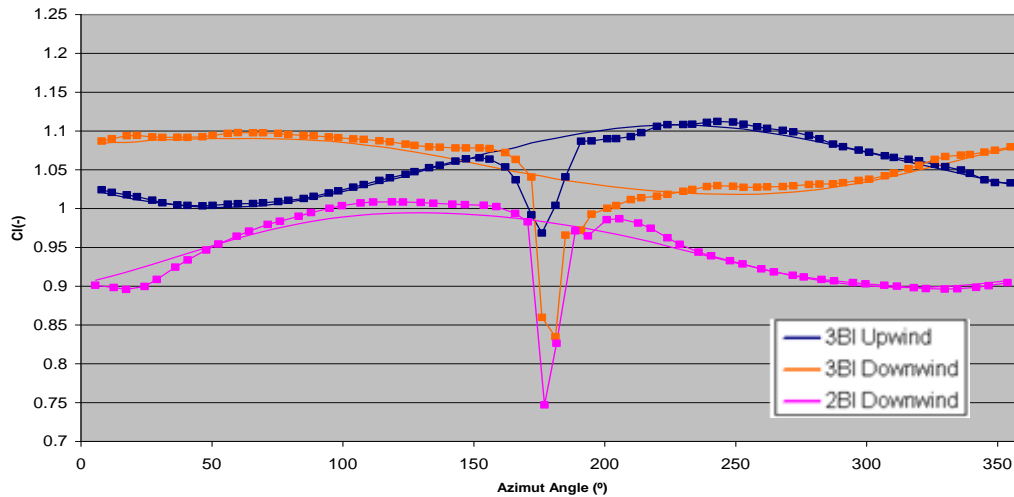


Figure 15: C_l -azimuth at $V_m=10\text{m/s}$ 50% blade length section ($r=47.53\text{m}$)

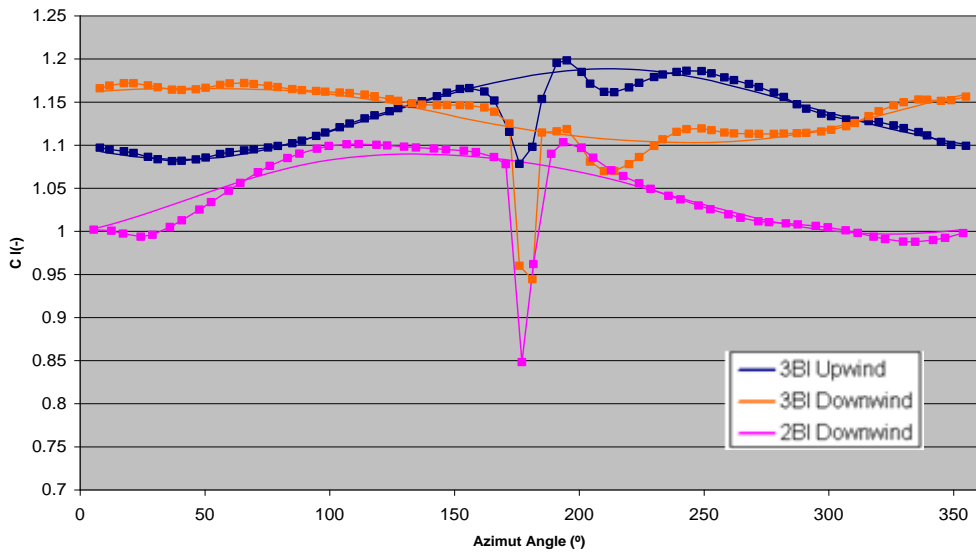


Figure 16: C_l -azimuth at $V_m=10\text{m/s}$ 70% blade length section ($r=63.45\text{m}$)

Both for AoA and C_l , the amplitude of the effect in downwind cases is around 2.5 times the amplitude of the effect in the upwind case. The range of azimuths at which the strong effect happens is similar in upwind and downwind cases, and takes around 50° .

In 3 bladed cases, the strong tower shadow effect is located around 180° and is almost negligible in the rest of the azimuth. In the 2 bladed case, apart from the strong effect, there is also a lighter effect from 0° - 180° azimuth.

Also, variations of rotor power and rotor torque coefficient in one revolution of a blade have been analysed, as shown below:

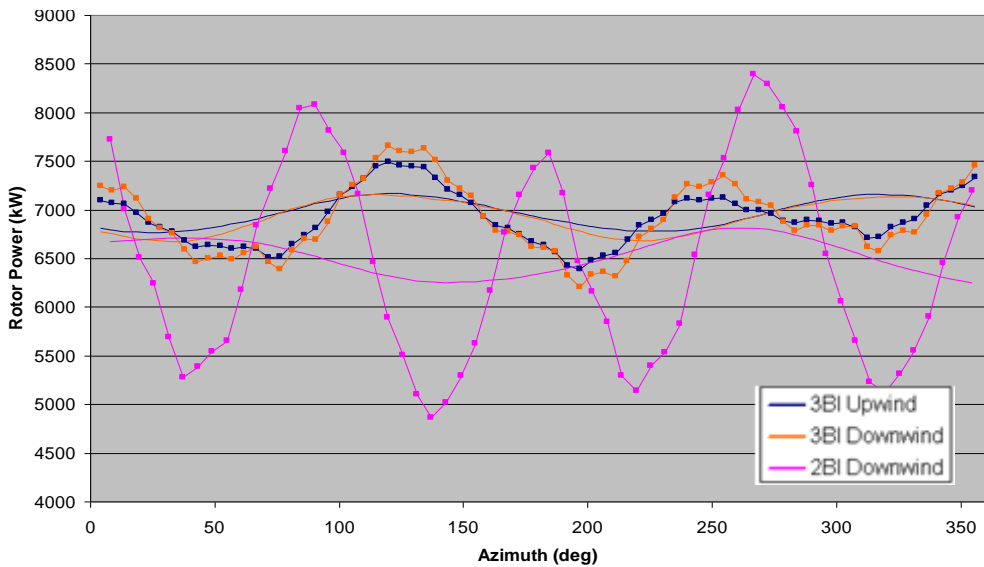


Figure 17: RotorPower-azimuth at $V_m=10\text{m/s}$

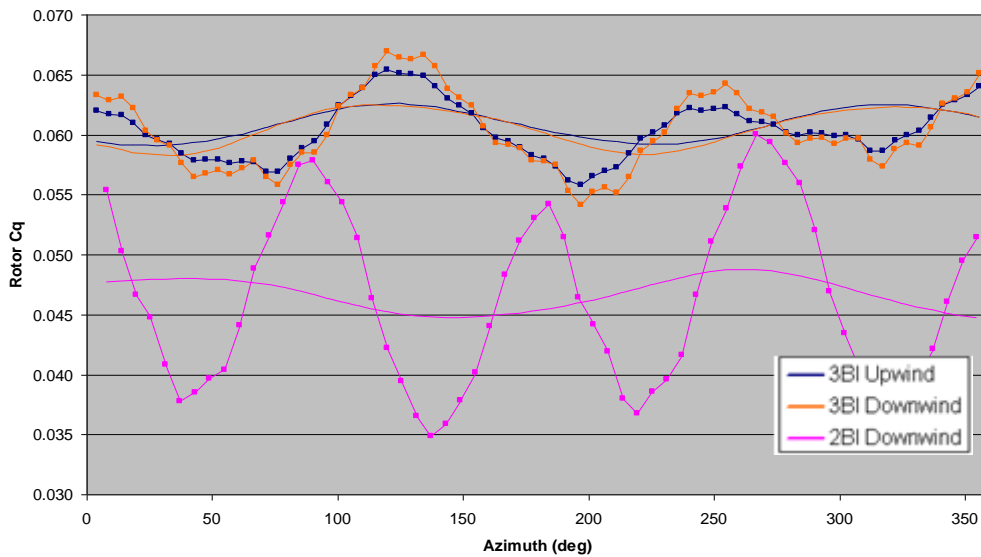


Figure 18: RotorCq-azimuth at $V_m=10\text{m/s}$

About the behaviour of rotor power and rotor torque coefficient in one revolution, it has to be said that without tower shadow, the amplitude of the variation is similar for the three cases, although the mean value is lower in the 2 bladed case.

In general, the tower shadow effect makes the frequency of the variation to be higher and the amplitude bigger. However, the mean values do not change significantly with and without tower shadow.

The amplitude of the 3 bladed downwind case is a bit bigger than in the 3 bladed upwind case, and in the 2 bladed case is around twice the 3 bladed upwind case's.

Simulations performed at $V_r=11.4\text{ m/s}$

Variations of angle of attack and Cl in one revolution of a blade have been analysed in the sections 50%L and 70%L at rated wind speed, and are shown in the next figures.

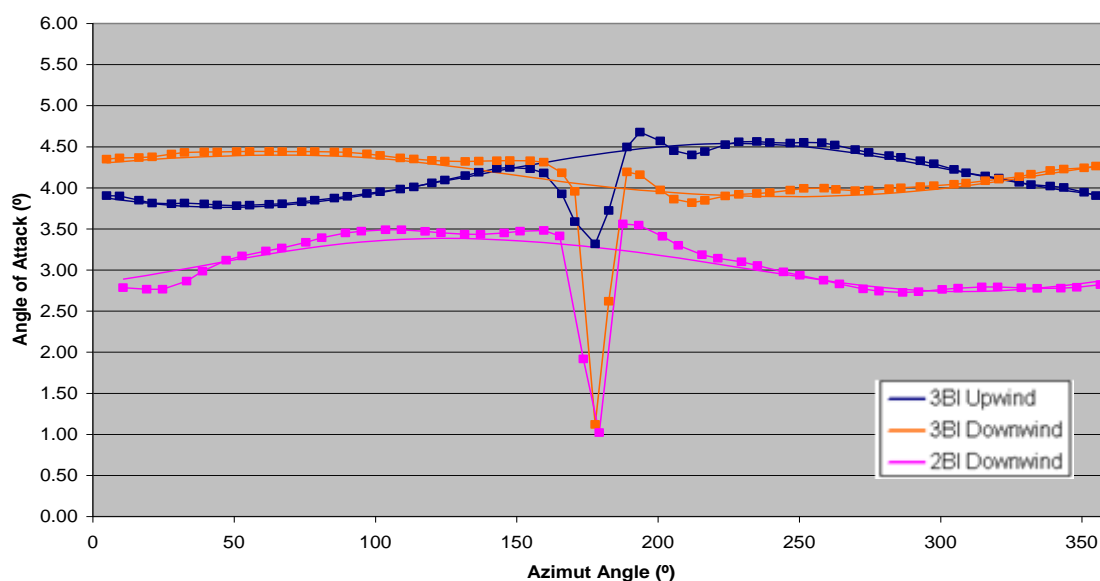


Figure 19: AoA-azimuth at $V_r=11.4\text{m/s}$ at 50% blade length section ($r=47.53\text{m}$)

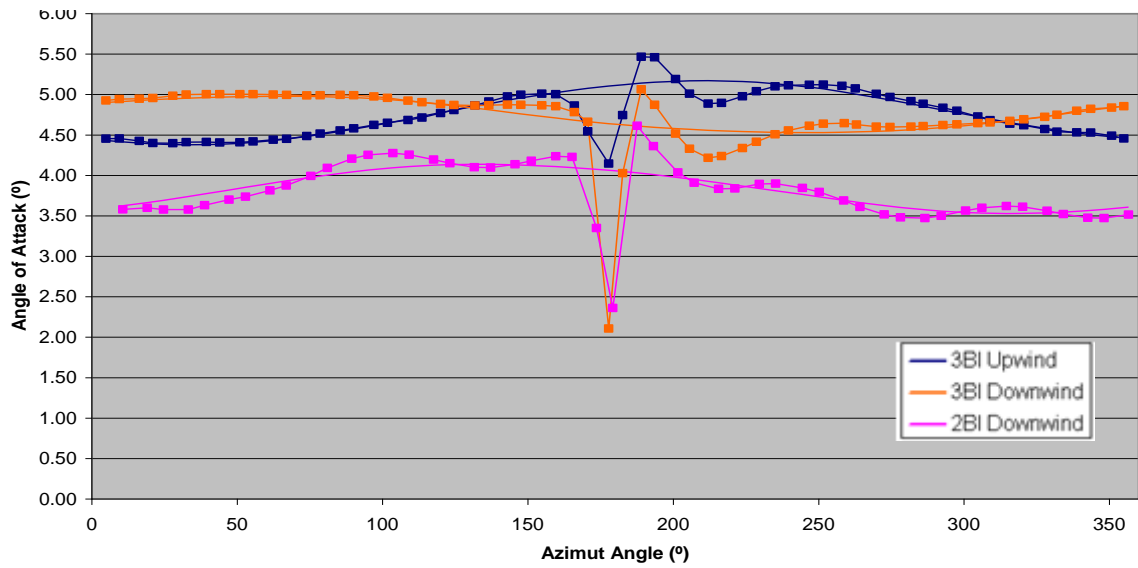


Figure 20: AoA-azimuth at Vr=11.4m/s at 70% blade length section (r=63.45m)

To evaluate the speed of the changes seen above, AoA-t has also been plotted:

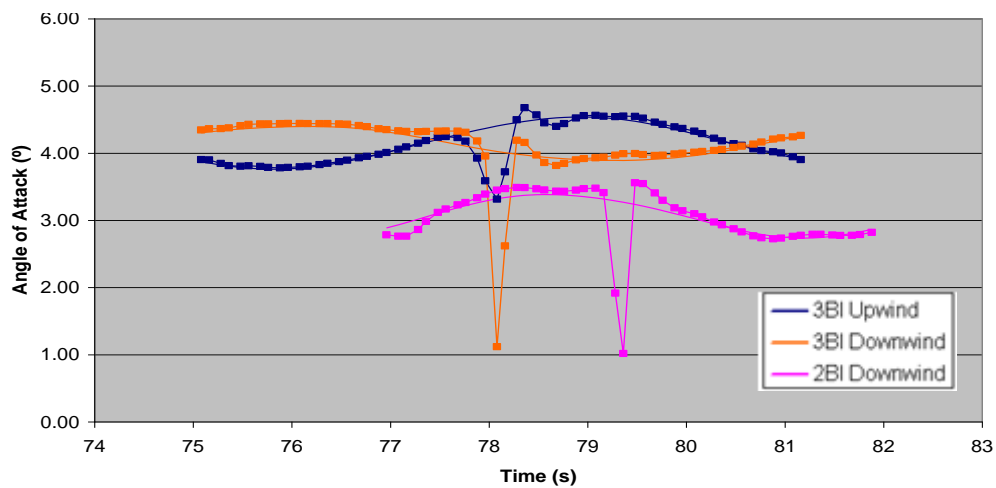


Figure 21: AoA-t at Vr=11.4m/s at 50% blade length section (r=47.53m)

	Section	Δt (s)	AoA range (deg)	ΔAoA (deg)	$\Delta AoA / \Delta t$
3Bladed Upwind	50%L	1.4	4.68 - 3.32	1.36	0.971
3Bladed Downwind	50%L	1	4.31 - 1.12	3.2	3.2
2Bladed Downwind	50%L	0.8	3.56 - 1.02	2.54	3.175

Table 5: AoA and time increments at 50%section for Vr

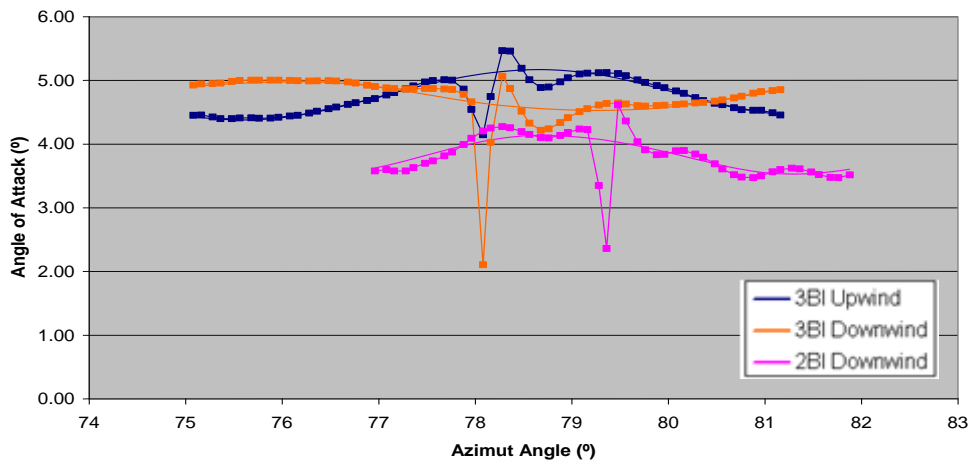


Figure 22: AoA-t at Vr=11.4m/s at 70% blade length section (r=63.45m)

	Section	Δt (s)	AoA range (deg)	ΔAoA (deg)	$\Delta AoA / \Delta t$
3Bladed Upwind	70%L	1.4	5.47 - 4.15	1.32	0.942
3Bladed Downwind	70%L	1.12	5.06 - 2.11	2.95	2.634
2Bladed Downwind	70%L	0.92	4.61 - 2.36	2.25	2.446

Table 6: AoA and time increments at 70%section for Vr

Changes at 3 bladed downwind case occur around 2.5-3 times faster than at 3 bladed upwind case. Changes at 2 bladed downwind case occur around 2.5-3 times faster than at 3 bladed upwind case.

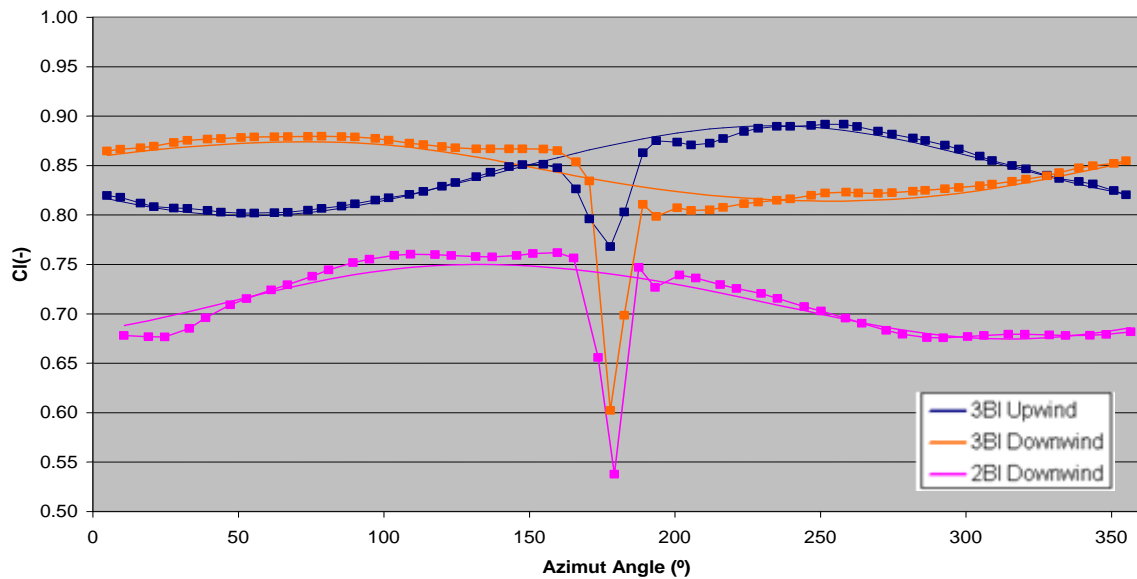


Figure 23: Cl-azimuth at Vr=11.4m/s at 50% blade length section (r=47.53m)

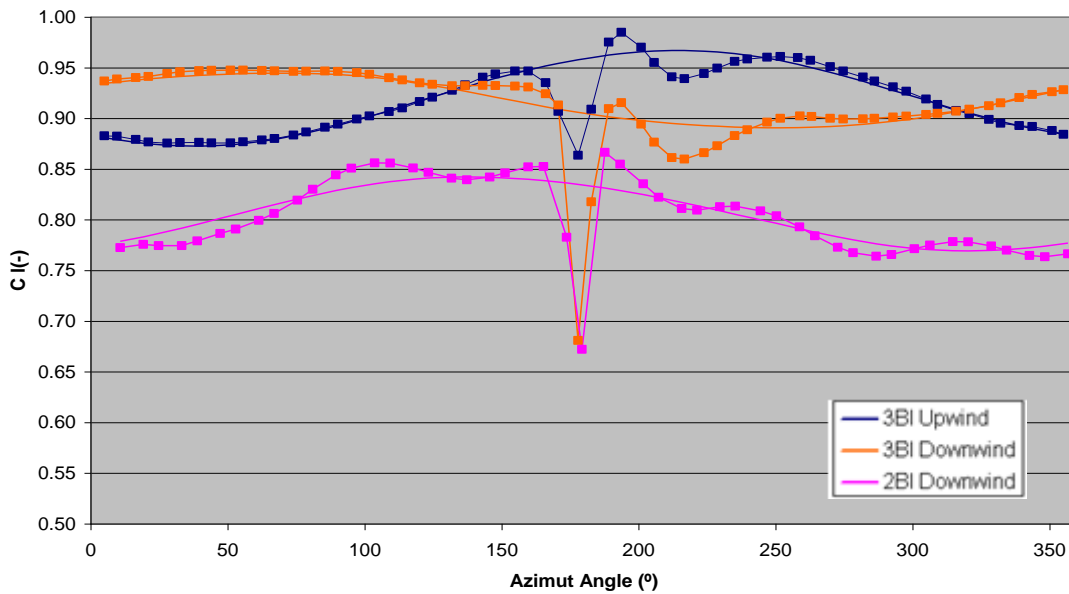


Figure 24: C_l -azimuth at $V_r=11.4\text{m/s}$ at 70% blade length section ($r=63.45\text{m}$)

Almost the same conclusions than for the case of V_m apply, but in this case at V_r , the effect at 3 bladed downwind case (2.5 times the upwind case's) is stronger than in the 2 bladed downwind case (2 times the upwind case's).

Variations of rotor power and rotor torque coefficient in one revolution of a blade have also been analysed, and are shown in the next figures:

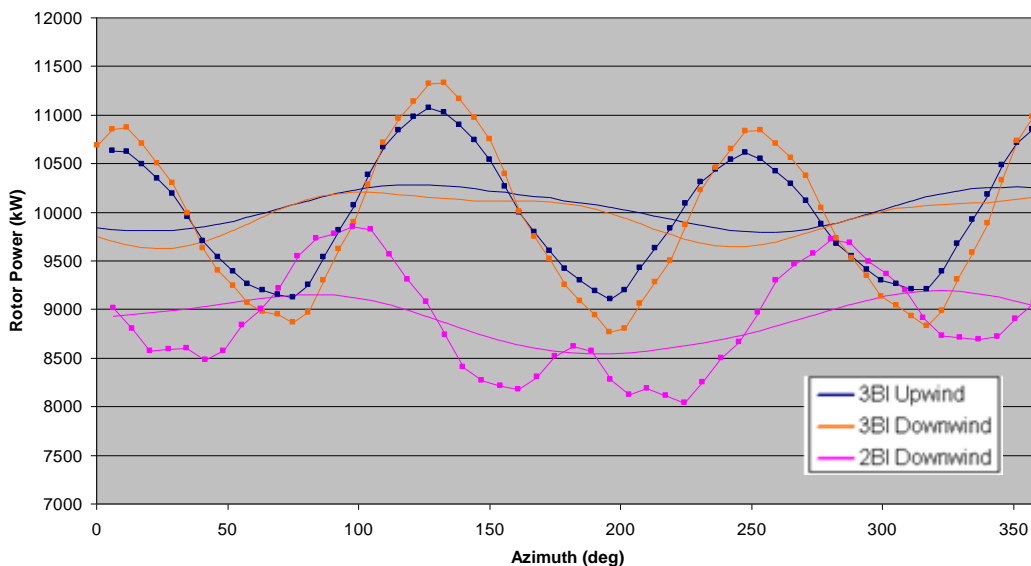


Figure 25: RotorPower-azimuth at $V_r=11.4\text{m/s}$

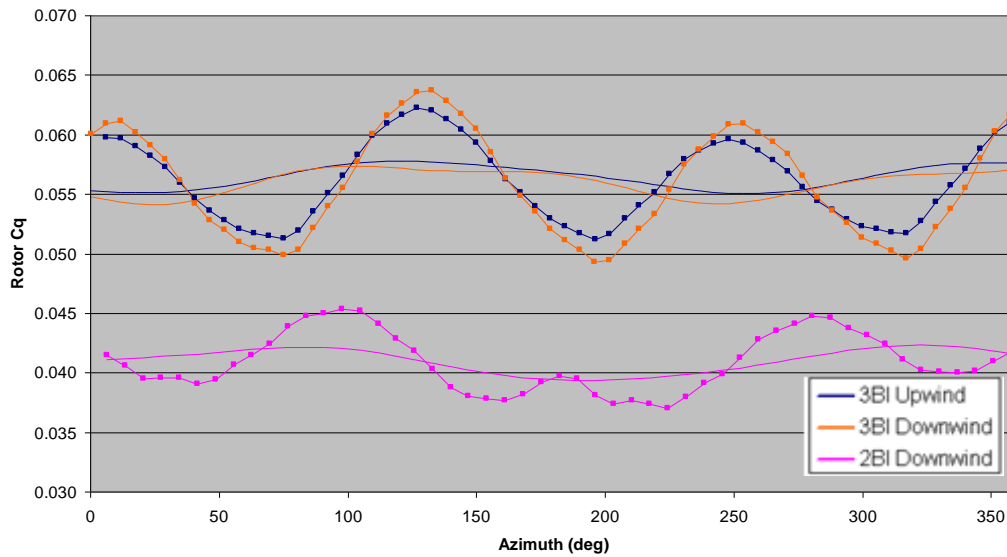


Figure 26: RotorCq-azimuth at $V_r=11.4\text{m/s}$

At rated wind speed, the interpretation of the results is almost the same than for the mean wind speed.

The strongest difference relies on the behaviour of the 2 bladed downwind case with tower shadow effect: the amplitude is more irregular. This does not happen in the 3 bladed cases, where the amplitude and frequency are similar for V_m and V_r .

The other difference is that in the cases at V_r the signals are smoother at rated wind speed than at mean wind speed.

TSR - azimuth

To evaluate the influence of the tower shadow in blade design, TSR has been calculated for the different azimuth positions for one blade (using AoA-azimuth data of the tip section of each blade configuration).

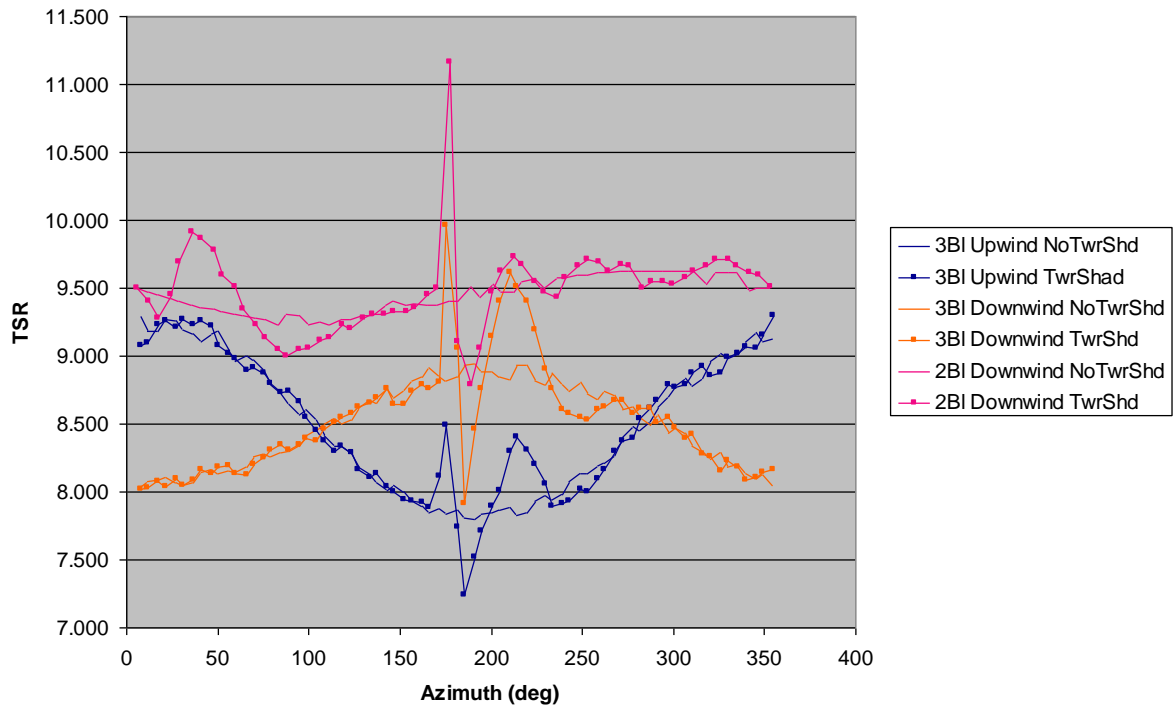


Figure 27: TSR-azimuth for the different turbine configurations

In the same way than with AoA, the amplitude of the effect in downwind cases is around 2.5 times the amplitude of the effect in the upwind case. The range of azimuths at which the strong effect happens is similar in upwind and downwind cases, and takes around 50°.

In 3 bladed cases, the strong tower shadow effect is located around 180° and is almost negligible in the rest of the azimuth. In the 2 bladed case, apart from the strong effect, there is also a lighter effect from 0°-180° azimuth.

Next figures show the results for each blade configuration separately.

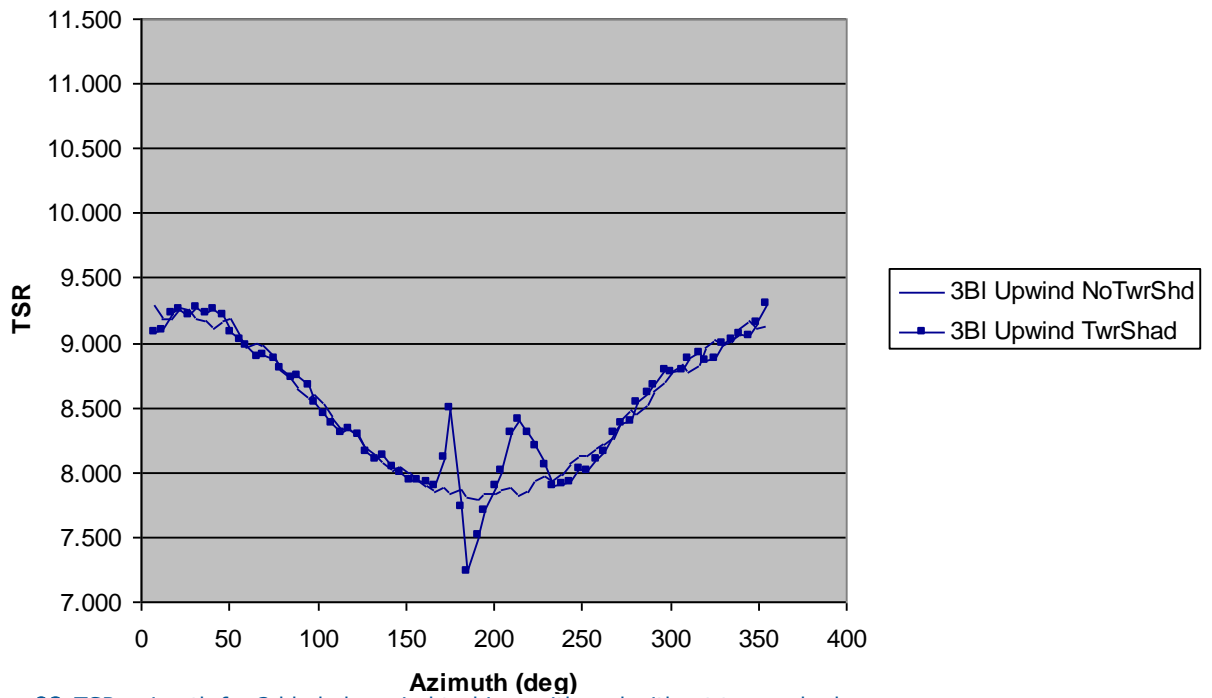


Figure 28: TSR-azimuth for 3 bladed upwind turbine, with and without tower shadow

In the 3 bladed Upwind case, it can be seen that without the effect, TSR values move from 7.83 to 9.27. With the tower shadow effect, TSR values move from 7.24 to 9.27.

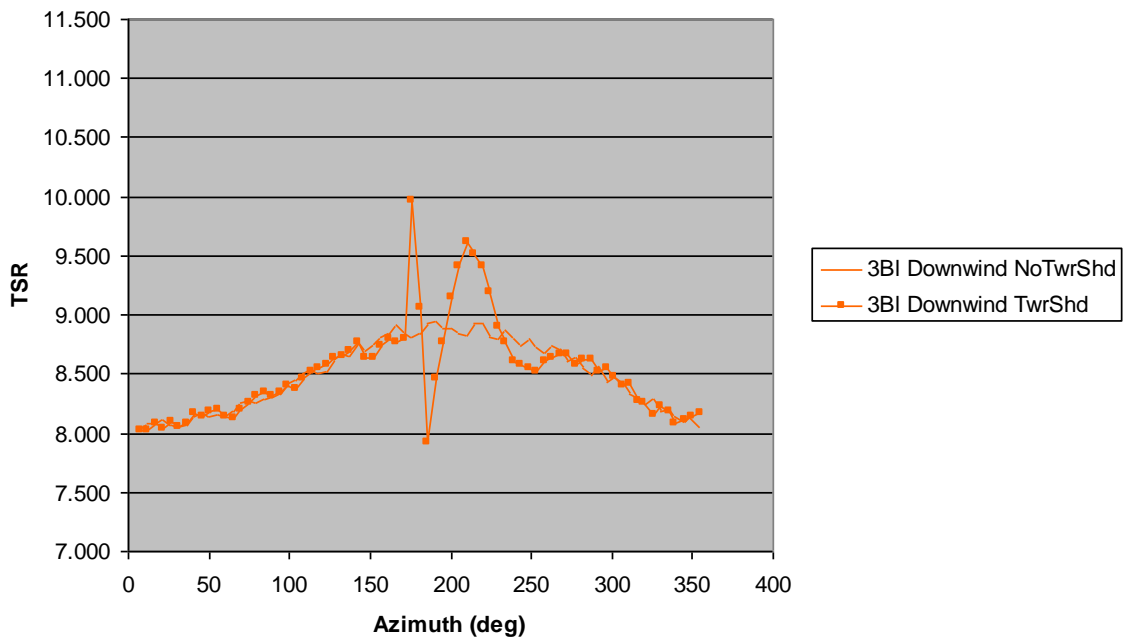


Figure 29: TSR-azimuth for 3 bladed downwind turbine, with and without tower shadow

In the 3 bladed downwind case, without the effect, TSR values move from 8.00 to 8.94. With the tower shadow effect, TSR values move from 7.91 to 9.96.

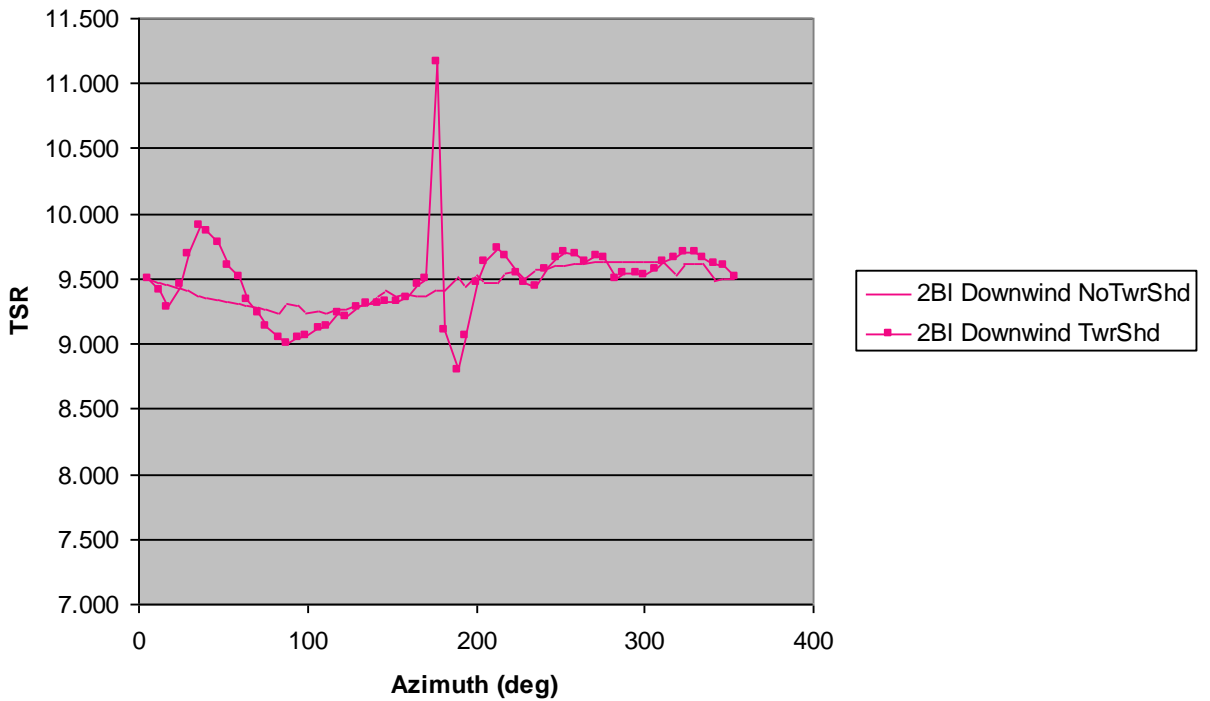


Figure 30: TSR-azimuth for 2 bladed upwind turbine, with and without tower shadow

In the 2 bladed downwind case, without the effect, TSR values move from 9.00 to 9.91. With the tower shadow effect, TSR values move from 8.79 to 11.16.

Unless a blade geometry that changes with azimuth is designed, to do a conventional design only one value of TSR is needed. So, the mean values around a revolution have been calculated.

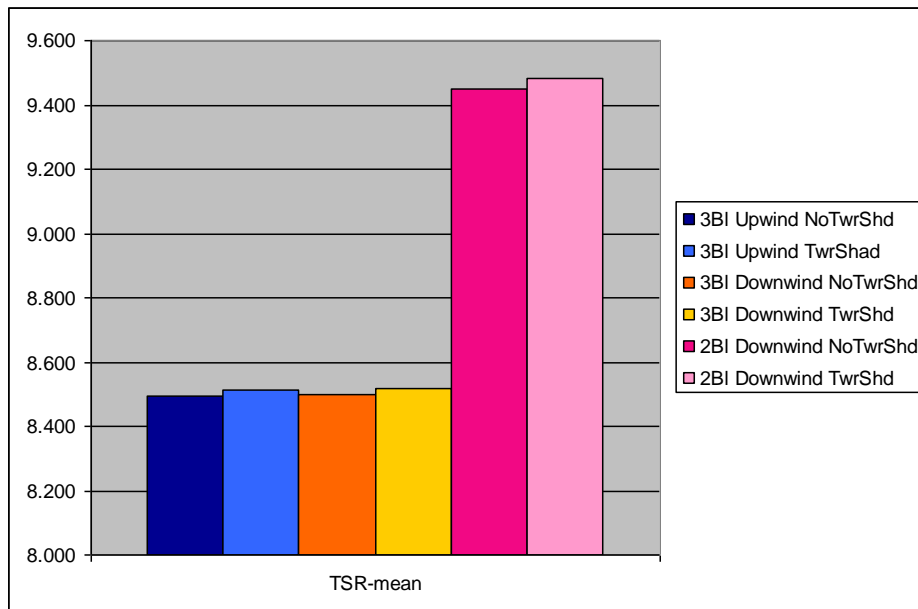


Figure 31: Mean TSR for different turbine configurations, with and without tower shadow

	NO TwrShd	TwrShd	Δ TSR	$\Delta\omega$	$\Delta\omega$ in % ω
3BI Upwind	8.496	8.511	0.0154	0.0165	0.206%
3BI Downwind	8.497	8.518	0.0211	0.0225	0.281%
2BI Downwind	9.450	9.481	0.0304	0.0326	0.332%

Table 7: Mean TSR, Δ TSR and $\Delta\omega$ for different turbine configurations, with and without tower shadow

Making the difference between mean TSR values, the conclusion is that tower shadow effect is stronger for downwind turbines, and stronger for 2 bladed turbines.

Trying to translate TSR values to design, increments of TSR have been turned into increments of ω (considering the wind speed as $V_m=10\text{m/s}$). The conclusion is that those increments in TSR are turned into an increment of ω between 0.206% ω_{rated} and 0.332% ω_{rated} .

Conclusions

- Tower shadow effect is stronger for downwind turbines, and stronger for 2 bladed turbines, both in intensity and speed.
- In general, the tower shadow effect makes the frequency of the variations of a variable to be higher and the amplitude bigger: less stable situation.
- Focusing on the behaviour of TSR in one revolution, tower shadow effects are significant during a short period of time, but when calculating the mean values of TSR with and without tower shadow effect in the whole range of time, results do not change significantly.
- The tower shadow effect cannot be coped only through a change in the blade geometry design. A blade geometry that changes with azimuth position is a possibility, or aerofoils that are designed to withstand unsteady aerodynamics.
- The way of considering the tower shadow effect in design could be focused on aerofoil design: design aerofoils where Cl variations are small with α variations, either through a fixed or through a variable aerofoil geometry.

CENER: COMPRESSIBLE FLOW BLADE DESIGN VERIFICATION AND HIGH TIP SPEED

Ainara Irisarri, Alfredo Martinez, Xabier Munduate

Introduction

The aim of CENER in this task is to evaluate the influence of the compressibility in blade design.

The work done in CENER to evaluate that consists in comparisons of C_p - λ , AEP, C_p , C_t , C_q and C_p/C_t of the reference 10MW wind turbine with three different sets of airfoil data, each of them considering a different compressibility assumption. The blade geometry is maintained as in the 10MW original wind turbine in all simulations.

The software used for this purpose is the NREL code FAST (v7.02.00d-bjj, 20-Feb-2013) with AeroDyn (v13.00.02a-bjj, 20-Feb-2013) [9].

Airfoil data used

The different sets of airfoil data used in this task have been obtained using XFOIL, doing 2D computations from -30° to 30° . Data out of that range has been taken from Original 2D DTU data, doing the joint as smooth as possible.

The details of each airfoil set used are shown in the next tables:

- Cener set 1: Mach =0 (incompressible flow).

	FFA-W3-600	FFA-W3-480	FFA-W3-360	FFA-W3-301	FFA-W3-241
Re	Original 2D	1.00E+07	1.00E+07	1.00E+07	1.20E+07
Mach	DTU data	0	0	0	0

- Cener set 2: Mach of the case where $V_{tip}=90\text{m/s}$ (compressible flow, conventional tip speed).

	FFA-W3-600	FFA-W3-480	FFA-W3-360	FFA-W3-301	FFA-W3-241
Re	Original 2D	1.00E+07	1.00E+07	1.00E+07	1.20E+07
Mach	DTU data	0.073	0.09	0.11	0.26

- Cener set 3: Mach of the case where $V_{tip}=110\text{m/s}$ (compressible flow, high tip speed).

	FFA-W3-600	FFA-W3-480	FFA-W3-360	FFA-W3-301	FFA-W3-241
Re	Original 2D	1.00E+07	1.00E+07	1.00E+07	1.20E+07
Mach	DTU data	0.085	0.11	0.137	0.317

Next figures show C_l , C_d , C_m and C_l/C_d of each airfoil, for the 3 airfoil data sets:

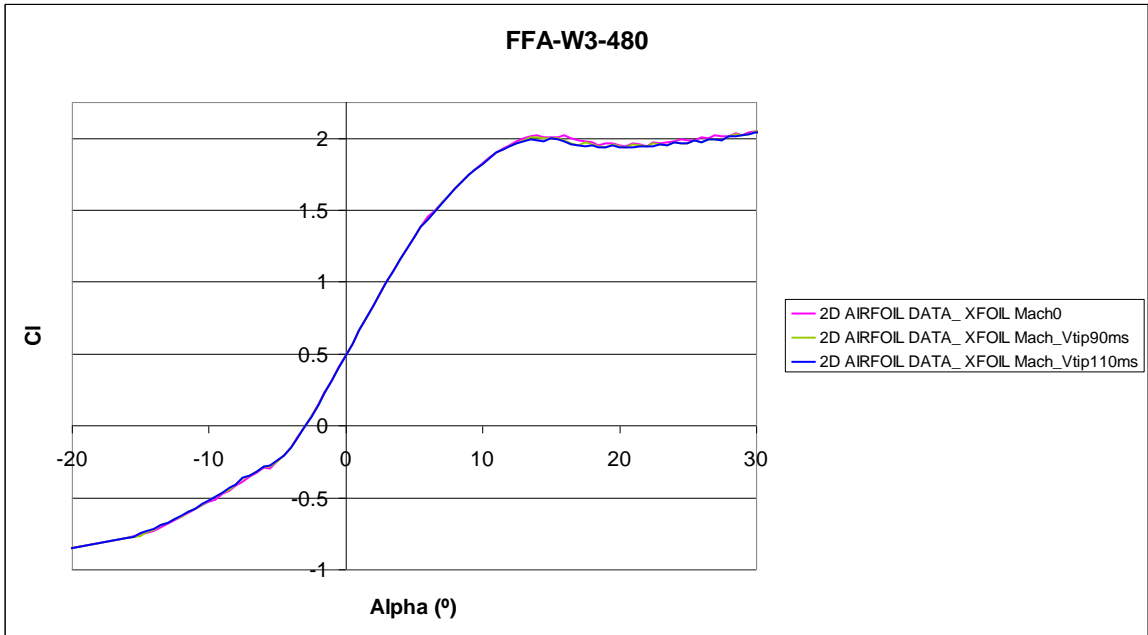


Figure 32: Cl-alpha of FFA-W3-480 airfoil computed with XFOIL for different Mach numbers

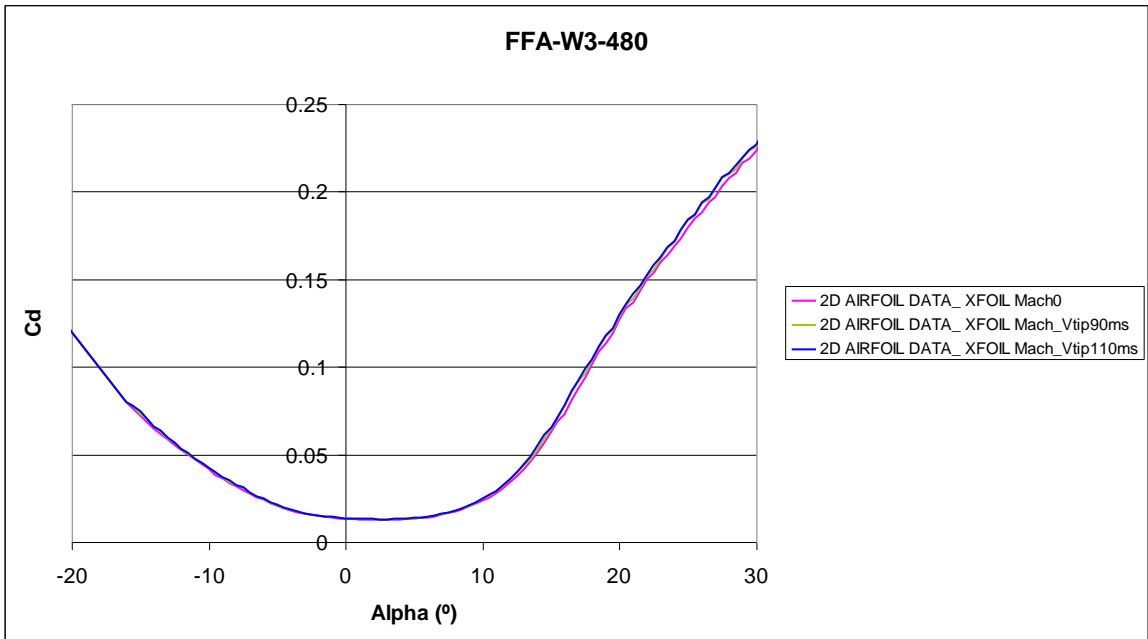


Figure 33: Cd-alpha of FFA-W3-480 airfoil computed with XFOIL for different Mach numbers

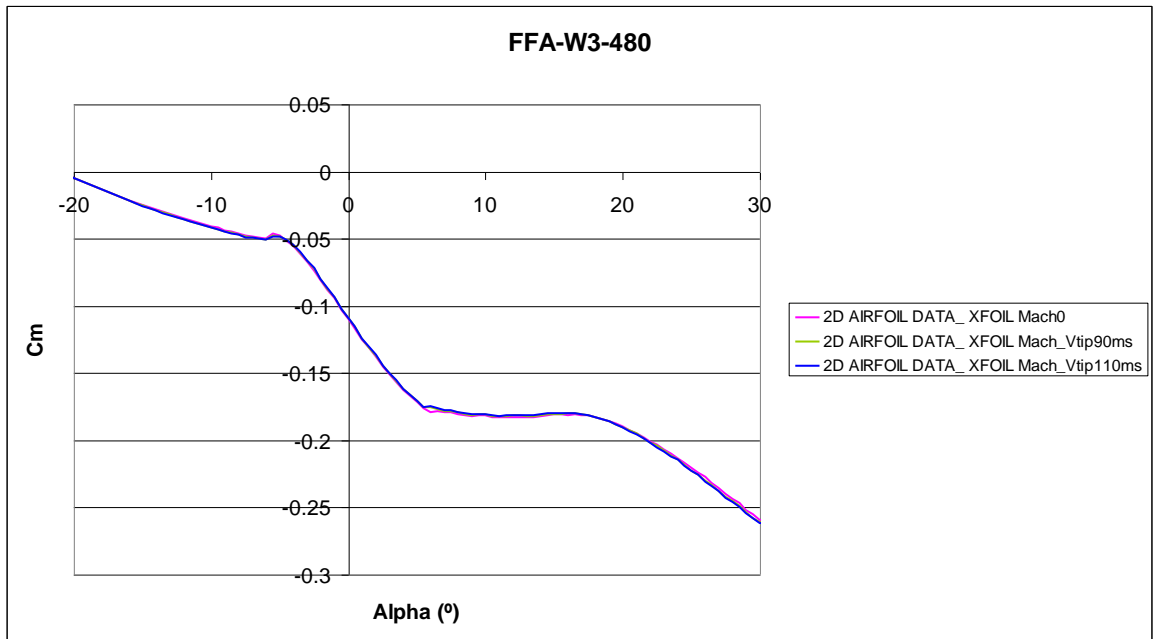


Figure 34: Cm-alpha of FFA-W3-480 airfoil computed with XFOIL for different Mach numbers

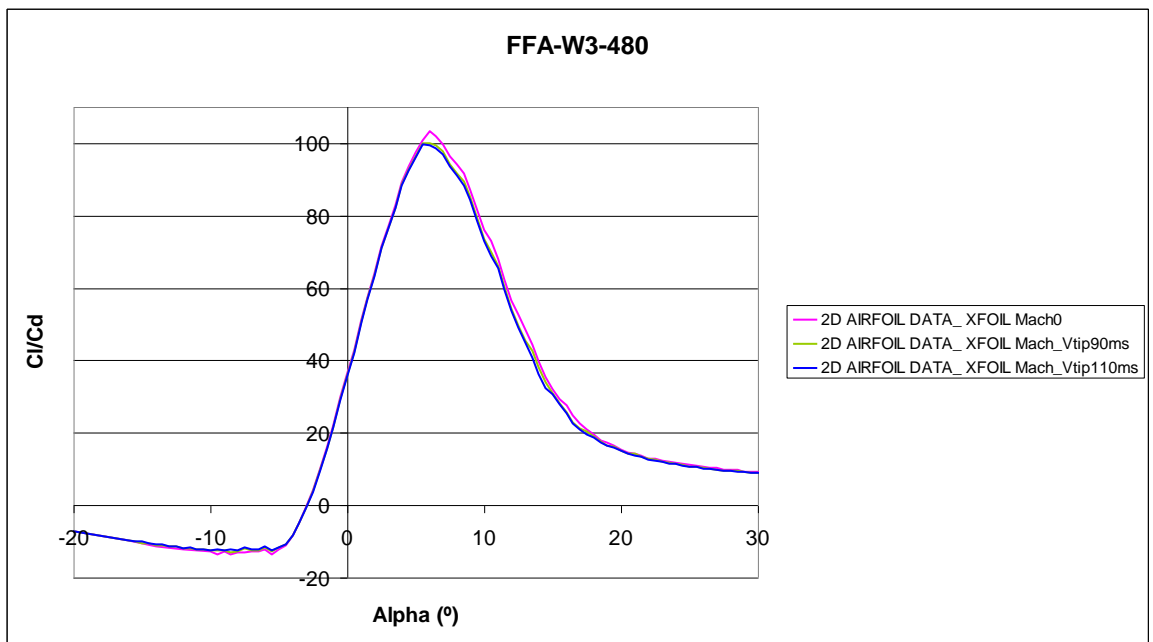


Figure 35: Cl/Cd-alpha of FFA-W3-480 airfoil computed with XFOIL for different Mach numbers

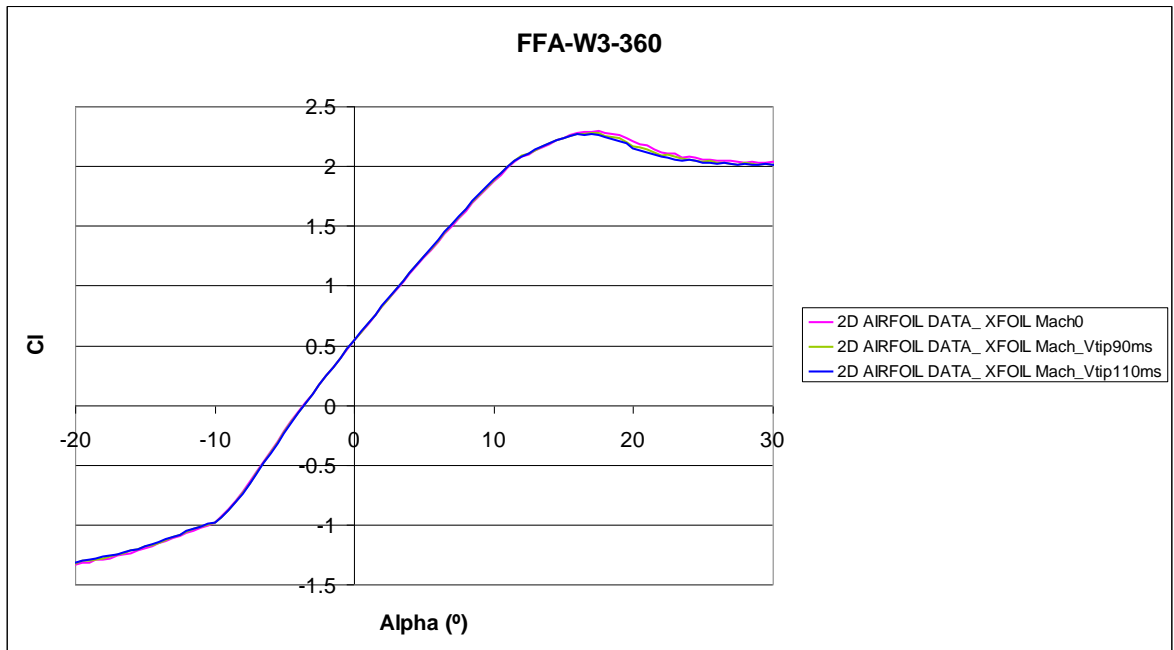


Figure 36: Cl-alpha of FFA-W3-360 airfoil computed with XFOIL for different Mach numbers

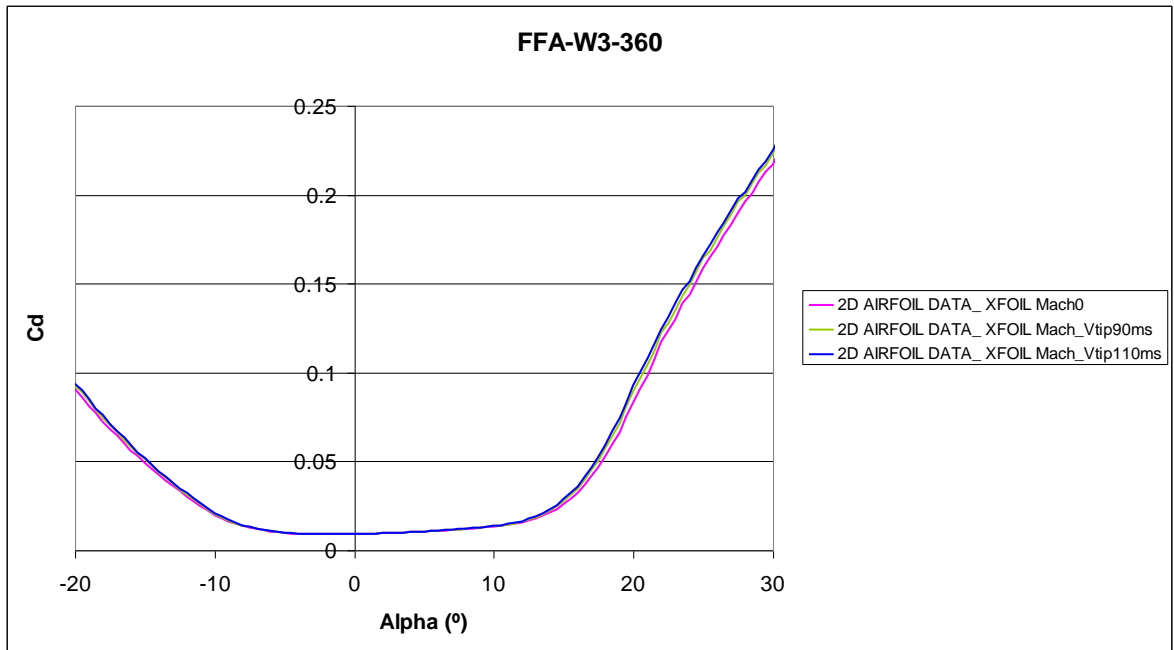


Figure 37: Cd-alpha of FFA-W3-360 airfoil computed with XFOIL for different Mach numbers

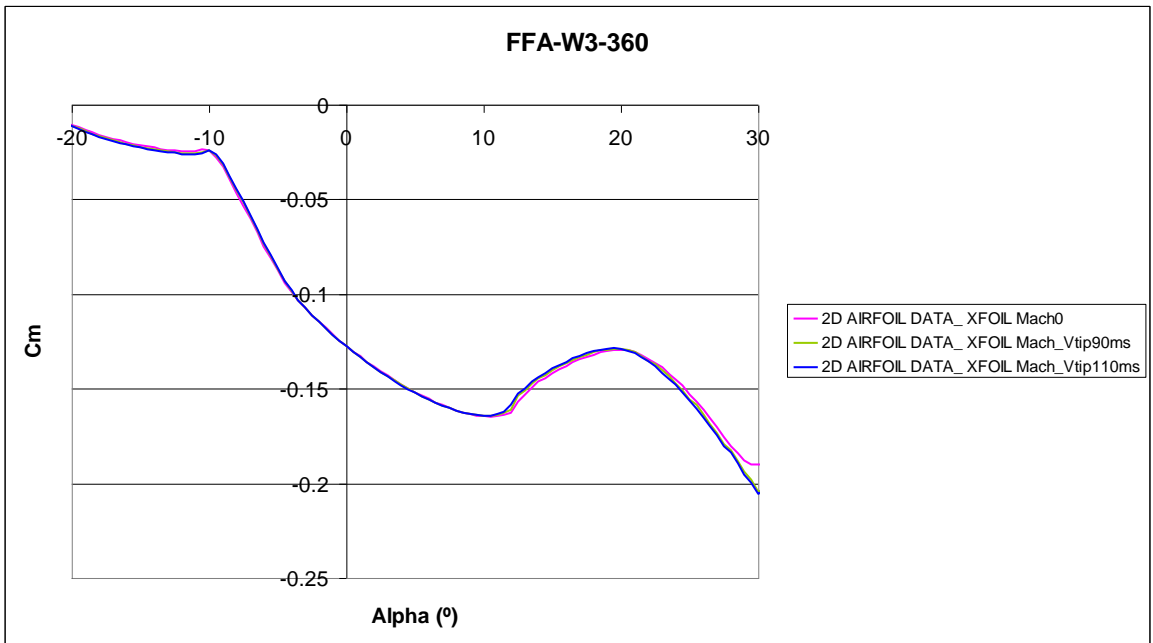


Figure 38: Cm-alpha of FFA-W3-360 airfoil computed with XFOIL for different Mach numbers

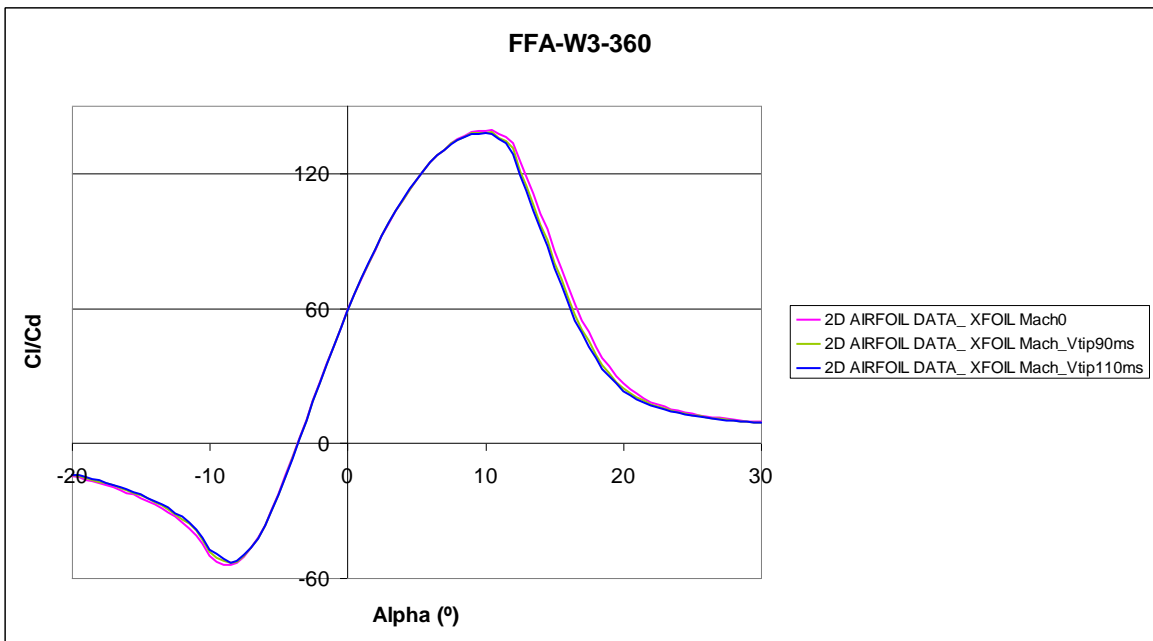


Figure 39: Cl/Cd-alpha of FFA-W3-360 airfoil computed with XFOIL for different Mach numbers

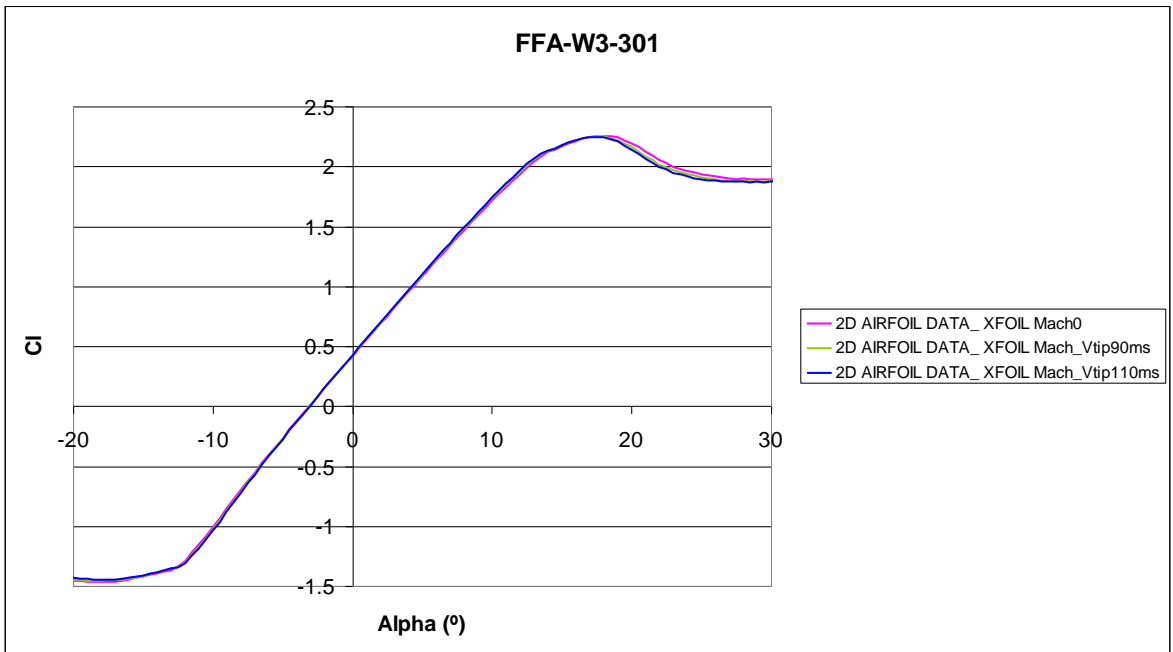


Figure 40: C_l -alpha of FFA-W3-301 airfoil computed with XFOIL for different Mach numbers

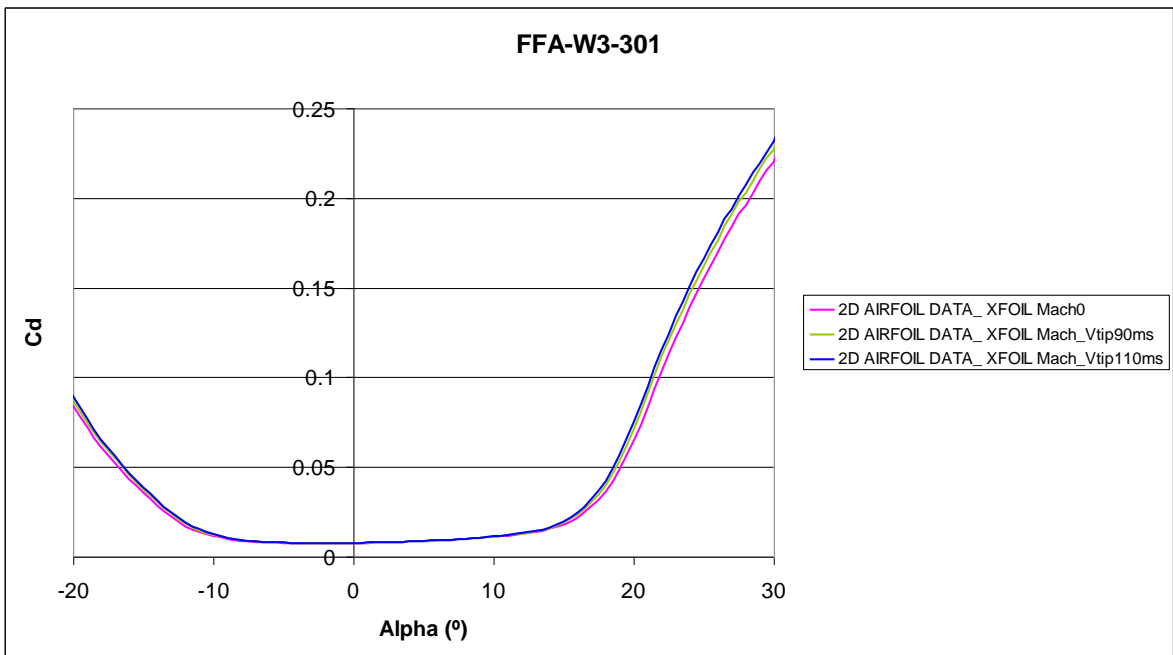


Figure 41: C_d -alpha of FFA-W3-301 airfoil computed with XFOIL for different Mach numbers

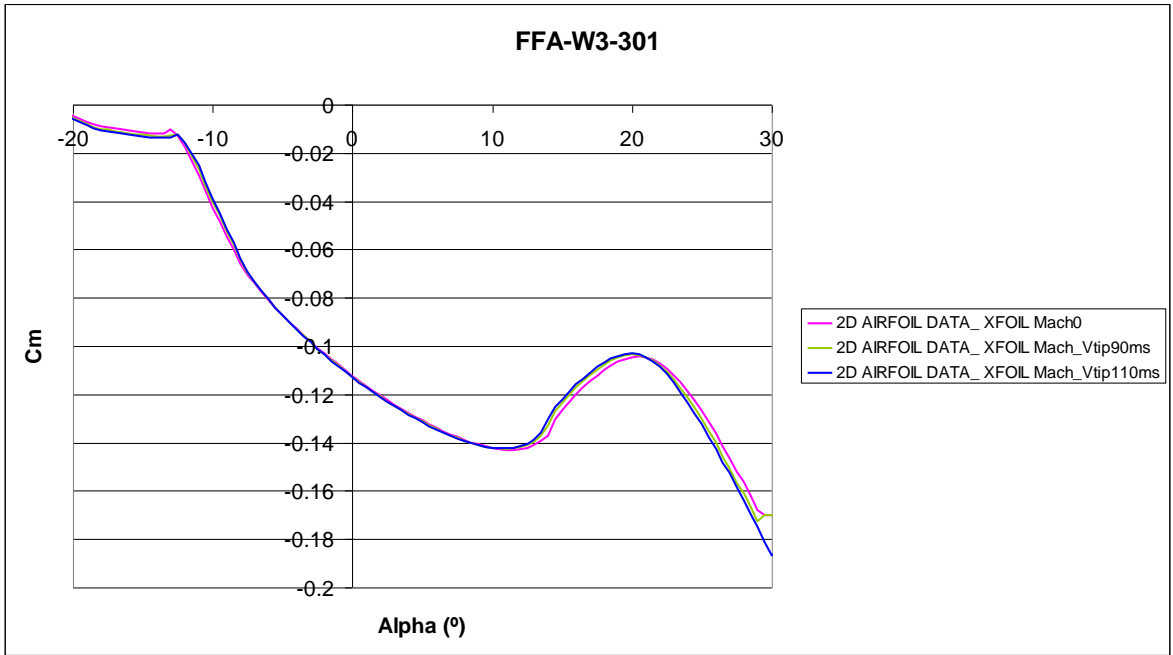


Figure 42: Cm-alpha of FFA-W3-301 airfoil computed with XFOIL for different Mach numbers

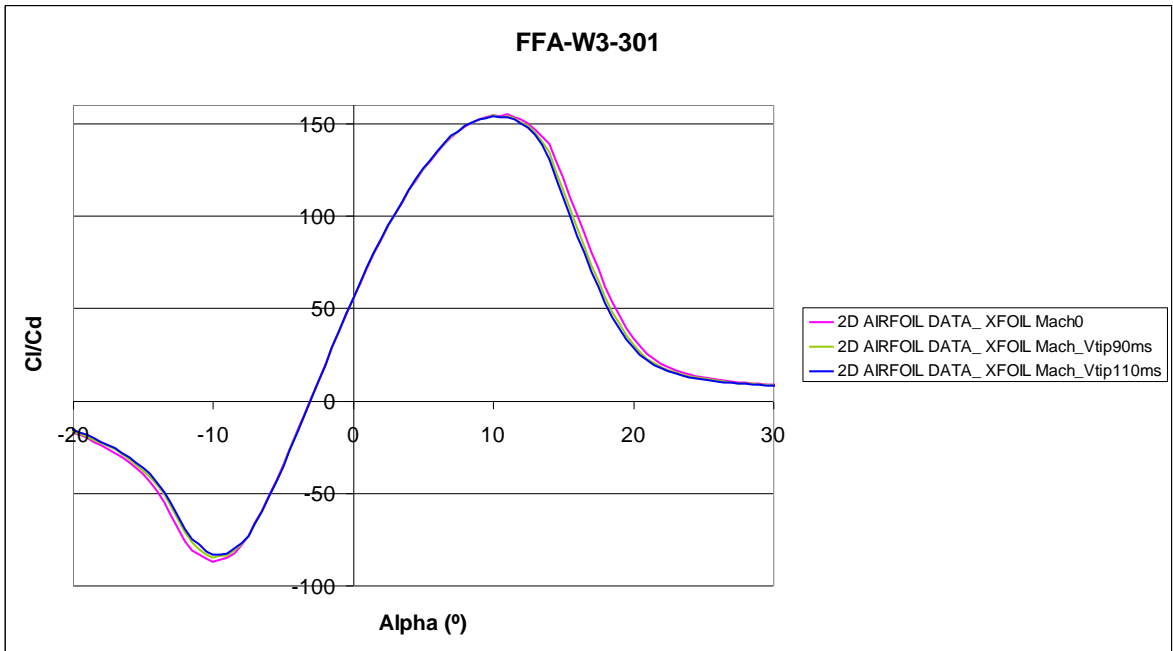


Figure 43: Cl/Cd-alpha of FFA-W3-301 airfoil computed with XFOIL for different Mach numbers

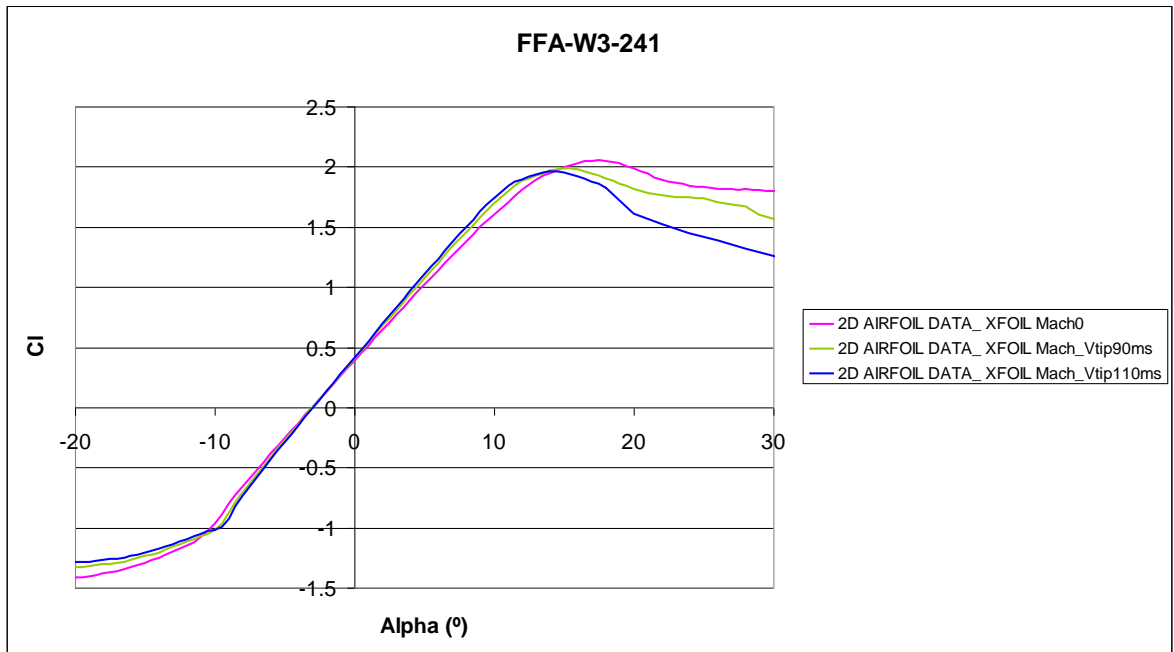


Figure 44: Cl-alpha of FFA-W3-241 airfoil computed with XFOIL for different Mach numbers

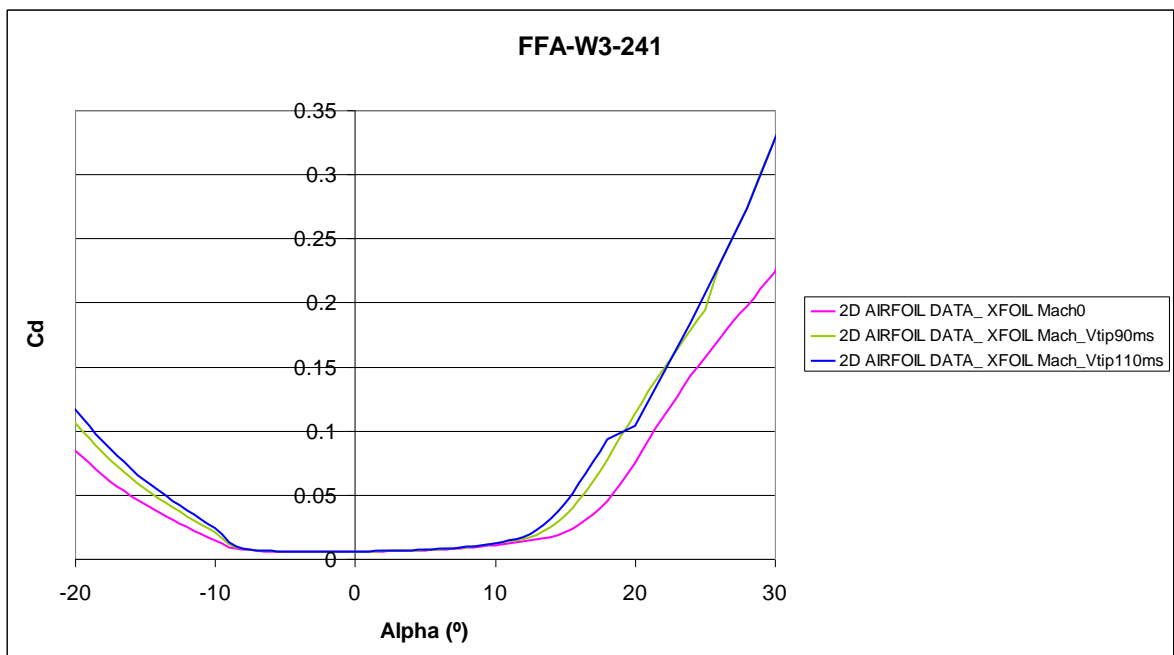


Figure 45: Cd-alpha of FFA-W3-241 airfoil computed with XFOIL for different Mach numbers

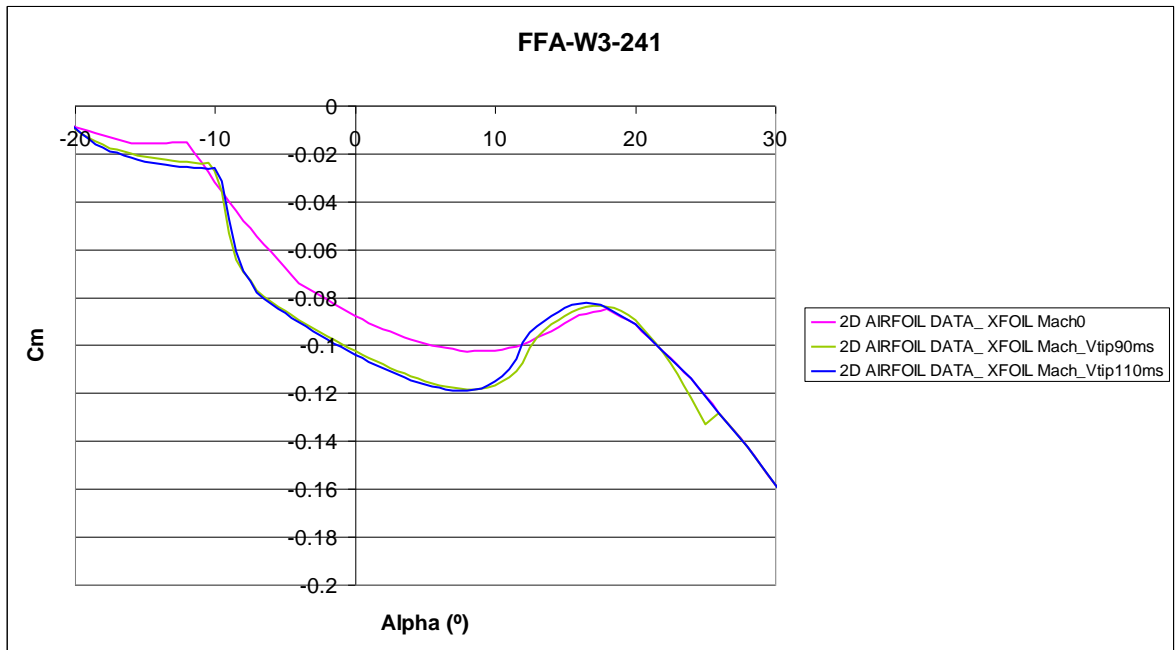


Figure 46: Cm-alpha of FFA-W3-241 airfoil computed with XFOIL for different Mach numbers

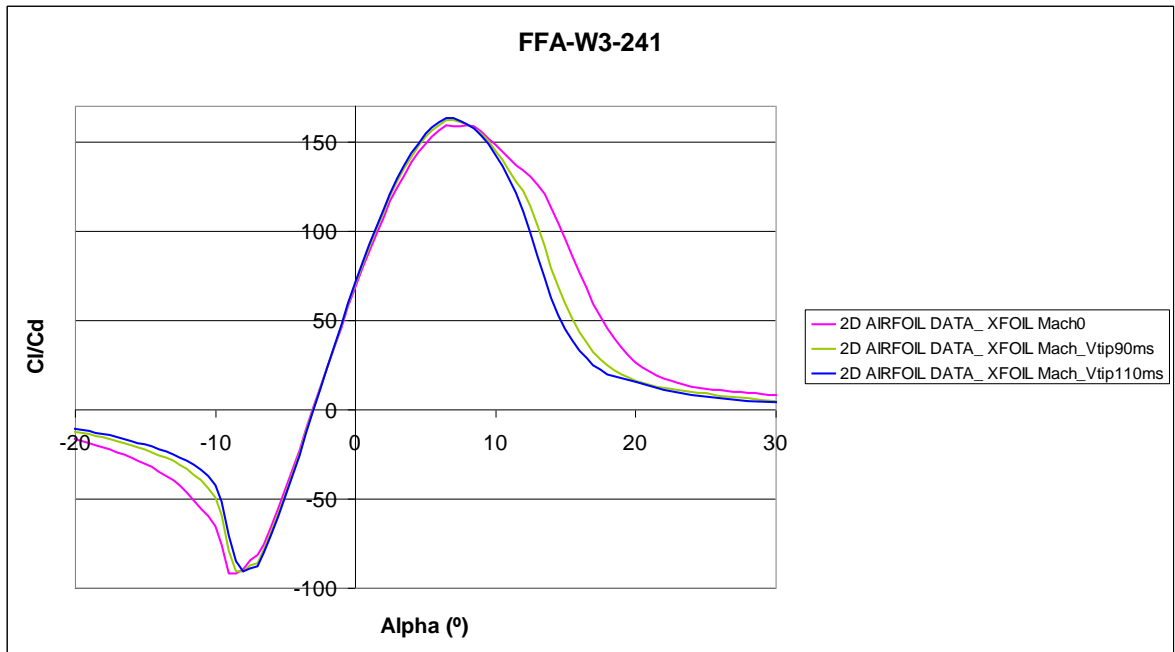


Figure 47: Cl/Cd-alpha of FFA-W3-241 airfoil computed with XFOIL for different Mach numbers

Computed cases

All simulated cases are with constant wind speed with no shear and constant rotor speed. The rotor speed has been taken from the steady power curve given by DTU at the wind turbine's data excel sheet.

Different conditions have been represented for different results:

- Cp, Ct and Cq have been obtained for the average wind speed conditions.
- Power curve and AEP have been calculated at the design λ condition ($\lambda=7.5$; $V_m=10\text{m/s}$; $w=8.03\text{rpm}$; $\text{pitch}=0^\circ$). Those results have been obtained doing a

linealization. This does not give a proper steady power curve, as it starts pitch control before reaching the rated power. However, for comparison purposes the results are enough as long as all steady power curves are calculated in the same way.

- AoA-r, a-r, a'-r, Cp-r, Cl-r, Cd-r, have been calculated at the design λ condition ($\lambda=7.5$: $V_m=10\text{m/s}$; $w=8.03\text{rpm}$; $\text{pitch}=0^\circ$).
- Cp- λ curve has been calculated for $6 < \lambda < 10$ and a fine pitch angle of 0° .

The table below shows the detail of all the simulated cases:

Airfoils	Case description	Outputs
Cener_M_0 Cener_M_0 Cener_M_0	$V_m=10\text{ m/s}$; $w=8.03\text{ rpm}$; $\text{pitch}=0^\circ$ $\lambda_{\text{design}}=7.5$: $V_m=10\text{m/s}$; $w=8.03\text{rpm}$; $\text{pitch}=0^\circ$ Vvariable; $w=9.6$; $\text{pitch}=0^\circ$	Cp, Ct, Cq Spcurve, AEP, AoA-r, a-r, a'-r, Cp-r, Cl-r, Cd-r Cp- λ
Cener_M_Vtip90m/s Cener_M_Vtip90m/s Cener_M_Vtip90m/s	$V_m=10\text{ m/s}$; $w=8.03\text{ rpm}$; $\text{pitch}=0^\circ$ $\lambda_{\text{design}} =7.5$: $V_m=10\text{m/s}$; $w=8.03\text{rpm}$; $\text{pitch}=0^\circ$ Vvariable; $w=9.6$; $\text{pitch}=0^\circ$	Cp, Ct, Cq Spcurve, AEP, AoA-r, a-r, a'-r, Cp-r, Cl-r, Cd-r Cp- λ
Cener_M_Vtip110m/s Cener_M_Vtip110m/s Cener_M_Vtip110m/s	$V_m=10\text{ m/s}$; $w=8.03\text{ rpm}$; $\text{pitch}=0^\circ$ $\lambda_{\text{design}} =7.5$: $V_m=10\text{m/s}$; $w=8.03\text{rpm}$; $\text{pitch}=0^\circ$ Vvariable; $w=9.6$; $\text{pitch}=0^\circ$	Cp, Ct, Cq Spcurve, AEP, AoA-r, a-r, a'-r, Cp-r, Cl-r, Cd-r Cp- λ

Table 8: Set of cases simulated in task 2.1

Results

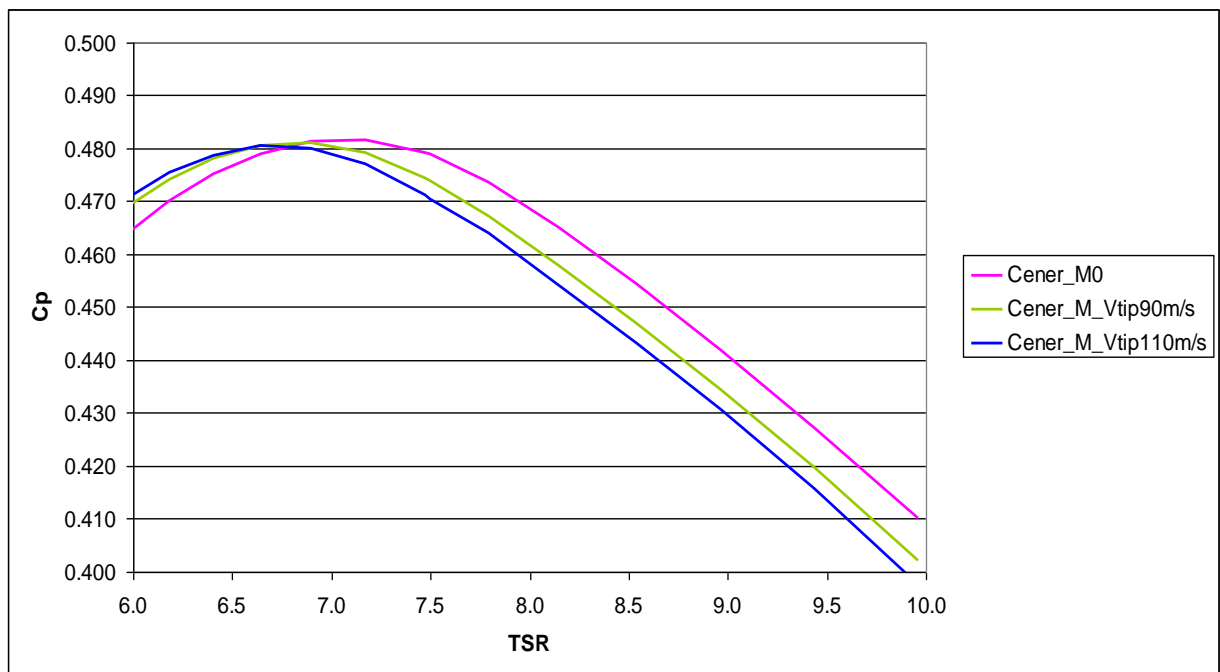


Figure 48: Cp- λ

TSR	Cener_M0	Cener_M_Vtip90m/s	Cener_M_Vtip110m/s
5.976	0.464	0.469	0.471
6.182	0.470	0.474	0.475
6.403	0.475	0.478	0.479
6.640	0.479	0.480	0.480
6.895	0.481	0.481	0.480
7.171	0.482	0.479	0.477
7.470	0.479	0.475	0.471
7.500	0.479	0.474	0.471
7.795	0.474	0.467	0.464
8.149	0.465	0.458	0.454
8.537	0.454	0.447	0.443
8.964	0.442	0.434	0.431
9.436	0.427	0.420	0.416
9.960	0.410	0.402	0.398
max	0.482	0.481	0.480
$\Delta C_{p_{design}}$ incompressible - compressible		-0.501%	-0.954%
$\Delta C_{p_{max}}$ incompressible - compressible		-0.122%	-0.260%

Table 9: C_p - λ values and $\Delta C_{p_{max}}$

In Figure 48: C_p - λ it can be seen that as the compressibility effect is stronger, the $C_{p_{max}}$ moves to lower λ values, and the $C_{p_{max}}$ value decreases.

This means two things:

If a blade is designed for the incompressible airfoil conditions, the really obtained C_p (at compressibility conditions) would be lower than the one expected.

The decrease in C_p between the conventional V_{tip} compressibility situation and the incompressible situation is (in this case) 0.5017%.

The decrease in C_p between the high V_{tip} compressibility situation and the incompressible situation is (in this case) 0.9538%.

That means that the obtained AEP would be lower than the calculated one, if compressibility effects have not been taken into account in the calculation.

However, if compressibility effects are considered, those losses in C_p would be lower because a different design λ value would be taken, and at that λ the C_p would be higher.

The decrease in C_p between designing at conventional V_{tip} compressibility λ and designing at the incompressible λ is (in this case) 0.1219%.

The decrease in C_p between designing at high V_{tip} compressibility λ and designing at the incompressible λ is (in this case) 0.2599%.

From the incompressible case to the compressible case with conventional tip velocity, $\Delta\lambda(C_{p_{max}}) = -0.2758$. From the incompressible case to compressible case with high tip velocity, $\Delta\lambda(C_{p_{max}}) = -0.5312$.

So, design λ values would decrease 0.27-0.53 when considering compressibility to have the maximum AEP.

Anyway, it has been said before that as the compressibility effect is stronger, the $C_{p_{max}}$ moves to lower λ values, and the $C_{p_{max}}$ value decreases. So, C_p - λ curves of the different compressibility situations match in a point (see figure 18). From that point to higher λ values, the relation between the C_p - λ curves would be the opposite than from that point to lower λ values.

The conclusions taken before, have been taken considering λ values around the optimum for incompressible conditions, but if λ values are lower than the optimum at incompressible conditions, it could happen that the obtained C_p at incompressible λ conditions would be higher than the expected one.

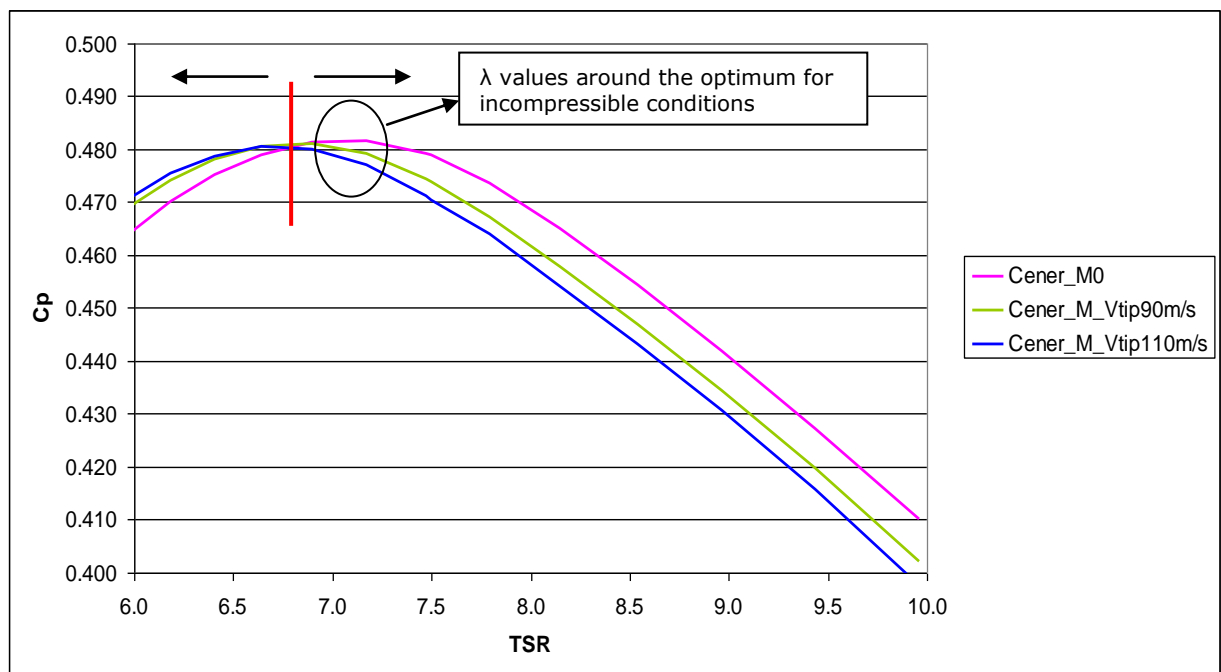


Figure 49: C_p - λ in different regions

Power Production:

All power production curves and AEP have been calculated for the incompressible λ conditions.

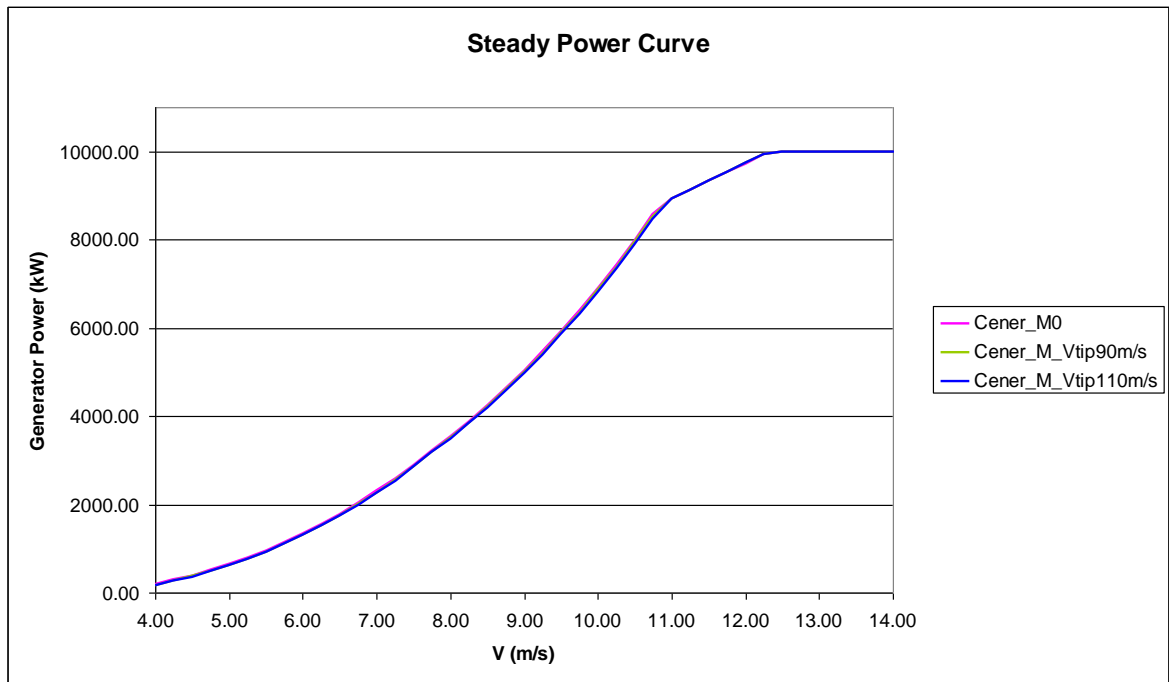


Figure 50: Steady power curve

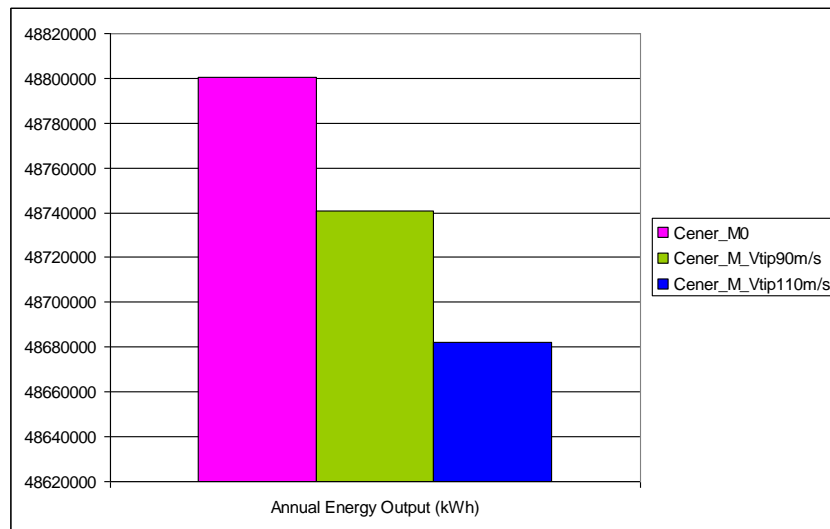


Figure 51: Annual Energy Production

	AEP (kWh)	Δ AEP incompressible - compressible	Δ AEP compressible at conventional Vtip - compressible at high Vtip
Cener_M0	48800550		
Cener_M_Vtip90m/s	48740699	-0.123%	
Cener_M_Vtip110m/s	48682187	-0.242%	-0.1203%

Table 10: AEP results and Δ AEP

As shown in the previous figures and Table 10, as compressibility effect increases the produced annual energy decreases if the blade is designed for incompressible airfoil conditions.

Cp, Ct, Cp/Ct and Cq:

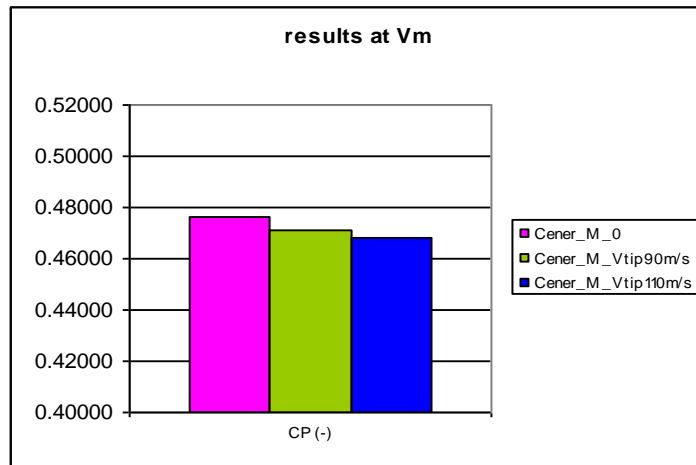


Figure 52: Cp at Vm

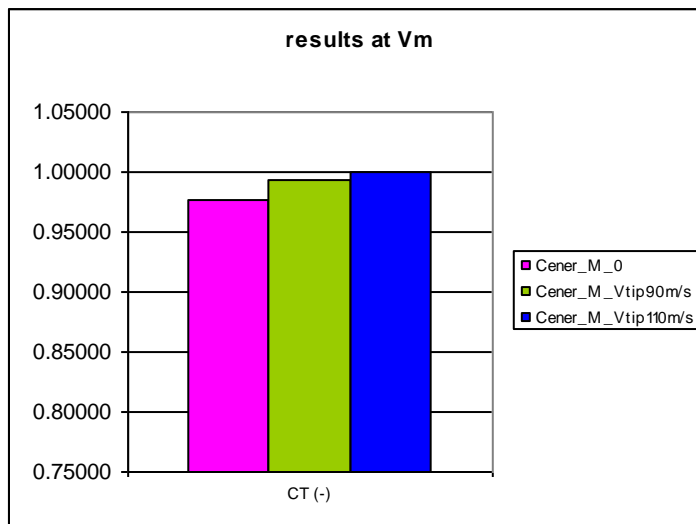


Figure 53: Ct at Vm

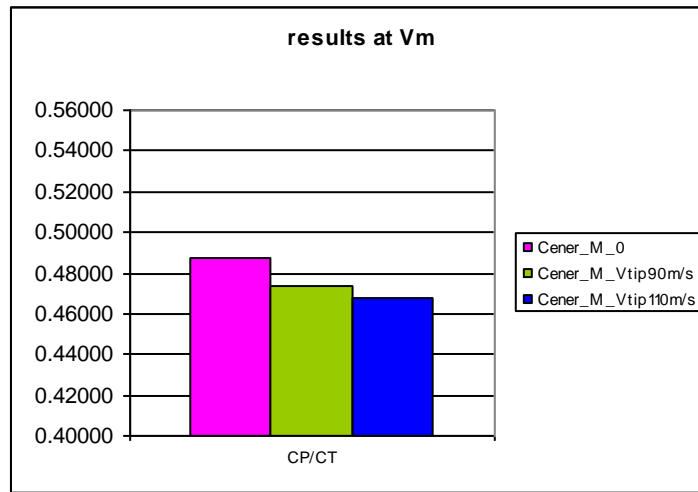


Figure 54: Cp/Ct at Vm

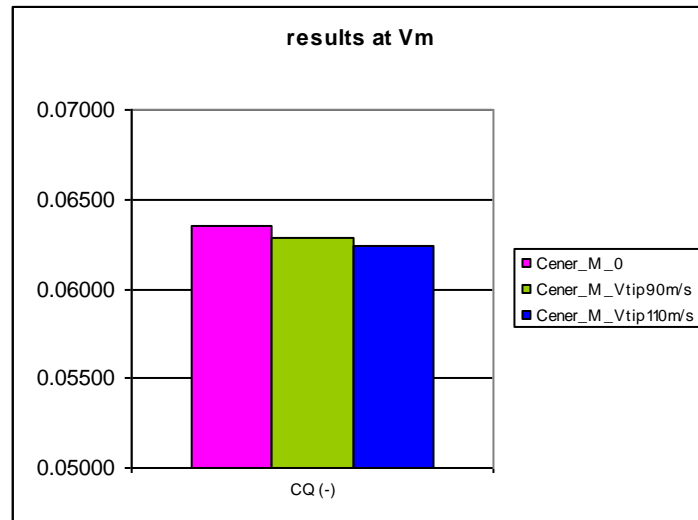


Figure 55: Cq at Vm

		Cp (-)	Ct (-)	Cp/Ct	Cq (-)
Cener_M_0	Vm	0.476	0.97600	0.48770	0.06350
Cener_M_Vtip90m/s	Vm	0.471	0.99400	0.47384	0.06280
Cener_M_Vtip110m/s	Vm	0.468	1.00000	0.46800	0.06240
Δ incompressible - compressible		-1.050%	1.844%	-2.842%	-1.102%
Δ compressible at conventional Vtip - compressible at high Vtip		-0.637%	0.604%	-1.233%	-0.637%

Table 11: Cp values and Δ Cp at Vm

As shown in previous figures and table, as compressibility effect is stronger Cp decreases, Ct increases, Cp/Ct decreases and Cq decreases.

This is consistent with Cp-λ, Spcurve and AEP results seen before.

The decrease in C_p means that not considering compressibility effects, the power production is overestimated, while the increase in C_t means that the loads are underestimated: situation against the security of the design.

$AoA-r$, $a-r$, $a'-r$, C_p-r , C_l-r , C_d-r :

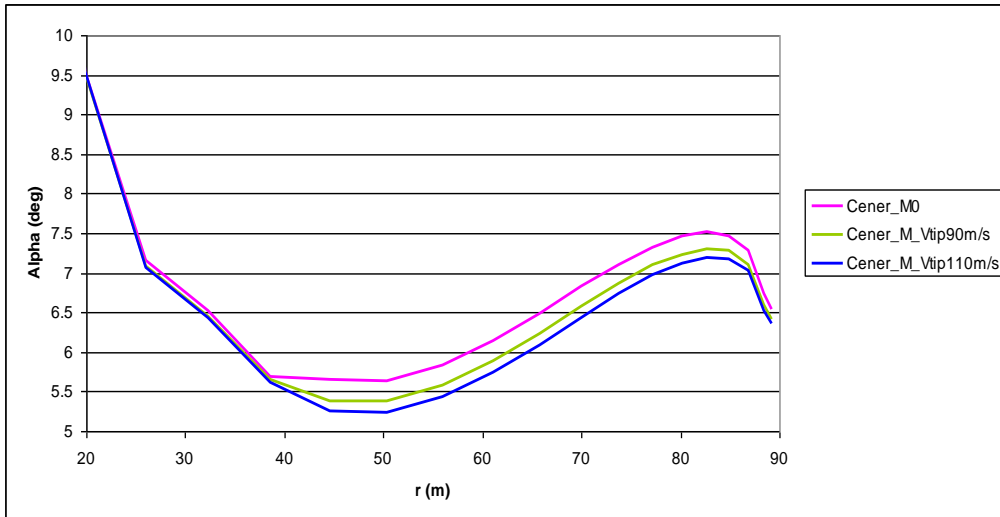


Figure 56: Alpha-r at λ_{opt} condition

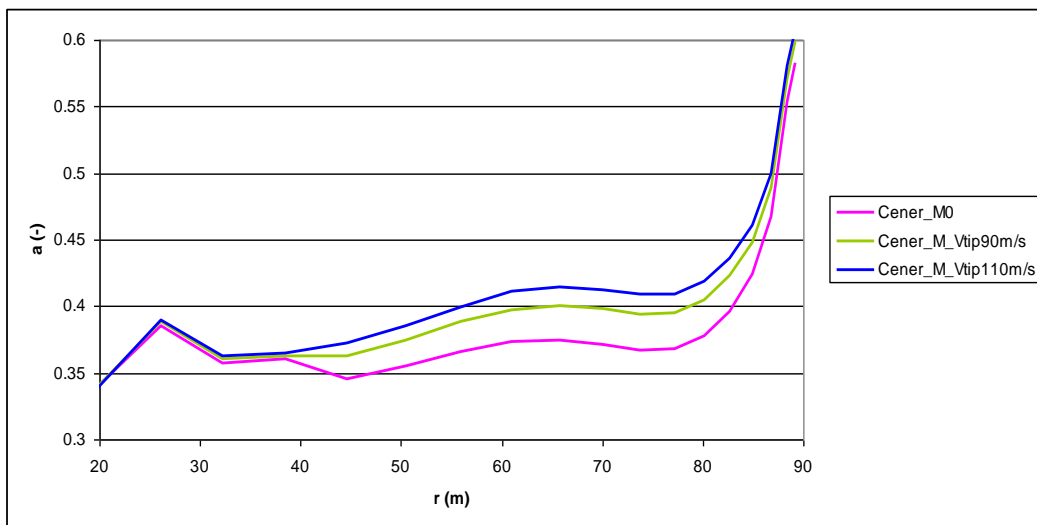


Figure 57: a-r at λ_{opt} condition

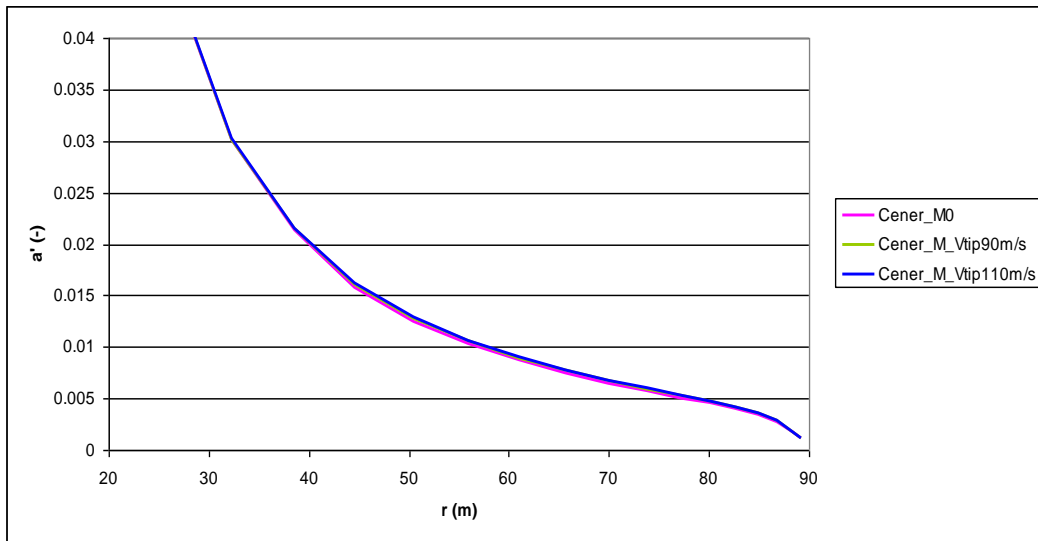


Figure 58: $a'-r$ at λ_{opt} condition

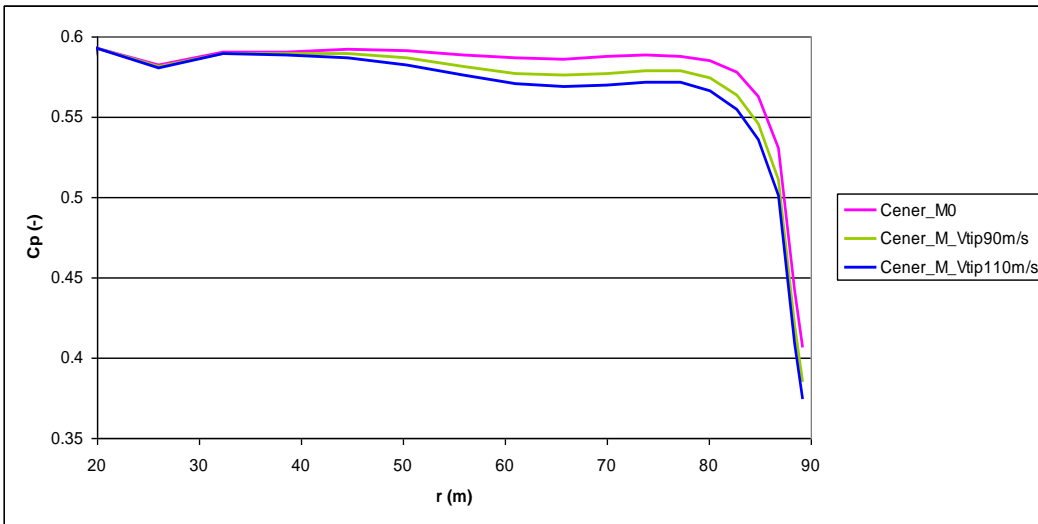


Figure 59: C_p-r at λ_{opt} condition

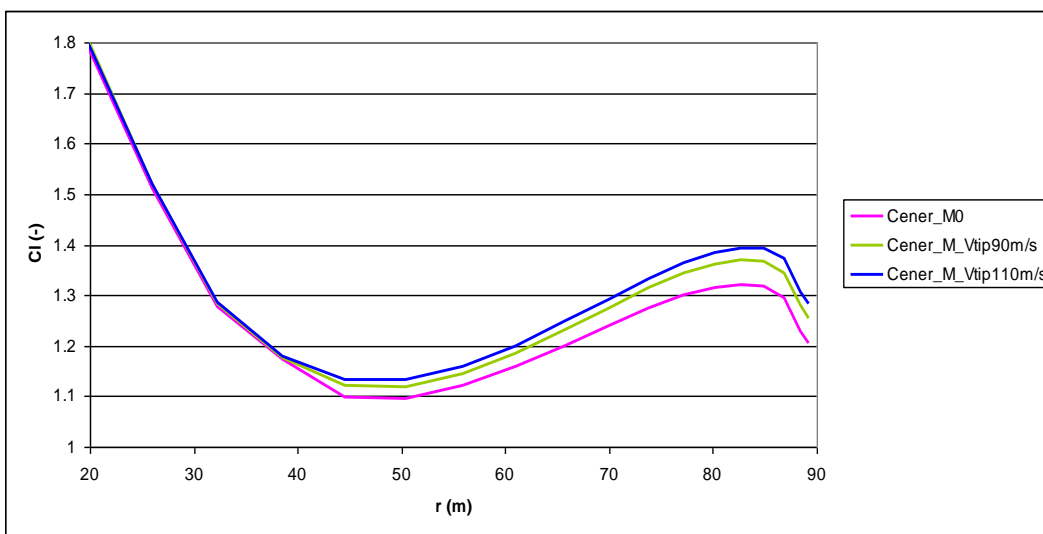


Figure 60: C_l-r at λ_{opt} condition

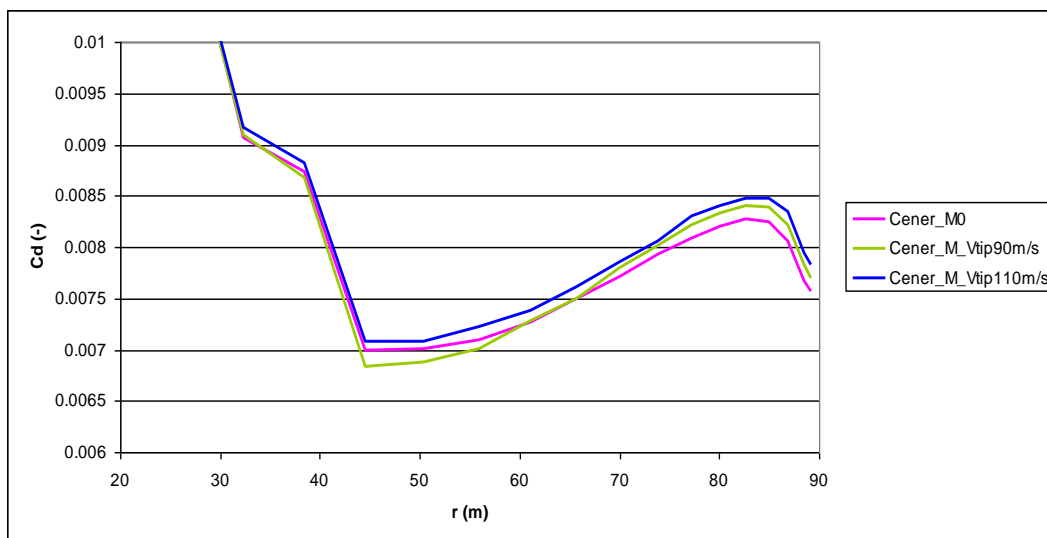


Figure 61: Cd-r at λ_{opt} condition

For the same λ_{design} condition, when compressibility effect is stronger axial induction is higher, so AoA decreases. However, as airfoil polars have changed and for higher mach numbers Cl-AoA and Cd-AoA curves are higher at linear region (mainly at tip, see figures 13 and 14), Cl and Cd values are also higher. Anyway, as axial induction is stronger (and very high) Cp-r is lower, what is consistent with the results of the power curve and AEP seen before.

Looking to Figure 59, the strong effect of compressibility in Cp around the blade can be evaluated.

An important point is that the effect is noticeable from the 45% of the radius. It is also important to know that from 68%R to 95%R, the decrease seen in Cp is almost constant and strong: the decrease in Cp for a conventional Vtip compressibility condition is 1.92%, and for a high Vtip compressibility condition is 3.26%.

Conclusions:

- If a blade is designed for the incompressible airfoil conditions, the really obtained Cp (at compressibility conditions) would be lower than the one expected. That means that the obtained AEP would be lower than the calculated one, but would be more realistic.
- If compressibility effects are considered, those loses in Cp would be lower because a different design λ value would be taken, and at that λ the Cp would be higher.
- Design λ values would decrease 0.27-0.53 when considering compressibility to have the maximum AEP.
- As compressibility effect is stronger Cp decreases and Ct increases. The decrease in Cp means that not considering compressibility effects, the power production is overestimated, while the increase in Ct means that the loads are underestimated: situation against the security of the design.
- The compressibility effect is noticeable from the 45% of the radius. Looking to Cp along the radius, from 68%R to 95%R, the decrease seen in Cp is almost constant and strong: the decrease in Cp for a conventional Vtip compressibility condition is 1.92%, and for a high Vtip compressibility condition is 3.26%.

ECN: NEW AIRFOILS FOR HIGH EFFICIENCY AND LOAD REDUCTION

Francesco Grasso, Ozlem Ceyhan

Introduction

A way to reduce the weight of the blades for very large offshore wind turbines, is the use of specially tailored new airfoil families.

The scope of this preliminary study is to investigate the potentialities of new airfoils adoption in decreasing the loads and the weight of the blade, while keeping high aerodynamic performances.

Requirements for new airfoils

Specific studies have been performed by ECN [10,11,12,13], focused on the design of new airfoils and the definition of design requirements for geometries suitable for large, lightweight wind turbine rotors.

A general list of requirements is listed below:

- Aerodynamics
 - High aerodynamic efficiency (L/D)
 - Good performance in off-design conditions
 - Insensitivity to the roughness
 - Good stall characteristics
 - Margin between design condition and stall (gust robustness)
- Structure
 - High structural strength
- Geometry
 - Sufficient internal space for the spar
 - Compatibility with the other airfoils along the blade

From the aerodynamic point of view the most important parameter for the tip region is the aerodynamic efficiency (L/D). In order to obtain good turbine performance, the aerodynamic efficiency should be as high as possible, but, at the same time, other considerations should be taken into account.

One consideration is related with the stall behavior and the C_{lmax} . Some of the existing airfoils for wind turbines have also a high value of C_{lmax} and a relative high value for the design C_l ; this means that, for a certain load, a smaller chord is necessary. This reduces loads under parked conditions at high wind speeds. A lower chord in the outboard sections also reduces weight. In addition to this, a high C_l value (and lower associated chord c) in the outboard sections reduces the amplitude of load fluctuations resulting from wind gusts. Hence a high C_l is desirable to reduce fatigue and parking loads and can save weight. On the other hand, the stall can be abrupt and undesirable vibrations can be induced on the blade. So, it is important that the transition and the separation move gradually when the angle of attack increases. Another important consideration is related with the sensitivity of the airfoil to the roughness. An airfoil with a large laminar flow extension will be very efficient in “clean” conditions, but very bad in case of “dirty” conditions.

Another problem that should be taken into account in developing airfoils for wind turbines is connected with gusts. Because of gusts, the local angle of attack for the single airfoil can suddenly change and be in pre-stall or stall zone. So, it is important to keep good off-design performances and try to have an angle of attack range between the design angle of attack and the one for which, noticeable separation occurs on the airfoil.

Effects of new airfoils for the development of very large offshore wind turbines

In this preliminary study, the aerodynamic characteristics of the airfoils (named ECN-G1, formerly GWA-A1) presented in the above mentioned references have been used to simulate new airfoils.

The analysis of the wind turbine performance has been calculated considering the blade as rigid body operating in normal conditions. The simulations have been performed by using the ECN tool BOT [14], that is based on BEM theory. One of the inputs consists in the aerodynamic characteristics of the airfoils. The RWT is equipped with FFA-W3-xxx airfoils. In order to have fair comparisons with the performance obtained with the new airfoils, the original datasets provided in INN WIND.EU regarding the airfoil properties have been replaced by the ones obtained by using the ECN panel code RFOIL [15].

As mentioned at the beginning of the paragraph, the RWT has been modified to include the ECN-G1 airfoils. Chord and twist distributions have been optimized (based on the new airfoils) to maximize the Annual Energy Production (AEP) and the pitch angles have been adapted. However, the other parameters of the blade like the blade radius, the design tip speed ratio (TSR) and the other operating parameters have been kept unchanged, so the effects due to the introduction of new airfoils can be investigated.

The following figures show the comparison between the geometries. The main difference consists in a reduction in chord, so in the plan-form area. This can be beneficial in case of parking conditions; a reduction of 2.6% should be expected.

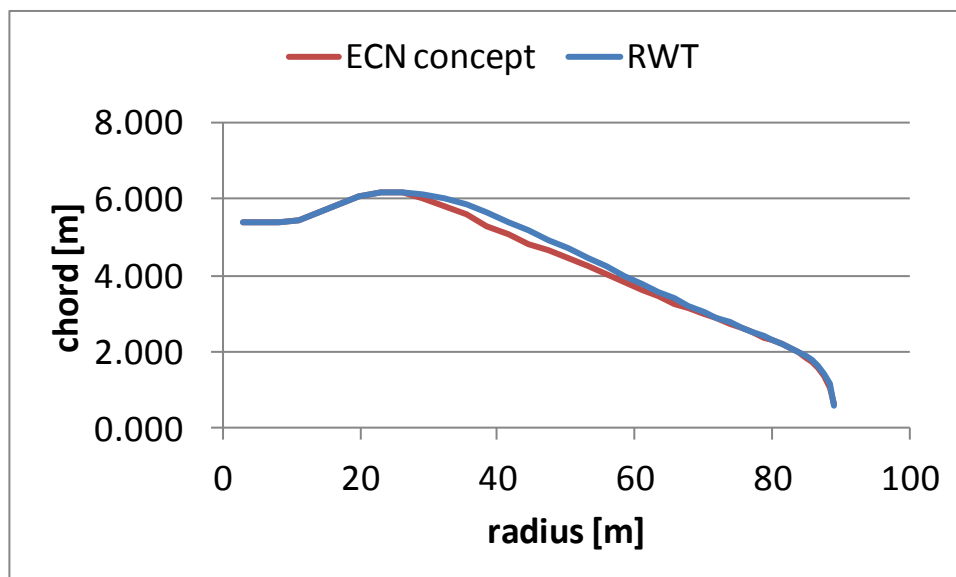


Figure 62: Chord distribution of the RWT and ECN concept.

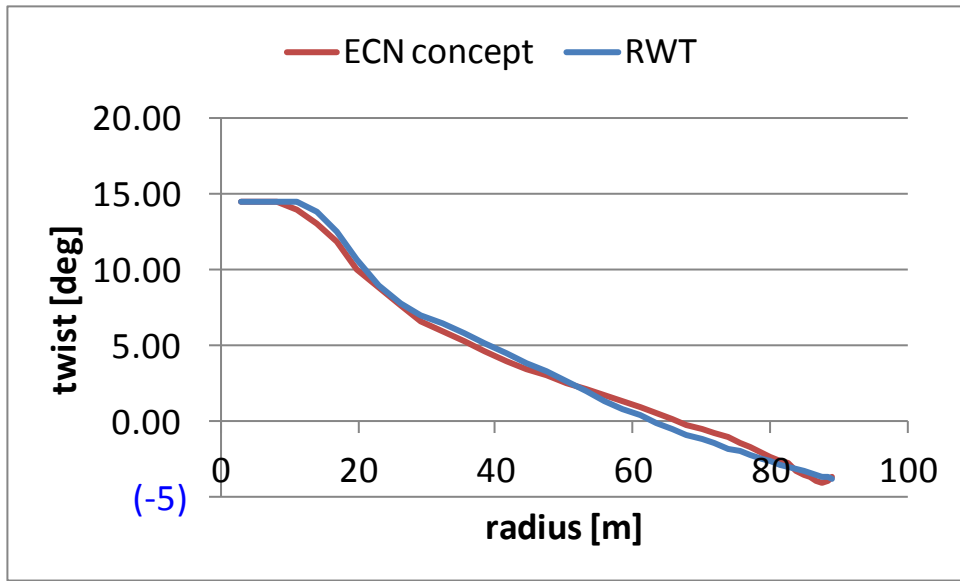


Figure 63: Twist distribution of the RWT and ECN concept

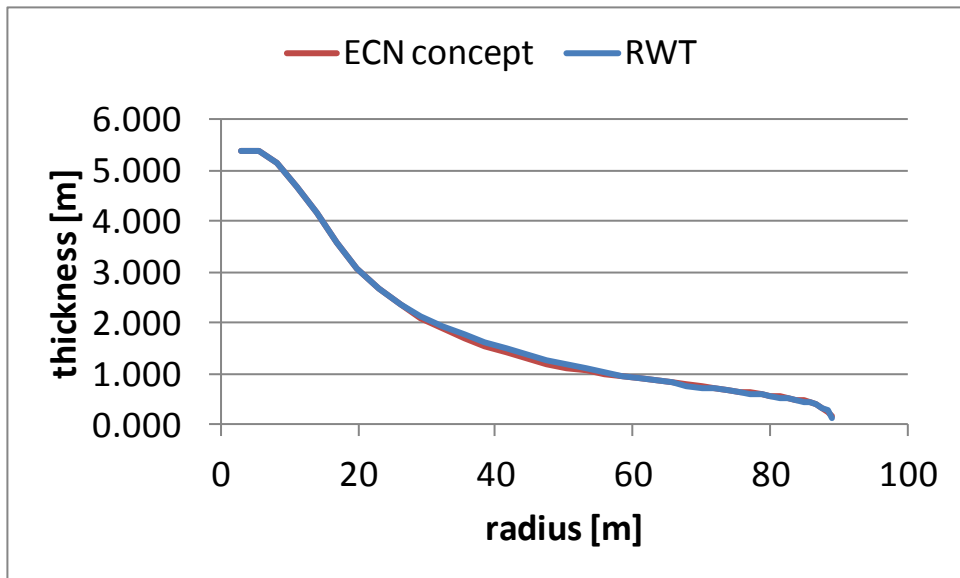


Figure 64: Thickness distribution of the RWT and ECN concept

	RWT	ECN	ECN mod
Yield: GWh/yr	53.41	53.45	53.41
P_{rated} : kW	10000	10000	10000
U_{rated} : m/s	12.00	12.00	12.00
C_{Pmax} : (mech)	0.4980	0.4987	0.4987
λ_0 :	7.500	7.500	7.500
Q_{start} : kNm	89.113	93.141	93.141

Table 12: Overall blade performance

Table 12 shows the overall performance of the blades.

As it can be seen, the AEP for the new blade is slightly larger than the reference value, as well as the maximum mechanical power coefficient (C_{pmax}). In the same table, a modified version of the new blade is proposed, where the pitch angle at rated wind speed has been modified in order to have the same AEP as the reference geometry but a reduction in loads.

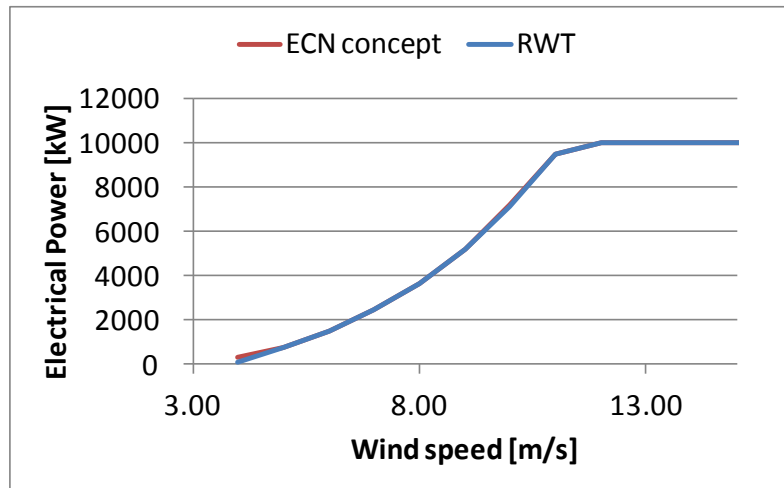


Figure 65: Power curve comparison.

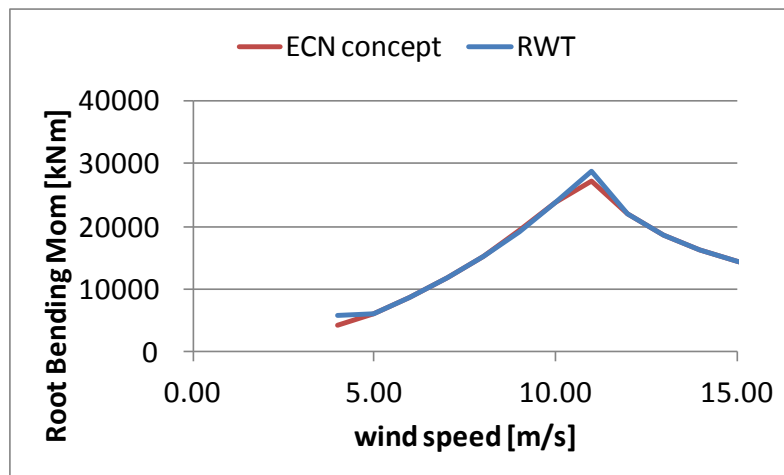


Figure 66: Root bending moment comparison.

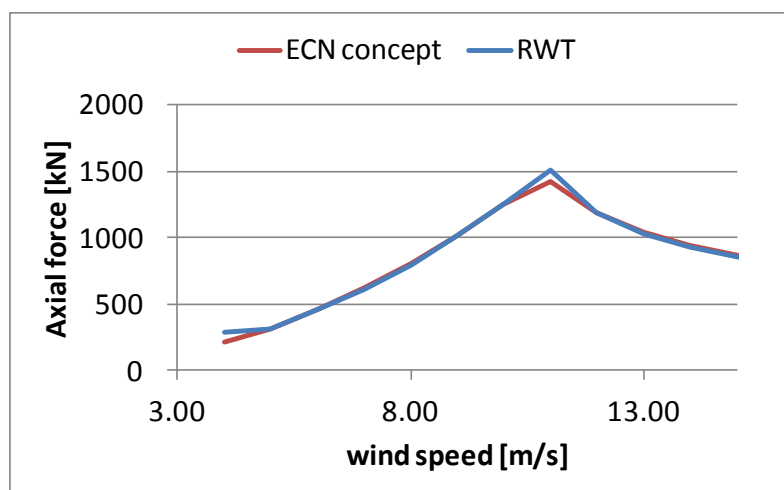


Figure 67: Axial force comparison.

Figure 65-Figure 67 show the performance of the RWT and the modification in terms of axial force and root bending moment. A reduction of 5.4% for the axial force and 5.6% for the root bending moment has been obtained that can lead to a reduction of the cost due to the materials/weight of the blade, the tower but also it can be beneficial to extend the life of the bearings and other components. This means a reduction in maintenance costs.

Conclusions

A conceptual study has been performed, focused on the impact of new advanced airfoils on the performance of very large offshore wind turbines. The preliminary results showed that:

- New airfoil families can contribute to reduce the cost of energy (CoE) of very large wind turbines. In particular, airfoils with high lift performance, beside high aerodynamic efficiency, can be beneficial to reduce the blade surface (slender blade). As consequence, the loads in parked conditions can be reduced. Together with it, the root bending moment and the axial force can visibly be reduced, while keeping the same annual energy production (AEP). Alternatively, an increase in AEP can be achieved with the same loads as the reference geometry.
- Beside high lift and high efficiency, other parameters should be considered to evaluate the performance of an airfoil. In terms of weight, high lift airfoils can lead to lighter weight blades. However, the structural design was not included in the present study. In general, beside the aerodynamic characteristics of the airfoils, also the structural properties should be considered during the design
- In performing the design of new airfoils, the geometrical compatibility of the shapes is important for manufacturing and to avoid not uniform local loads along the blade. As consequence, the design of families of airfoils is needed.

ECN: PARAMETRICAL CONCEPT STUDY FOR LOWER POWER DENSITY ROTORS

Francesco Grasso, Ozlem Ceyhan

Introduction and motivation

Growing rotor sizes of offshore wind turbines changes the rotor design principles. Today's largest rotor is more than 150m diameter and the capacities are around 7-8MW. In INN WIND.EU project, 10 MW reference turbine is designed in order to compare innovative rotor concepts with it. This rotor is one of the possible concepts that can be used for future 10MW turbines. It has 179m diameter and that means the power density is 400W/m² for a tip speed of around 90m/s. However, there is a tendency to go for lower power densities with larger blade length in the industry in recent years. Therefore, in this study, it is aimed not to skip this aspect as one of the possible future trend for conventional wind turbine concepts while the innovations are being compared with the reference turbine.

Parameters

In this study, very shortly, the rotor radius is increased to 103m to reach the power density of 300W/m². When the rotor radius increased, the parameters like tip speed, solidity, rpm and tip speed ratio needs to be adjusted. Since those parameters influence each other, a parametrical study is performed. The rotor concepts that are covered are categorized in 3 groups: alternative 1, 2 and 3 which are shown in Table 13. For alternative 1, tip speed, solidity and tip speed ratio are kept constant so rpm is reduced. For alternative 2, rpm is increased to be the same as the reference, and solidity has been decreased proportionally and then the tip speed is increased as well as tip speed ratio. For alternative 3, tip speed ratio is increased to 9.5 to simulate the tendency of designing high tip speed ratio rotors with high tip speeds. These concepts will be investigated further but in a rather limited manner since they are not innovative.

	Reference	Alter1	Alter2	Alter3
Total capacity	10000000	10000000	10000000	10000000
Tip speed	89.64	89.64	103.55	113.54
Lambda	7.50	7.50	8.66	9.50
rpm	9.60	8.31	9.60	10.53
radius	89.166	103	103	103
Power density	400.36	300.04	300.04	300.04

Table 13: Alternative rotor concepts and the design parameters

Results

For alternative 1, the chord length is proportionally increased with the increase of radius to keep the solidity the same as reference rotor blade. In addition to alternative 1, the solidity is decreased by keeping the twist angles the same. For the low solidity alternative 1, the chord distribution is calculated by curve fitting the chord length between alternative 1 and the reference blade starting from the root chord of reference rotor. In order to reduce the loads further, pitch angles for operation is increased such that the blade root bending moment of this rotor is equal to the one of the reference blade (the local angles of attack are reduced). This rotor is called as "alternative 1 ls (low solidity)" and it is compared also with alternative 1 with peak shaving strategy. The chord length of

alternative 1 ls is compared with chord length of alternative 1, 2 and 3 and the reference blade in Figure 68.

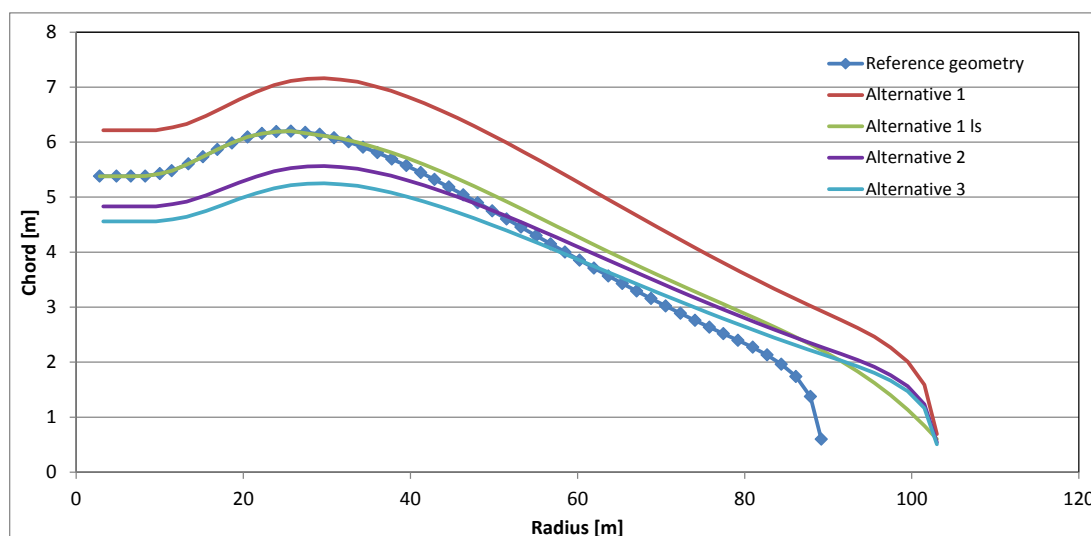


Figure 68: Chord distributions of alternatives are compared with each other&reference blade.

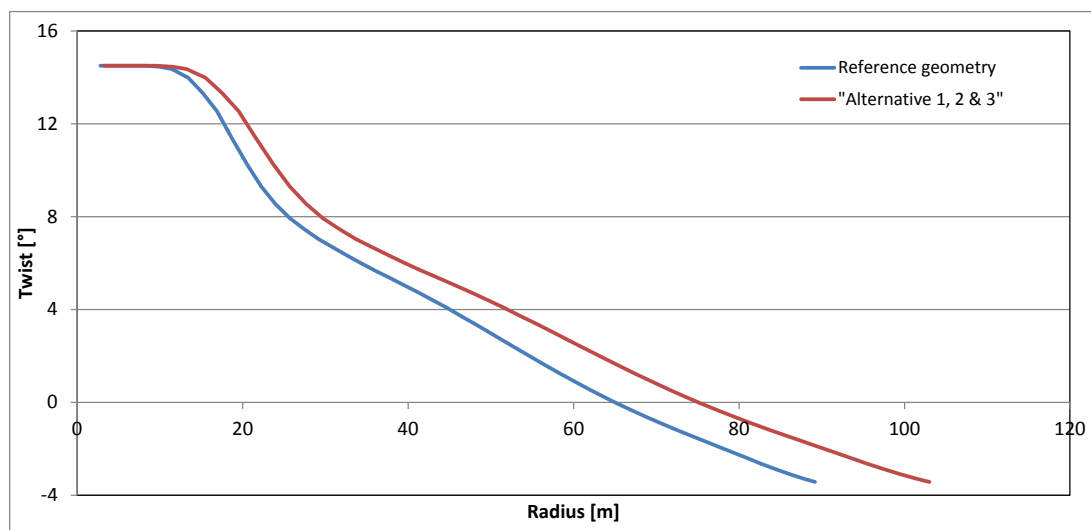


Figure 69: Twist distributions of alternatives are compared with the reference blade.

As a result of increase in blade length, rated wind speed is decreased from 11m/s to 10m/s but the loads before the rated wind speed are increased. However, especially the parked loads&loads due to gusts in alternative 2 and 3 are expected to be lower than the rest of the concepts due to the significant reduction in their chord lengths. But it is necessary to perform detailed load simulations to prove this. Another way of reducing the loads is to apply the peak shaving strategy which is investigated in “alternative 1 peak shaving”. Alternative 1, 2 and 3 give almost the same axial loads as shown in Figure 70. However, “alternative 1 ls” and “alternative 1 peak shaving” show significant reduction in axial loads, even lower than the reference rotor. Similarly for the blade root bending moments of alternative 1, 2 and 3 are increased due to the blade length as shown in Figure 71. In alternative 1 peak shaving, the pitch angles are modified slightly in order to reduce the maximum blade root bending moment to the one of the reference rotor. The difference between those concepts is also visible in c_t comparisons in Figure 72. c_t of alternative 1, 2 and 3 are reduced above rated wind speed of 10m/s compared to the

reference turbine. Moreover, “alternative 1 ls” shows a significant low c_t operation compared to the rest of the concepts where alternative 1 peak shaving is still lower than the other rotors except alternative 1 ls. This parameter is especially important for the farm operation of the different rotor concepts. Lower C_t operation implies lower wake losses of the turbine which means more power production for the second/third row of the turbines. However, this needs to be investigated further.

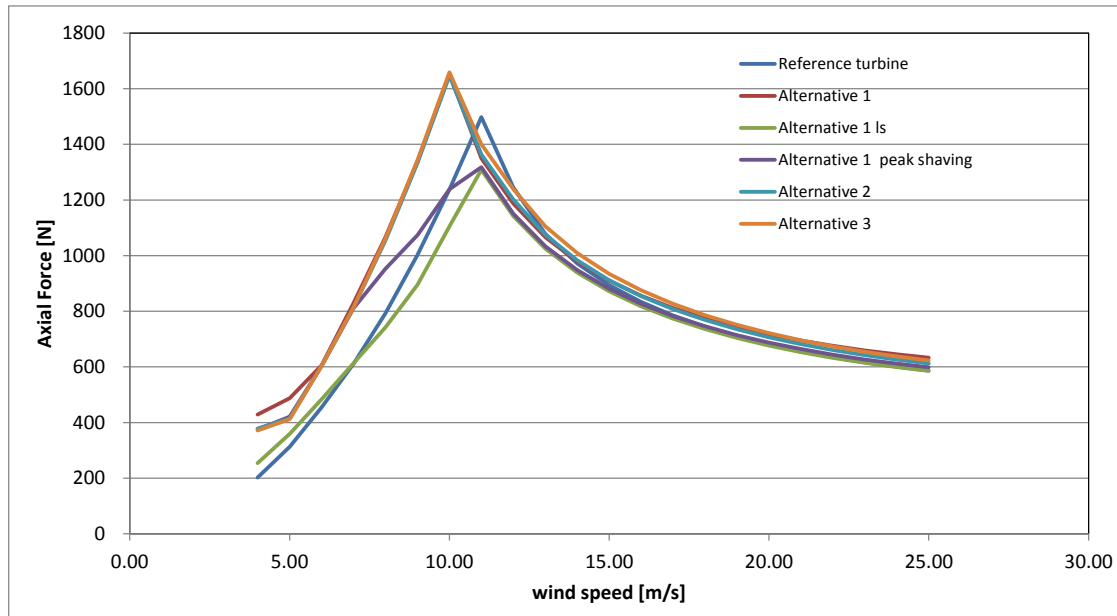


Figure 70: Axial force comparison of alternatives.

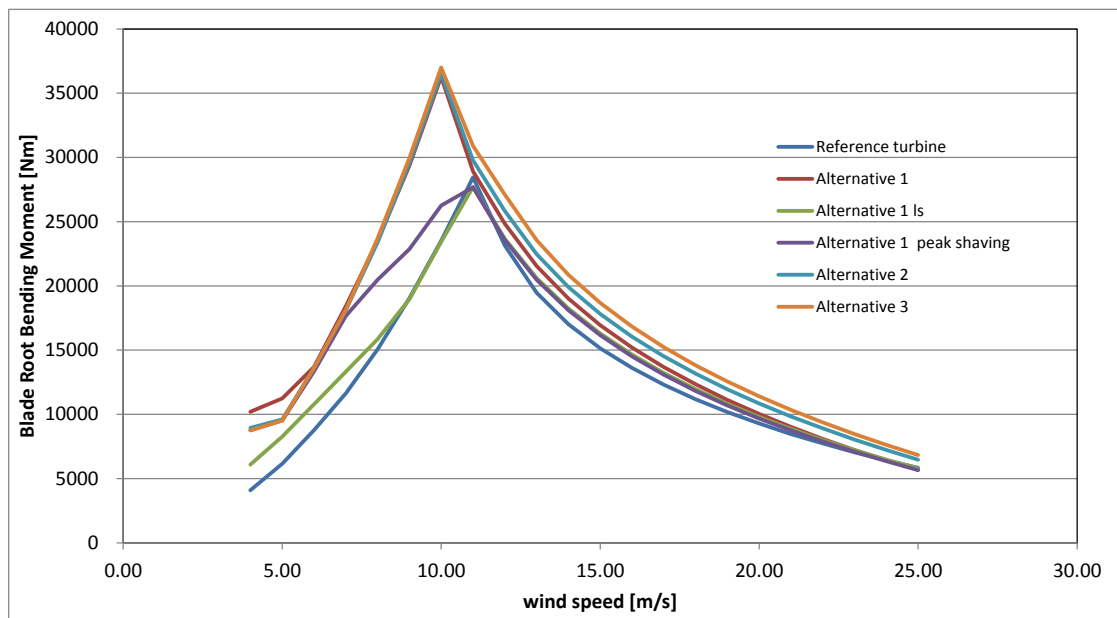


Figure 71: Blade root bending moment comparison of alternatives.

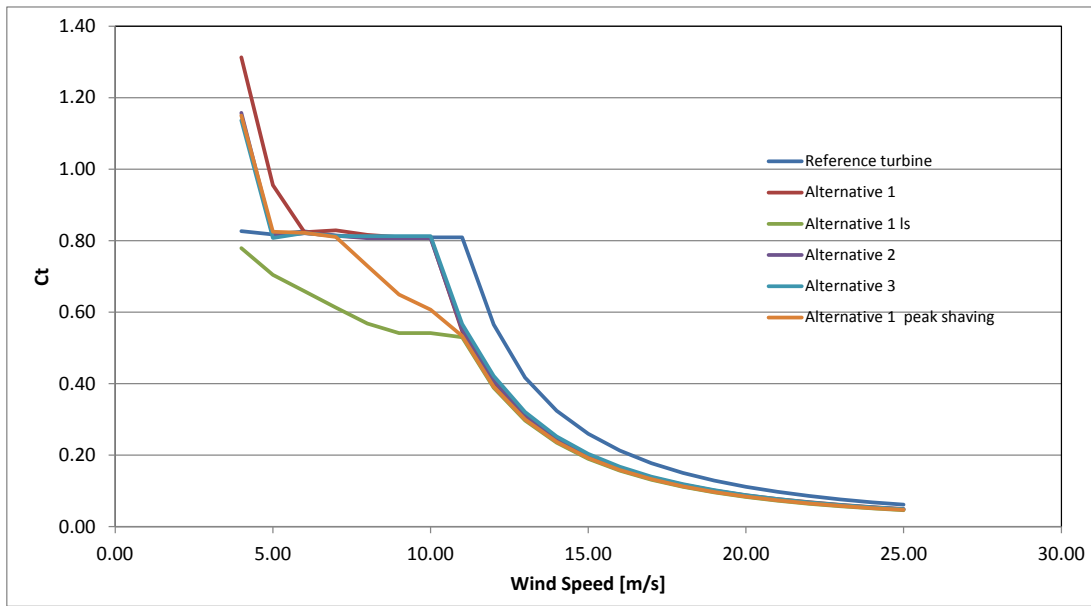


Figure 72: Ct comparison of alternatives

Power productions from all those concepts are compared in Figure 73 in terms of annual yield. Annual yield is increased due to the increase in blade length for more than 9% even if the loads are reduced by using a more slender blade or a peak shaving strategy. Although “alternative 1 peak shaving” seems to be more advantageous in terms of low axial load and high power production, these results require more investigation in terms of dynamic load cases in turbulent environment, gusts, etc. Moreover, since a peak shaving strategy can be applied to alternatives 2&3 where the blades are significantly more slender than the other concepts, it is crucial to compare the concepts in terms of the design driving loads and operational loads during the lifetime of the wind turbine and their effectiveness in farm operation in order to find the most optimum (conventional) concept for the future large wind turbines.

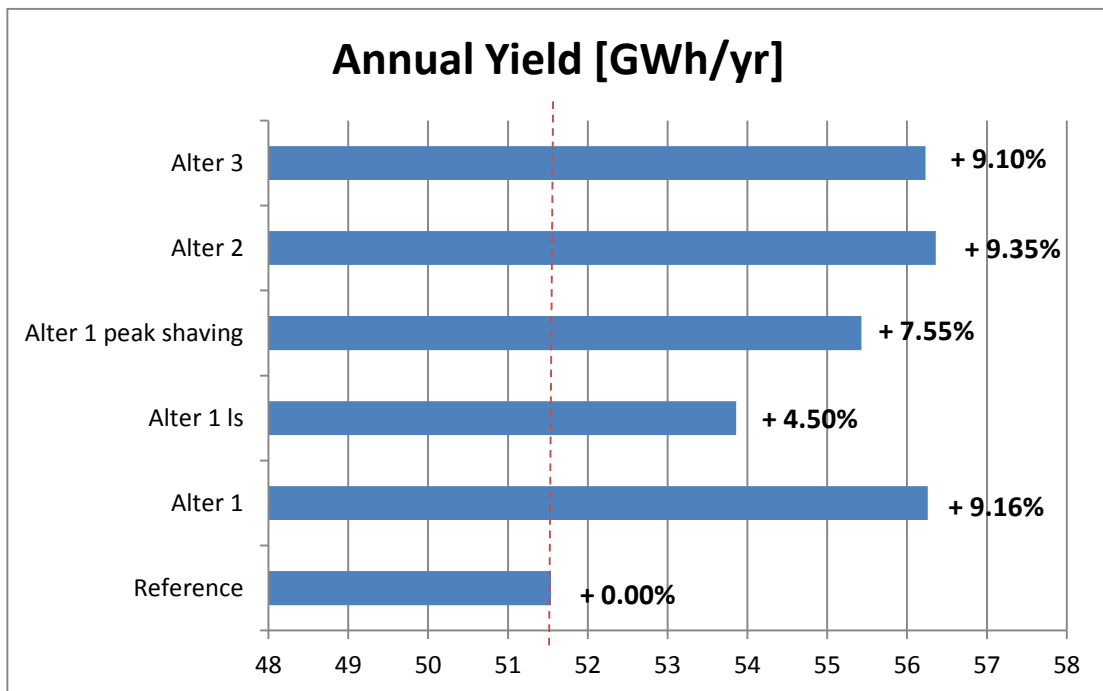


Figure 73: Annual yield comparisons of different concepts

Conclusions

Lower power density rotors have been investigated for this study parametrically in order to include the evaluation of other conventional concepts for future 10MW wind turbines. Two main conclusions out of this study are

- Lower power density with low solidity blades have a significant potential for load and weight reduction of the rotors.
- Lower loads mean lower annual yield and it needs to be justified how much load reduction and how much power reduction is still beneficial for the reduction of the cost of energy.

It is also crucial to consider the farm operation of the wind turbines with the new concepts in order have a better understanding of the benefits of those concepts since future large wind turbines are mainly going to be built in off shore wind farms.

DTU WIND: TWO-BLADED ROTOR CONFIGURATION

Leonardo Bergami, Helge Aagaard Madsen, Flemming Rasmussen, Frederik Zahle

Introduction

The aim of this contribution is to propose a lighter rotor alternative for the DTU 10 MW reference Wind Turbine [16] by exploring an innovative two-bladed configuration. The preliminary investigation describes the benefit and addresses some of the problematic issues that would arise in the two-bladed configuration.

The final objective is to provide a set of key figures that would allow for a direct comparison of the two-bladed configuration versus the reference three-bladed one. The key figures will provide WP 1 with a background to estimate the cost of energy associated with the proposed configurations.

The two-bladed configuration is derived assuming the same rotor solidity as in the reference wind turbine, as to maintain similar aerodynamic characteristics and operation points. The structural characteristics of the two-bladed rotor are briefly summarized in terms of rotor mass and stand-still eigen frequencies. Thereafter, the contribution presents and analyses some of the complications related to the two-bladed configuration. First, the power losses due to increased tip effects are quantified for a stiff rotor, and for a fully flexible wind turbine structure operating in steady state. The steady state response of the two-bladed configuration is simulated using the aero-servo-elastic code HAWC2 [18] and is compared to the reference three-bladed wind turbine; the increase of tip losses effects from the three to the two bladed configuration are also quantified by performing 3D CFD rotor computations.

Thereafter, the contribution investigates the effects of the two-bladed sampling of the non-uniform turbulent wind field, and quantifies it in terms of increased variation of the aerodynamic loads over the rotor area. The investigation focuses then on the aeroelastic problem arising by the interference between the lower turbine vibration modes and the 2P forcing frequency, which originates from the rotation of the two blades in a non-uniform wind field. The problem is addressed by simulating the turbine response for different tower stiffness configurations. Finally, preliminary results for a two-bladed rotor with a teetering hub are provided.

Two-bladed rotor configuration

Derivation

To maintain the overall aerodynamic performances similar to the reference three-bladed rotor, the two-bladed rotor configuration is derived by keeping the same rotor solidity, hence the chord length is scaled by a factor of 1.5 throughout the blade span, and all the geometrical characteristics of the blade structure are scaled by the same factor. As the chord length is increased, the Reynolds numbers for the blade airfoil sections are also increased by the same factor; the effects of the increased Reynolds number on the blade airfoil aerodynamic coefficients are neglected in this preliminary investigation.

The structure of the blade is approximated to a main spar with a rectangular cross section, and the same section modulus as in the reference blade is assumed. Hence, the scaling of the blade geometry by a factor of 1.5 implies that the thickness of the spar section walls is reduced by a factor of $1/1.5$ [17]. The resulting spar section maintains the same area as the original one, and its second moments of area are increased by the square of the scaling factor. Therefore, each of the blades in the two-bladed configuration is assumed to have the same weight as the original blade, and the stiffness increased by

a factor of 2.25 (1.5^2) in both bending directions. Please note that the simplified blade scaling neglects any structural requirements that might arise from buckling restrictions, and also neglects the increase in weight given by the larger blade shell.

As the aerodynamic loads on the blade scale by the same factor as the chord length (1.5), whereas the blade stiffness scales by the square of it, the blade pre-bending in the flapwise direction is thus reduced by a factor of $1/1.5$.

A downwind configuration is chosen for the two-bladed rotor, and is thus decided to remove the shaft tilt (5° in the reference rotor) as well as the blades cone (2.5°).

Structural properties

By assuming that the original weight of the shaft and hub components is maintained, the two-bladed rotor configuration is lighter than the three bladed by the weight of one blade, hence reducing the total rotor weight by about 18 %.

		3 Bladed	2 Bladed
Blade Mass	[ton]	41.70	41.70
Rotor Mass	[ton]	228.00	186.30

Table 14: Comparison of rotor and blade mass for the reference 3 bladed and the proposed 2 bladed rotor configurations

As the blade stiffness is increased while the blade mass is preserved, the blade natural frequencies are increased.

Mode Nr.	3 Bladed	2 Bladed	Mode:
	Nat Frq. [Hz]	Nat Frq. [Hz]	
1	0.610	0.906	1st Flap
2	0.931	1.373	1st Edge
3	1.739	2.536	2nd Flap
4	2.761	3.975	2nd Edge
5	3.574	5.097	3rd Flap
6	5.693	6.650	1st Torsion

Table 15: Isolated (clamped) blade natural frequencies. The blade frequencies for the two bladed rotor configuration are increased due to the increased stiffness.

Compared to the original 3-bladed configuration, Table 16, the natural frequencies at stand-still for the whole turbine structure are slightly increased for the first two modes (tower fore-aft and side-to-side displacement) as an effect of the reduced rotor mass. The modes involving blade deflections are also increased due to the increased blade stiffness, the first asymmetric flap mode (yaw) changes from 0.55 Hz to 0.67 Hz, the second asymmetric flap mode (tilt) changes from 0.59 Hz to 0.81 Hz, and the first collective flap mode increases from 0.63 Hz to 0.93 Hz. Note that in the two bladed configuration different modes are obtained depending on whether the standstill analysis is performed with the horizontal or vertical blades, as the asymmetric vibration modes only appears in the corresponding blade positions; the blades positions have only minor effects on the tower and collective modes.

3 Bladed Reference				
Modes	Damp. Frq [Hz]	Nat Frq. [Hz]	Log Decr	Mode
1	0.251	0.251	1.91	1st Tower SS
2	0.256	0.256	1.97	1st Tower FA

	0.500		3.10	1st fix-free mode
3	0.546	0.546	2.21	1st flap yaw
4	0.590	0.590	2.78	1st flap tilt
5	0.630	0.630	3.13	1st coll. Flap
6	0.922	0.922	2.93	1st asym. Edge plunge
7	0.936	0.936	3.00	1st asym. Edge SS
8	1.376	1.376	4.79	2nd asym. Flap yaw
9	1.550	1.551	6.14	2nd asym. Flap tilt

Table 16: First structural modes at standstill for the reference three-bladed wind turbine.

2 Bladed Downwind (vert.)				
Modes	Damp. Frq [Hz]	Nat Frq. [Hz]	Log Decr	Mode:
1	0.259	0.259	1.976	1st FA
2	0.265	0.265	2.041	1st SS
3	0.811	0.811	3.348	1st asym. Flap (Tilt)
4	0.926	0.926	4.545	1st coll. Flap
5	1.373	1.373	4.347	1st asym. Edge (SS)
6	1.870	1.870	6.120	2nd asym. Flap
7	2.312	2.312	4.589	2nd tower SS
8	2.490	2.490	2.366	2nd asym. Edge (+tow)

Table 17: First structural modes at standstill for the two-bladed wind turbine. The Frequencies are computed for the rotor with vertical blades.

2 Bladed Downwind (horiz.)				
Modes	Damp. Frq [Hz]	Nat Frq. [Hz]	Log Decr	Mode:
1	0.264	0.264	2.032	1st FA
2	0.265	0.265	2.046	1st SS
3	0.671	0.671	1.913	1st asym. Flap (Yaw)
4	0.925	0.926	4.544	1st coll. Flap
5	1.349	1.349	4.411	1st asym edge (Plunge)
6	1.710	1.710	6.331	2nd asym Flap
7	2.175	2.176	4.450	2nd coll Flap (+tow)
8	2.307	2.307	4.605	2nd tower SS

Table 18: First structural modes at standstill for the two-bladed wind turbine. The Frequencies are computed for the rotor with horizontal blades.

Steady state analysis

An aerodynamic analysis is first performed assuming a fully stiff structure; the aerodynamic power output is determined for the 3-bladed and the 2-bladed rotor setting identical properties in terms of blade pre-bending, tilt and cone angles, pitch and rotor speed operating conditions. The analysis is performed in uniform wind flow and allows for an estimation of the power losses directly ascribed to tip losses effects; simulations are performed for the 3D stiff rotor using the CFD code Ellipsys 3D, with the same settings as in the reference wind turbine computations [16]. The 3D CFD results are then compared

against the power losses predicted by the BEM model [18] that will be used in the following analysis.

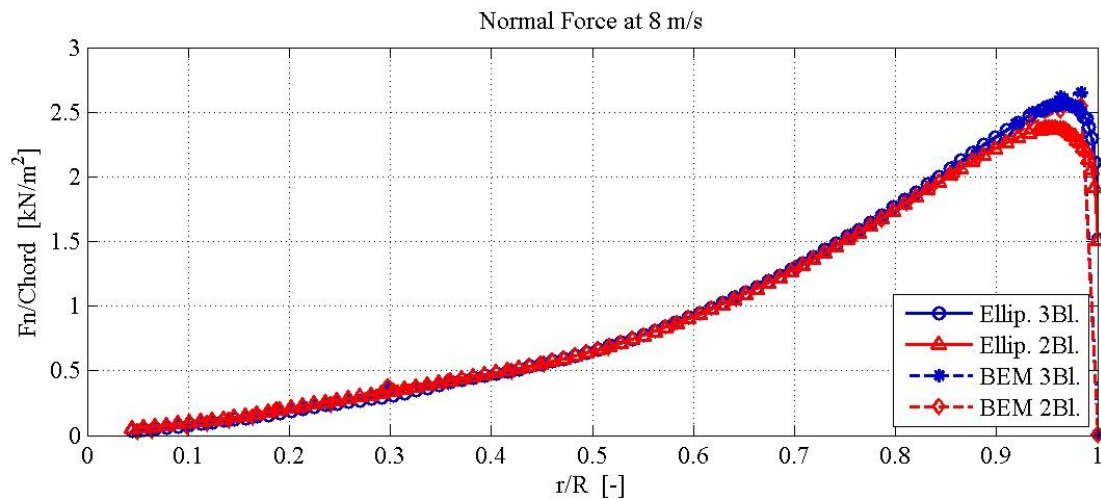


Figure 74: Normal aerodynamic force over the blade span, normalized by the chord length; results from 3D CFD simulations (Ellip.), and BEM analysis. The 2-bladed rotor displays larger tip losses, which decrease the normal force in the outer 30 % of the blade span.

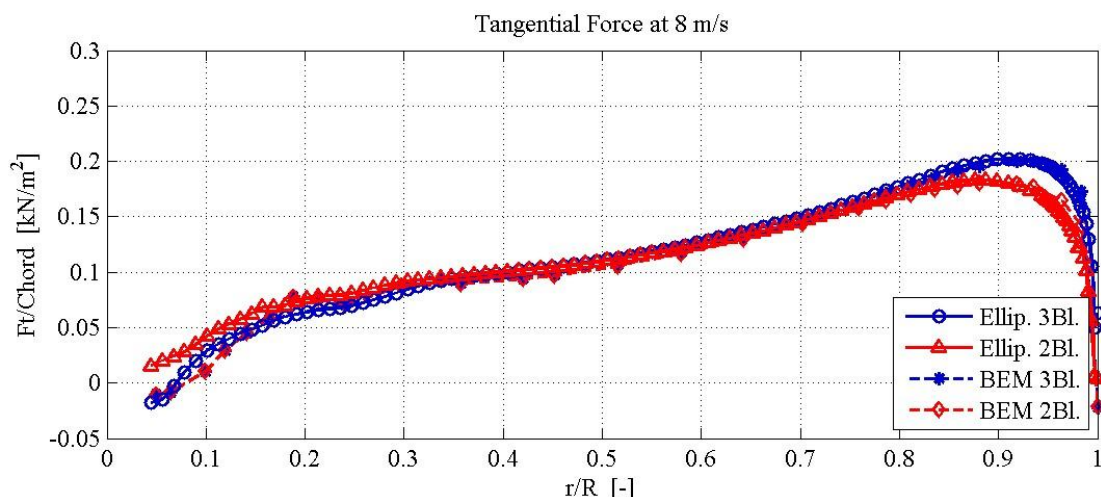


Figure 75: Tangential aerodynamic force over the blade span, normalized by the chord length; results from 3D CFD simulations (Ellip.), and BEM analysis. The 2-bladed rotor displays larger tip losses, which decrease the tangential force in the outer 30 % of the blade span.

The two-bladed rotor configuration presents higher tip losses which noticeably reduce the aerodynamic forces on the outer 30 % of the blade span, both for the normal, Figure 74, and the tangential forces, Figure 75. Generally, a very good agreement is reported between the BEM model and the 3D CFD simulations concerning both the forces distribution, and the increase of tip losses effects in the two-bladed configuration. The BEM model does not account for the finite span effects close to the blade root, and return the same normalized forces for both the two and three bladed configuration; the CFD simulations return instead higher tangential forces at the root for the two bladed configuration.

Overall, the larger tip losses in the two-bladed rotor configuration would cause a power reduction that, when the turbine operates close to optimal C_p conditions is estimated around 4.2 % by the BEM model; the 3D CFD computations return a slightly lower estimation of the power losses: 3 - 3.5 %. Larger losses are reported as the rotor thrust

coefficient is increased, at lower mean wind speed where the turbine operates at higher tip speed ratios, Figure 76.

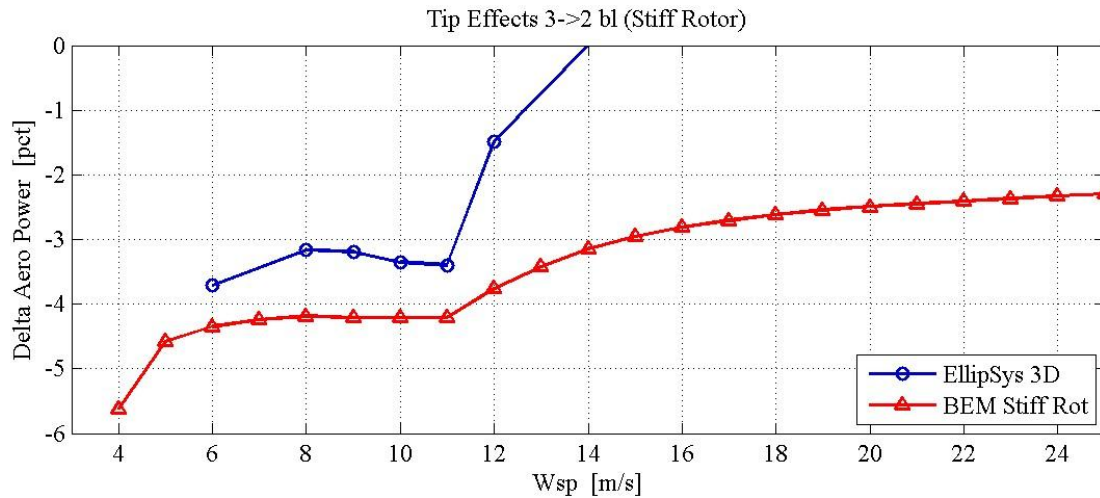


Figure 76: BEM aerodynamic analysis of the stiff rotor. Power reduction on the two bladed rotor due to tip losses; the reduction is given as a difference between the 2-bladed rotor output minus the 3-bladed one, normalized by the 3-bladed power output. The operating conditions (pitch angle and rotor speed) are identical for the two rotor configurations.

Similar figures in terms of power losses due to increased blade tip effects are also reported in a steady state analysis including all the structural degrees of freedom, Figure 77. The power reduction for the 2-bladed configuration is close to 4 % below rated conditions, whereas above rated wind speed the same power output is obtained as the controller compensates by setting the blade pitch to lower values, Figure 79. Probably, the power losses at lower wind speed could be at least partly mitigated by retuning the controller pitch and rotational speed settings to account for the lower rotor thrust close to the blade tip.

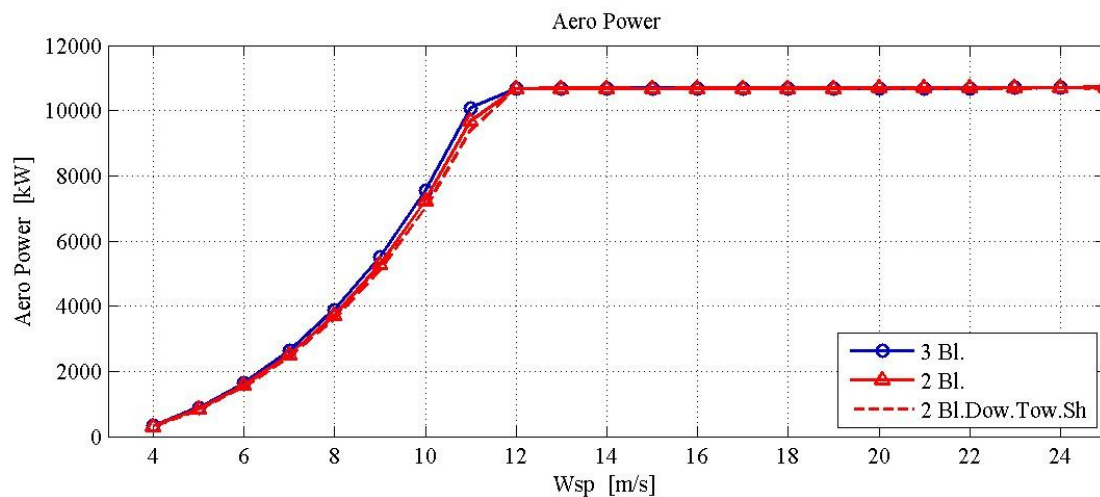


Figure 77: Steady state analysis of the reference 3-bladed wind turbine and the 2-bladed rotor configuration at different operating mean wind-speed. Comparison of the aerodynamic power output.

By adopting the downwind rotor configuration, the power output would be slightly increased due to the increased effective rotor area, but a larger reduction caused by more marked tower shadow effects decreases the overall power output.

The differences in the aerodynamic power output between the proposed rotor configurations are summarized in terms of Annual Energy Production for the turbine

placed in a IEC standard [19] class II site (Rayleigh distributed wind speed with 8.5 m/s average), Figure 78. The increased tip losses with the two bladed rotor account for an energy loss of about 2 %; passing from an up-wind to a down-wind configuration causes a further decrease of the energy output of about 1 %, due to higher tower shadow effects, only partly counterbalanced by the increased effective rotor area. Overall, in the investigated conditions, the proposed two-bladed rotor configuration delivers an energy output approximately 3 % lower than the reference three-bladed turbine configuration; the figures provide an indication for the cost of energy estimation to be performed in WP1.

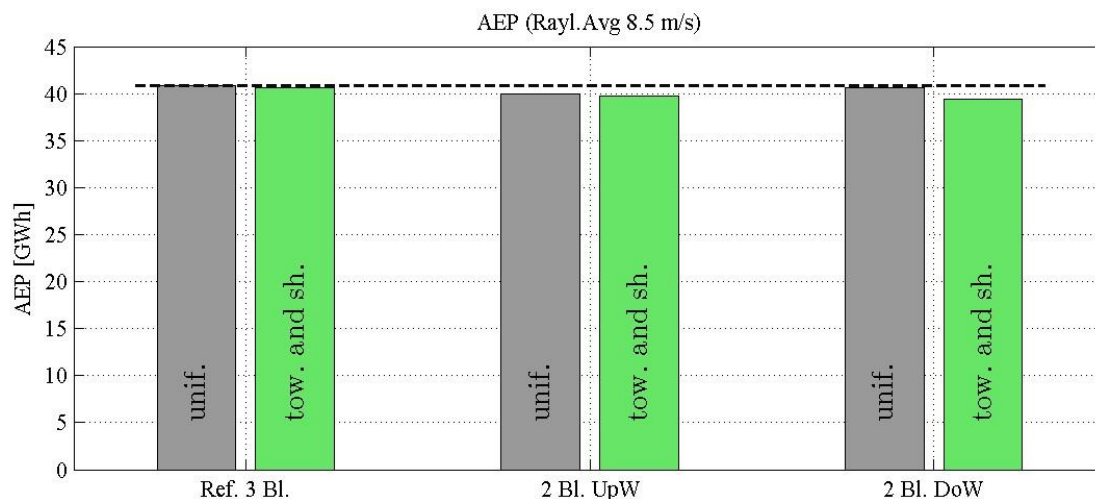


Figure 78: Annual energy production for the investigated rotor configurations in a class II IEC site. The proposed two-bladed rotor configuration leads to an overall AEP output that is approximately 3 % lower than the corresponding power output from the reference wind turbine (an efficiency factor of 0.935 is assumed in all cases).

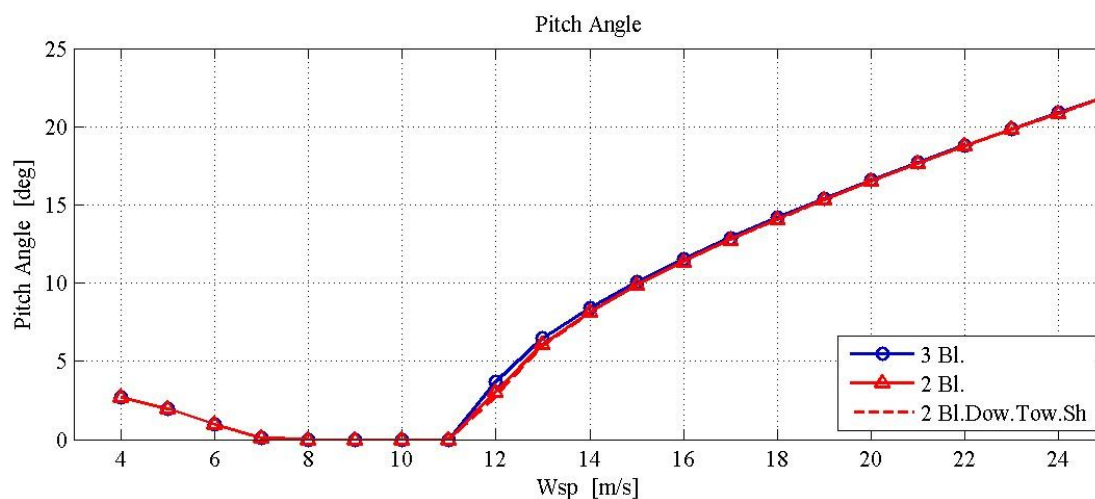


Figure 79: Steady state analysis of the reference 3-bladed wind turbine and the 2-bladed rotor configuration at different operating mean wind-speed. Comparison of the pitch angle settings.

The steady state analysis of the aerodynamic thrust force on the rotor area indicates slightly lower values for the two-bladed configuration up to rated conditions, and slightly higher just above rated due to the lower pitch angle, Figure 80.

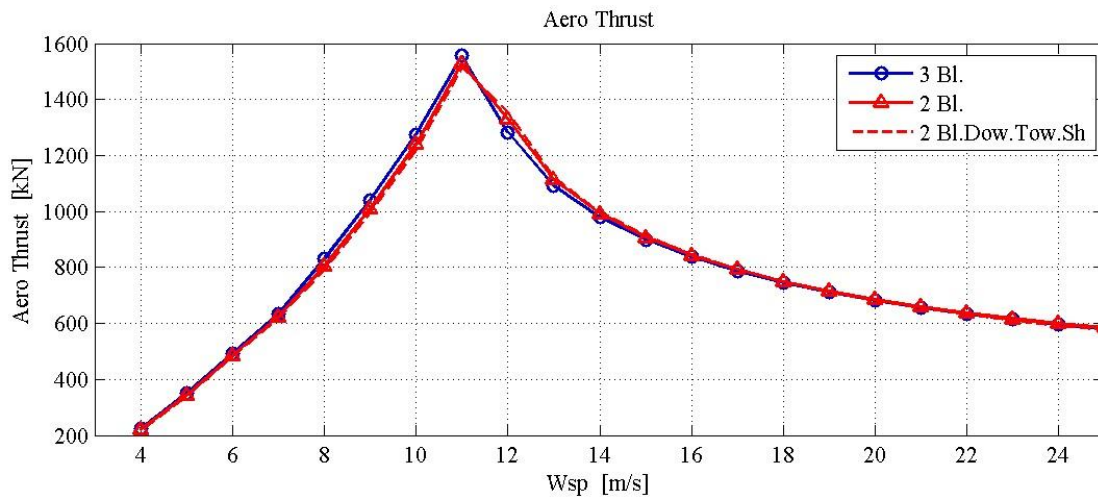


Figure 80: Steady state analysis of the reference 3-bladed wind turbine and the 2-bladed rotor configuration at different operating mean wind-speed. Thrust force over the rotor area.

The blade tip deflection at steady-state conditions clearly displays the effects of a stiffer structure in the two-bladed configuration: the maximum deflection is approximately 30 % lower than in the reference case, Figure 81. The two-bladed rotor reaches null tip deflection at the same operating wind speeds as the reference one, thus indicating an appropriate scaling of the blade pre-bending. The slightly lower deflections reported in the downwind rotor configuration are due to the absence of blade coning, which in the upwind configuration increases the deflection as centrifugal internal forces tend to ‘pull’ the blade closer to the rotor plane.

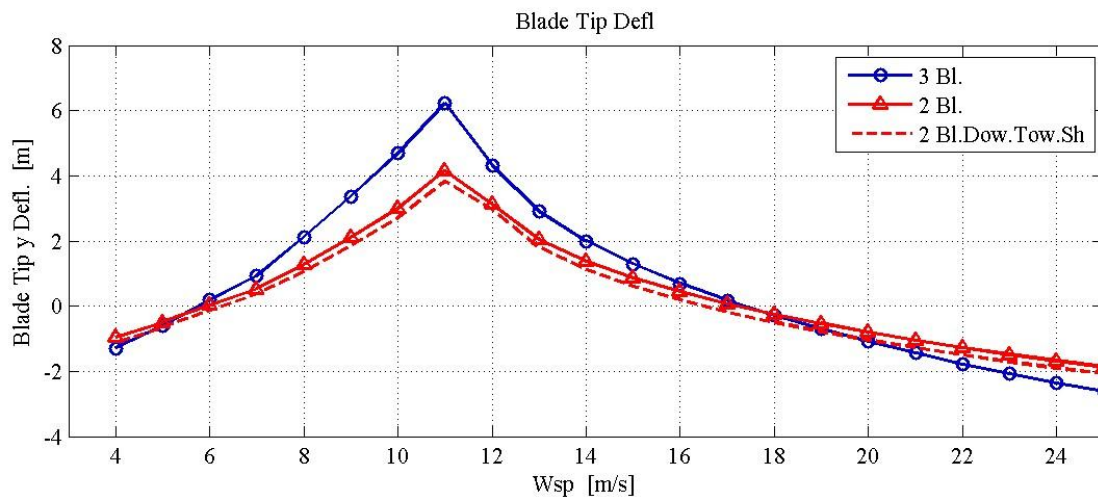


Figure 81: Steady state analysis of the reference 3-bladed wind turbine and the 2-bladed rotor configuration at different operating mean wind-speed. Blade tip deflection measured in the blade-base coordinate system.

Rotational frequency and turbulence spectrum

For a wind turbine operating in a non-uniform wind field, the prevailing forcing frequency on non-rotating structures corresponds to the frequency of the blade passage, and is thus equal to three times the rotational frequency in the reference wind turbine (3P), and twice the rotational frequency (2P) for the two-bladed configuration.

The energy content of the atmospheric turbulence increases at lower frequencies, and therefore the two-bladed configuration, with a main forcing frequency peak located at 2P, will transfer more of the turbulence energy to the non-rotating parts of the turbine. This section provides a quantification of the effects of the turbulent wind field sampling for the two rotor configurations. The analysis considers stiff structures and is performed for a mean wind speed at hub height of 10 m/s and a turbulence intensity of 0.18, corresponding to the IEC standard turbulence for a class B turbine.

The spectral analysis of the wind field observed at a stationary point (black line in Figure 82) displays the classical trend with increasing energy at lower frequencies. As the wind field is sampled in an observation point rotating with the blade (dashed black line), the spectral energy at the rotational frequency and its harmonic is increased. Correspondingly, the wind field sampled by the whole rotor, as is the case of the aerodynamic thrust force, displays a peak corresponding to the rotational frequency times the number of blades. The 2P frequency peak for the two-bladed configuration has higher energy content than the corresponding 3P peak of the reference three-bladed configuration, as it is placed closer to the turbulence frequency range with higher energy.

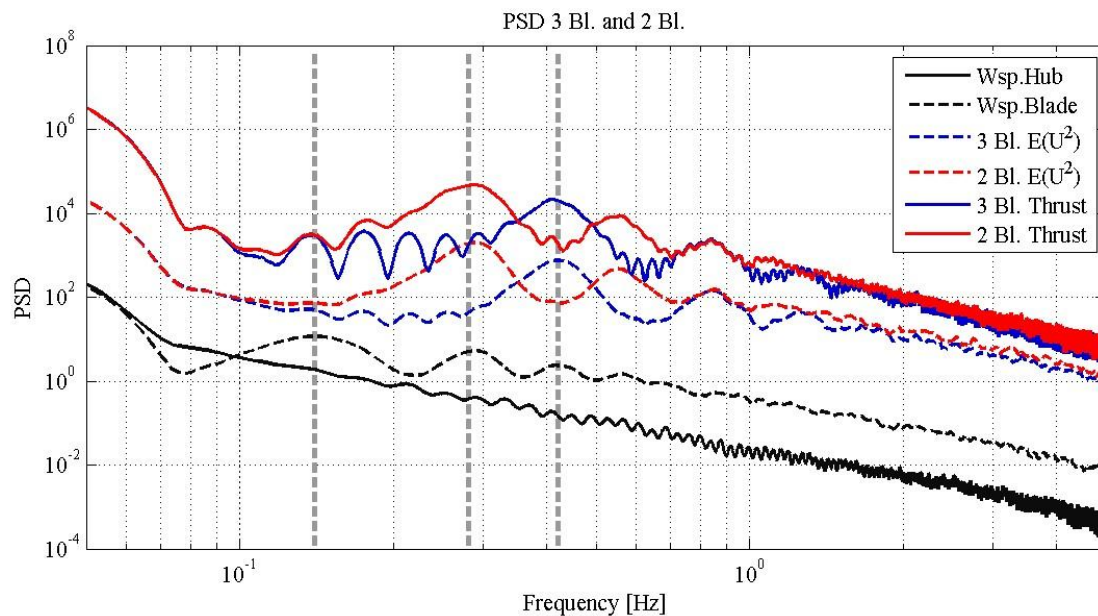


Figure 82: Power Spectral Density for the two-bladed and the three-bladed rotor configuration with a stiff wind turbine. Comparison of the spectra for the wind speed observed at the hub, on the rotating blade, an average of the wind speed squared observed on all the rotor blades, and the aerodynamic thrust. The vertical dashed gray lines indicates the frequencies corresponding to 1P (revolution frequency), 2P and 3P.

By analysing the cumulated power spectral density below the spectra curves in the range from 0.05 to 5 Hz, it is clear that most of the spectral energy for the aerodynamic thrust is acquired at frequencies of 2P and 3P for, respectively, the two and three bladed configurations, Figure 83. The spectra are normalized by the spectral energy in the frequency range for the reference three-bladed case, thus showing that the spectral energy for the two-bladed configuration is approximately 15 % higher in the frequency range from 0.05 to 5 Hz; therefore, as a consequence of the lower dominant frequency peak, the two-bladed configuration will experience higher load fluctuations due to the turbulent wind.

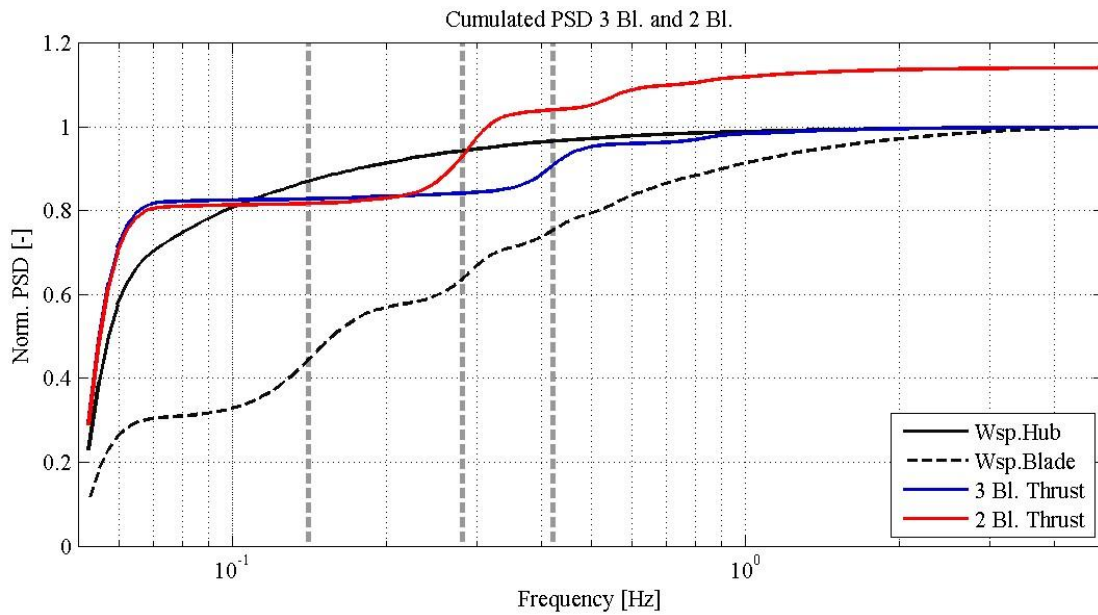


Figure 83: Cumulated PSD in the range 0.05 to 0.5 Hz for the wind speed and thrust time series in the 2 and 3 bladed configuration. The spectra are normalized by the total spectral energy value in the range for the reference three-bladed configuration.

The effects of the different sampling of the variations in the wind field on the tower bottom loads are estimated by computing damage equivalent loads (DEL) for the time series given by the thrust times the tower height. The investigation is performed with a stiff wind turbine structure, operating with constant rotational speed at an average wind speed of 10 m/s; different wind field conditions are considered: a wind field with only terrain shear effects (described by a standard power law coefficient of 0.3 [19]), shear and tower shadow, atmospheric turbulence only, and, as in normal operating conditions, a combination of all three, Figure 84. The DEL reported with the two-bladed configuration is approximately 25 % higher, mainly as a consequence of the lower frequency sampling of the turbulent wind field, and the higher tower shadow effects, as also highlighted by the contribution from CENER.

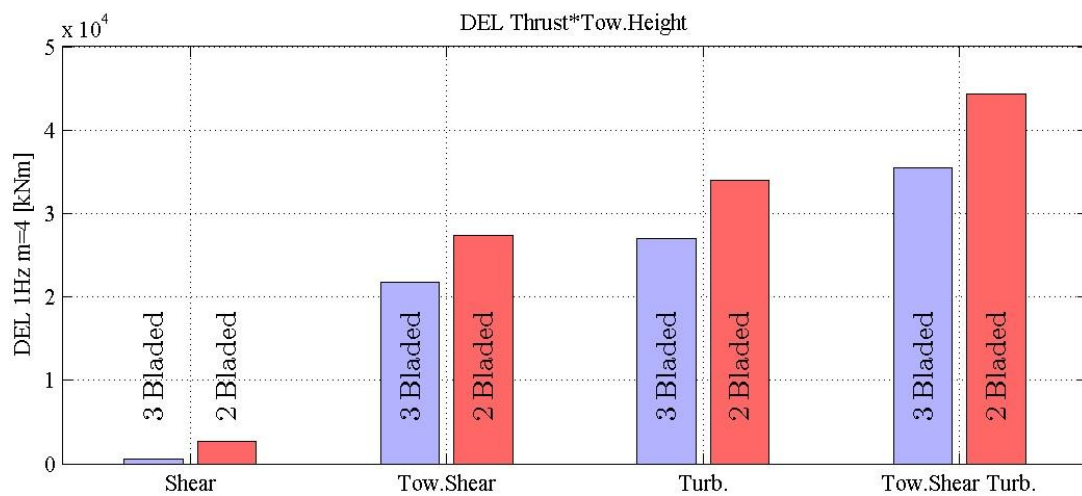


Figure 84: Fatigue Damage Equivalent Loads corresponding to the tower bottom fore-aft moment produced by the rotational sampling of a non-uniform wind field in the reference three-bladed configuration, and the two-bladed one.

Aeroelastic interaction with the tower modes

A major problematic in the two-bladed rotor configuration is that the prevailing forcing frequency of 2P lies close to the first tower modes and crosses them for operating wind speeds between 8 and 10 m/s. The result is a significant (and undesired) amplification of the tower loads and structural vibrations. In fact, by keeping the same tower as in the reference model, for operations at 10 m/s wind speed with a turbulence intensity of 0.18, the tower bottom DEL with the two-bladed configuration would be approximately 4 times larger than the reference turbine one, and the standard deviation of the tower top displacement as much as 2.5 times larger than the original one.

The two-bladed rotor configuration hence requires a re-design of the tower structure. The present contribution explores different tower design possibilities by investigating the effects on the tower loads and deflection from changes in the tower structural stiffness.

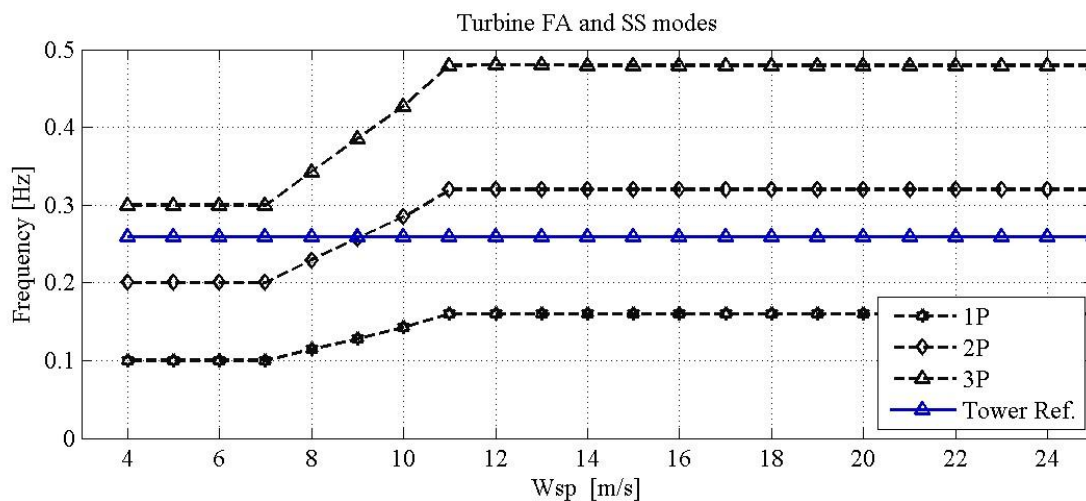


Figure 85: Rotational frequencies of 1P, 2P and 3P for the reference wind turbine. The first tower modes for the whole structure lie close to the 2P frequency, thus causing significant load amplification in the two-bladed configuration.

The stiffness of the tower structure is modified in two ways: with a uniform stiffness scaling, Figure 86, and by modifying the stiffness distribution in a linear way to obtain more marked variations at the tower base while leaving the higher quarter of the tower structure unchanged, Figure 87.

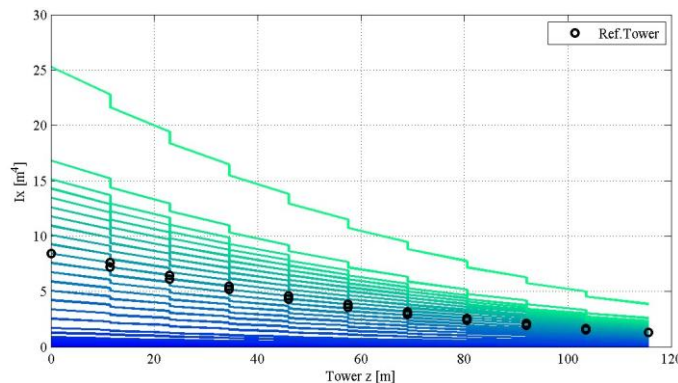


Figure 86: Uniform tower stiffness scaling. The same scaling factor is applied to the second moment of areas in the two directions throughout the tower length.

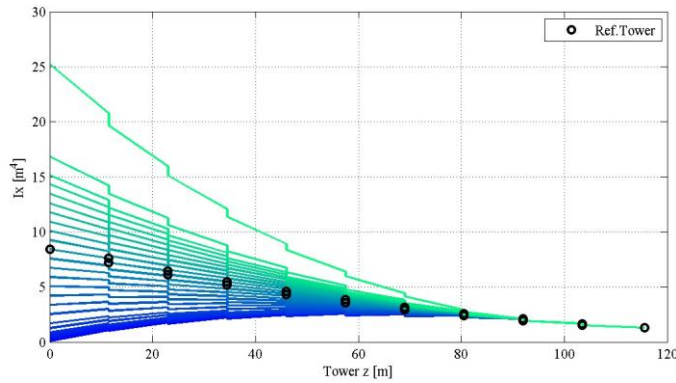


Figure 87: Base tower stiffness scaling. The second moments of area are modified by the specified scaling factor at the base of the tower, and left identical to the reference one in the top 25 % thus resulting in more marked reductions (or increase) of the stiffness close to the tower base.

By changing the stiffness of the tower, the frequencies of the first structural modes (Side-To-Side and Fore-Aft displacement) are also varied. While the uniform stiffness scaling produces larger variations of the modes frequencies, Figure 88, the base scaling has a lower impact on the other modes of the structure, Figure 89.

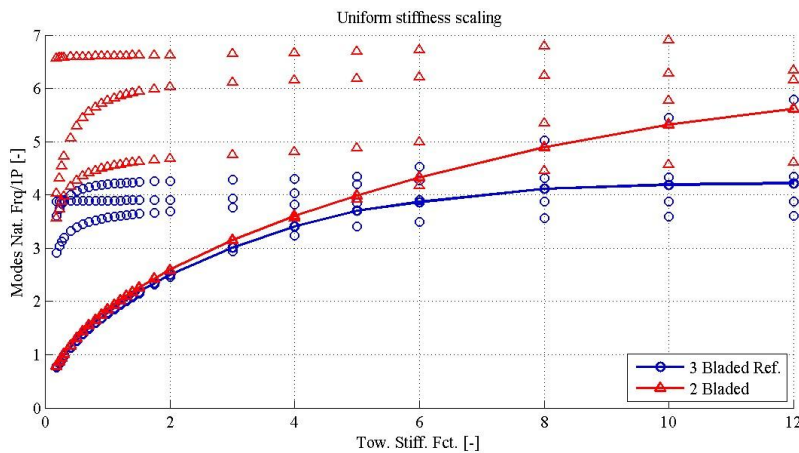


Figure 88: Structural modes at stand-still for different tower stiffness scaling factors. A uniform scaling of the stiffness is applied. The full line highlights the mode corresponding to the tower fore-aft displacement at stand-still.

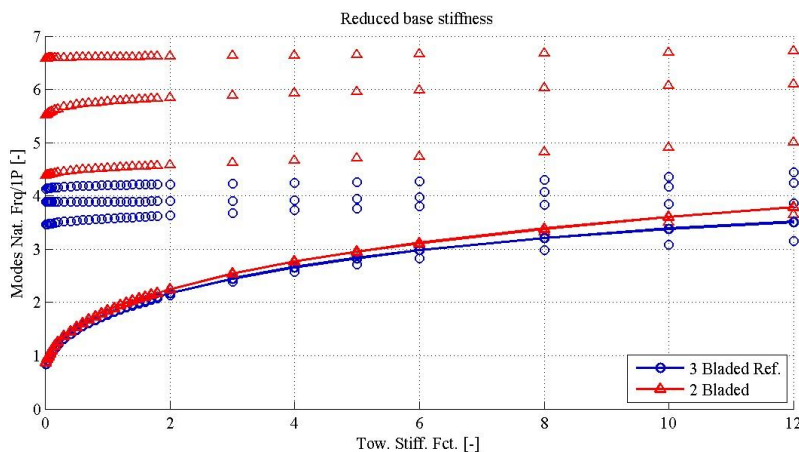


Figure 89: Structural modes at stand-still for different tower stiffness scaling factors. Larger scaling is applied to the tower base. The full line highlights the mode corresponding to the tower fore-aft displacement at stand-still.

The effects from different tower stiffness configurations are investigated by running aeroelastic simulations at a mean wind speed of 10 m/s, and considering a turbulent wind field with t.i. 0.18, terrain shear and tower shadow effects; to allow for a direct comparison, the same turbulence box is used in all computations. To simplify the analysis, the turbine controller is excluded: a constant rotational speed of 0.883 rad/s (1P = 0.14 Hz) and zero pitch angles are maintained throughout the simulations. The response of the structure is monitored in terms of 1 Hz fatigue Damage Equivalent Loads

(DEL) at the tower base, and in terms of standard deviation of the displacement at the tower top. The structural responses are plotted versus the frequency of the fore-aft vibration mode at standstill, normalized by the 1P rotational frequency; the loads obtained with a stiff tower structure are given as a term of reference (dashed lines). Please note that the vibration frequencies for the rotating turbine differ from the corresponding stand-still ones, especially for higher frequencies.

The response on the tower base fore-aft (FA) DEL displays a clear amplification of the loads as the tower mode frequency approaches the dominant forcing frequencies of 2P and 3P, respectively for the two (red lines) and three -bladed (blue lines) configurations, Figure 90. The 2P peak for the two-bladed configuration and the response with a stiff tower (dashed line) are higher than the corresponding three-bladed ones, since, as already discussed, the two-bladed rotor undergoes larger variations of loads due to turbulence sampling, and tower shadow effects.

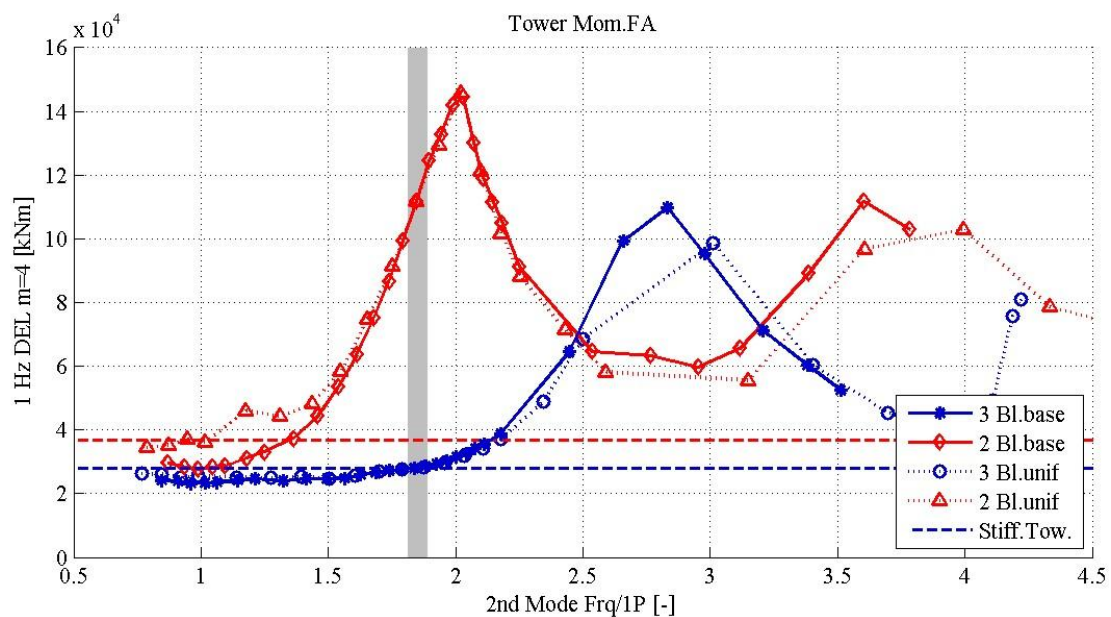


Figure 90: Response on the DEL at the tower bottom from different tower stiffness configurations. The grey shaded area indicates the tower mode frequencies for the reference wind turbine. Simulations at 10 m/s, 1P = 0.14 Hz.

The grey shaded area indicates the frequency corresponding to the reference tower stiffness; although very appropriated for the three-bladed rotor, the reference tower design would cause a significant amplification of the loads in the two-bladed configuration. A re-design of the tower stiffness is thus necessary. The investigation indicates that a more compliant tower, giving a mode with stand-still frequencies close to 1-1.5 P would be beneficial in terms of load amplification. Furthermore, redesigning the tower stiffness distribution by having a more compliant structure close to the base appears preferable, as causing lower interference from the other modes.

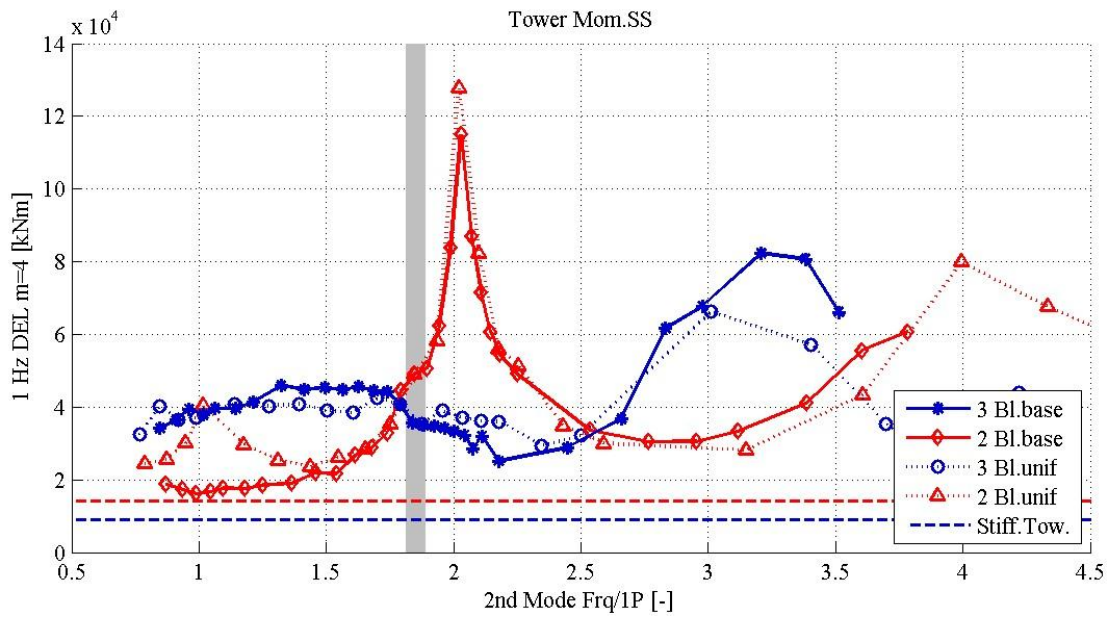


Figure 91: Response on the DEL at the tower bottom side-to-side from different tower stiffness configurations. The grey shaded area indicates the tower mode frequencies for the reference wind turbine. Simulations at 10 m/s, 1P = 0.14 Hz.

Similar results are also obtained for the tower bottom side-to-side fatigue DEL, Figure 91, whereas the tower top displacement indicates, as expected, that a more compliant tower will result in larger variations of the tower top displacement, Figure 92.

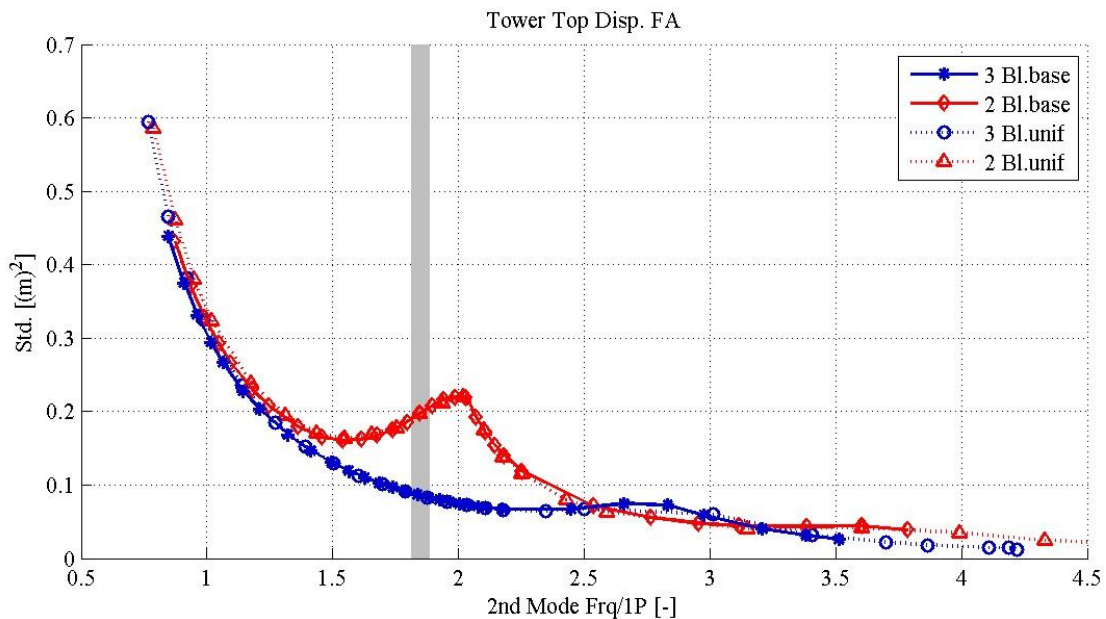


Figure 92: Response to operation with different tower stiffness configurations in the standard deviation of the tower top fore-aft displacement. The grey shaded area indicates the tower mode frequencies for the reference wind turbine. Simulations at 10 m/s, 1P = 0.14 Hz.

Teetering hub configuration

A preliminary analysis with a free teetering hub configuration is carried out by running aeroelastic simulations in the same conditions: mean wind speed of 10 m/s, t.i. 0.18, constant rotational speed and zero pitch. The presence of the teetering hub has a relatively small impact on the tower loads, where it decreases the loads in the fore-aft

direction, Figure 93, and increases the one in the side-to-side; in the latter case considerably so as the tower mode approaches the 2P forcing frequency, Figure 94.

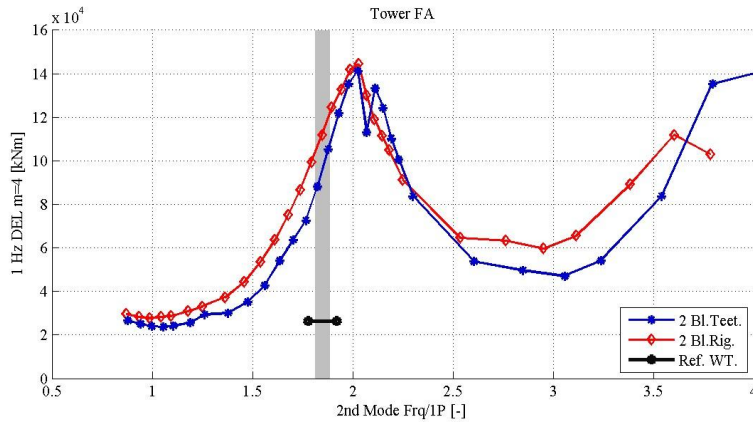


Figure 93: Response on tower fore-aft DEL for different tower stiffness (base scaling), rigid hub vs. teetering hub.

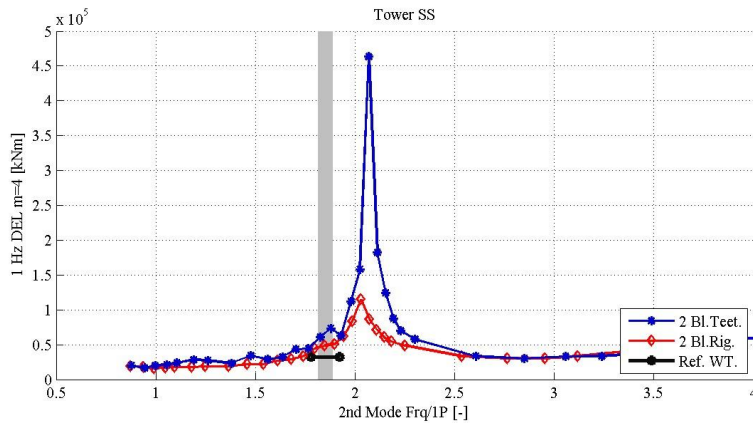


Figure 94: Response on tower side-to-side DEL for different tower stiffness (base scaling), rigid hub vs. teetering hub.

The presence of the teetering hinge is instead beneficial for the loads on the rotor shaft, which are considerably reduced (80 % less) compared to the reference three-bladed wind turbine, Figure 95. The teetering hinge also alleviates the flapwise DEL at the blade root, which is decreased to nearly the same level of the reference wind turbine, in spite of the larger aerodynamic loads due to the longer airfoil chord, Figure 96. The alleviation occurs mainly about the 1P rotational frequency.

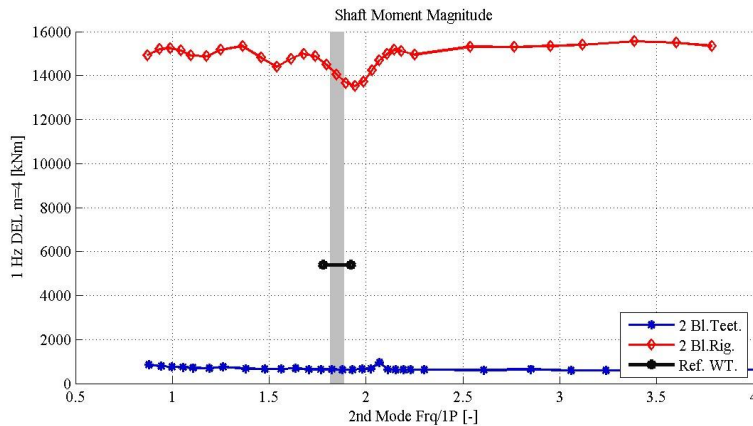


Figure 95: DEL on the shaft main bearing. The loads are scarcely affected by the tower stiffness, but significantly reduced by the teetering hinge.

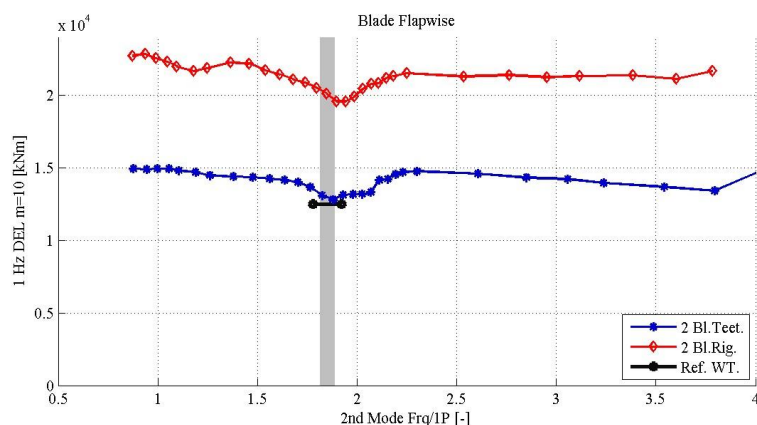


Figure 96: DEL on the blade root flapwise bending moment. The loads are scarcely affected by the tower stiffness, and reduced by the teetering hinge, down to nearly the level of the reference wind turbine.

Conclusion

The contribution proposed a down-wind two-bladed rotor configuration for the DTU 10 MW reference wind turbine. The rotor has the same solidity as the original one, hence the geometry is scaled by a factor of 1.5 giving a maximum chord length of 9.3 m. Under the listed assumption, the two-bladed rotor would be 18 % lighter than the reference one.

The two-bladed configuration is affected by higher tip losses; the decrease in power output below rated conditions is estimated around 4 % by BEM computations. Verification of the tip-losses prediction with 3D CFD computations returned a slightly lower value, with power loss estimations close to 3.4 % below rated conditions. Considering both the increase in tip losses and tower shadow effects, the annual energy yield by the two-bladed configuration in a reference site would be 3 % lower than the reference three-bladed turbine.

The two-bladed rotor samples the non-uniform wind field at a lower frequency, where the turbulence energy content is higher, thus resulting in larger variations of the loads over the rotor area. In the investigated conditions, an ideal stiff turbine with the two-bladed downwind configuration would have approximately 25 % higher Damage Equivalent Loads on the tower bottom.

The two-bladed rotor would require redesigning the stiffness of the turbine tower to avoid load amplification effects given by the excitation of the tower modes from the 2P frequency. The investigation has shown that a more compliant tower, with the first modes close to 1-1.5 times the rotational frequency, would be preferable in terms of load amplification. On the other hand, a lower tower stiffness would imply larger oscillations of the rotor position, and would require a re-tuning of the turbine controller toward a slower response. Furthermore, lower structural modes would get closer to the peak frequency of the wave loads spectrum (approximately in the order of 0.05 - 0.1 Hz). These issues were not investigated in the present contribution, and should be addressed in future studies.

A teetering hub configuration has shown promising results in terms of blade and especially shaft DEL alleviation. In future investigations the teetering hub configuration will be compared against, and eventually combined with, active load alleviation solutions, as individual pitch or active trailing edge flaps.

REFERENCES

- [1] J. Jonkman, S. Butterfield, W. Musial, G. Scott, "Definition of a 5-MW reference wind turbine for offshore system development" NREL/TP-500-38060, 2007
- [2] Eize de Vries, "Sway Turbine unveils 10 MW design", Windpower Offshore, Oct 23 2012
- [3] SeaTitan 10 MW Wind Turbine <http://www.amsc.com/documents/seatitan-10-mw-wind-turbine-data-sheet/>
- [4] The 6MW-154m Siemens wind turbine http://www.energy.siemens.com/hq/pool/hq/powergeneration/renewables/windpower/6_MW_Brochure_Jan.2012.pdf
- [5] The V164-8.0 MW <http://www.vestas.com/en/wind-power-plants/procurement/turbine-overview/v164-8.0-mw-offshore.aspx#/vestas-univers>
- [6] The 6MW Heliade 150 Alstom wind turbine <http://www.alstom.com/power/renewables/wind/offshore-wind-turbines/>
- [7] Peter Jamieson, Innovation in Wind Turbine Design, A John Wiley & Sons, Ltd., Publication, ISBN 978-0-470-69981-2, 2011
- [8] Chaviaropoulos, P.K., Chortis, D., Lekou, D. Definition of the Reference Wind Turbine – Analysis of Rotor Design Parameters (D1.2.1, May 2013, Innwind.EU Internal site)
- [9] NWTC Computer-Aided Engineering Tools (AeroDyn by David J. Laino, Ph.D.). <http://wind.nrel.gov/designcodes/simulators/aerodyn/>. Last modified 23-February-2013; accessed 8-August-2013.
- [10] Grasso, F., "Design and optimization of Tidal Turbine Airfoils", Journal of Aircraft, AIAA, Vol.49, No.1, Jan.-Feb. 2012.
- [11] Grasso, F., "Usage of Numerical Optimization in Wind Turbine Airfoil Design", AIAA, Journal of Aircraft, AIAA, Vol.48, No.1, Jan.-Feb. 2011, DOI: 10.2514/1.C031089
- [12] Grasso F., "Design of a Family of Advanced Airfoils for Low Wind Class Turbines", EWEA, Torque2012, 9-11 October 2012, Oldenburg, Germany
- [13] Grasso, F., "Hybrid Optimization for Wind Turbine Thick Airfoils", AIAA Proceedings, 9th AIAA Multidisciplinary Design Optimization Specialist Conference, 23-26 April 2012, Honolulu, HI, USA. AIAA 2012-1354.
- [14] Bot, E.T.G., Ceyhan, O., "Blade Optimisation Tool, User Manual". ECN, Petten, the Netherlands, ECN-E-09-092.
- [15] van Rooij, R.P.J.O.M., "Modification of the boundary layer calculation in RFOIL for improved airfoil stall prediction", Report IW-96087R TU-Delft, the Netherlands, September 1996
- [16] Bak, Christian, Frederik Zahle, Robert Bitsche, Taeseong Kim, Anders Yde, Lars Henriksen, Anand Natarajan, and Morten Hartvig Hansen. *Description of the DTU 10 MW Reference Wind Turbine*. Roskilde, Denmark: DTU Wind Energy, July 2013.
- [17] Larsen, Torben J., Helge Aagard Madsen, Kenneth Thomsen, and Flemming Rasmussen. "Reduction of Teeter Angle Excursions for a Two-bladed Downwind Rotor Using Cyclic Pitch Control." In Proceedings of European Wind Energy Conference (EWEC). Milan, 2007.
- [18] Larsen, Torben Juul. *How 2 HAWC2 the User's Manual*. Risø National Laboratory. Technical University of Denmark, 2009.
- [19] International Electrotechnical Commission. IEC 61400-1: Wind Turbines Part 1: Design Requirements. International Electrotechnical Commission, 2005.

